To the Graduate Council:

I am submitting herewith a dissertation written by Prajakta Kamerkar entitled "Experimental study of slip flow in the semi-hyperbolically converging dies". I have examined the final electronic copy of this dissertation for form and content and recommend that it be accepted in partial fulfillment of the requirements for the degree of Doctor of Philosophy, with a major in Chemical Engineering.

Dr. Brian J. Edwards

Major Professor

We have read this dissertation
and recommend its acceptance.

Dr. John Collier

Dr. David Keffer

Dr. Simioan Petrovan

Dr. Kevin Kit

Acceptance for the Council:

Anne Mayhew

Vice Chancellor and Dean of Graduate Studies

(Original signatures are on file with official student records.)

EXPERIMENTAL STUDY OF SLIP FLOW IN THE SEMI-HYPERBOLICALLY CONVERGING DIES

A Dissertation
Presented for the
Doctor of Philosophy
Degree
The University of Tennessee, Knoxville

Prajakta Arun Kamerkar
August 2005

DEDICATION

This dissertation is dedicated to my parents, Arun Kamerkar and Madhuri Kamerkar, whose constant love, understanding, support and encouragement has enriched my life, and to my fiancé Vishal Koparde, for his unwavering faith in me, and his enduring love.

ACKNOWLEDGEMENTS

I wish to thank my research advisor, Dr. Brian Edwards, for his guidance, support and encouragement throughout my studies here at the University of Tennessee, Knoxville. I would like to express my gratitude towards all my committee members, Dr. John Collier, who has been very encouraging throughout my research and has permitted the use of his rheology lab for my work, Dr. Simioan Petrovan for his valuable guidance and input in the experimental techniques, Dr. David Keffer for his helpful discussions in the computational field and about life in general, and Dr. Kevin Kit for his useful suggestions.

I would like to thank Dr. Brian Edwards and the Chemical Engineering Department for the financial support during my studies. I want to thank Mr. Doug Fielden for his assistance in making the capillary dies. I would also like to thank Dr. Simioan Petrovan and Mr. Keys from ExxonMobil for providing the different polymers. I want to thank Dr. Parag Patil and Dr. Yizhong Wang for their help in the lab. I would like to extend special thanks to my colleague and friend, Bangwu Jiang, for his camaraderie and encouragement.

Finally I would like to thank my parents and my sister, Sarika, for their support.

ABSTRACT

This dissertation contains a collection of the results from three different projects.

Part I: Experimental Study of Slip Flow in the Semi-hyperbolically Converging Dies

Elongational flow fields are of immense importance in the polymer processing industry as the elongational flow used in processes such as fiber spinning, film blowing, melt drawing, etc., produces the desired degree of polymer orientation so that the final products have the target properties of toughness and durability. Although these processes are widely used, it is very difficult to characterize the extensional rheological properties of polymers, such as elongational viscosity. This can be attributed to the difficulty in developing the experimental methods for measuring the elongational flow properties.

In late 1990s, Collier and co-workers began work on a project aimed at developing an inexpensive, reliable, accurate, and simple to use device to measure the elongational viscosity of polymer melts in a uniaxial elongational field. They have developed the semi-hyperbolically converging dies, the shape of which follows the natural pathways of the streamlines required to produce a purely uniaxial elongational field, provided that the assumptions used in the theoretical development are satisfied. We have continued the work with the semi-hyperbolically converging dies developed

by Collier and co-workers. The research focused on analyzing the assumptions used in the development of these dies.

The semi-hyperbolically convergent dies are used to measure the effective elongational viscosities of polymer melts and solutions at the industrial processing conditions. Based on a recent study by Feigl et al., it was confirmed that when full slip was assumed at the die walls in the semi-hyperbolically convergent dies, one can obtain an essentially purely uniaxial elongational flow. The degree of slippage taking place in these dies was scrutinized experimentally in our research based on the knowledge that small amounts of carboxylic acid additives can greatly reduce the shear viscosity in many polymer melts. We used the Mooney analysis to quantify the slip in capillary dies for various thermoplastics such as polypropylene, low-density polyethylene, and high density polyethylene. The Mooney equation was modified to fit the semi-hyperbolically convergent dies. Experiments were then performed to quantify the degree of slip in both the capillary and the semi-hyperbolically convergent dies.

Part II: Shear Thickening in Dilute Polymer Solutions: Transient Analysis

Transient shear properties of dilute polymer solutions were investigated in the shear-rate regions where shear thickening can occur. Comparison of transient rheological and optical data with the Two Coupled Maxwell Modes Model offered insight into the physical mechanisms that give rise to this anomalous behavior. Specifically, shear thickening occurs due to the deterioration of the size and anisotropy of structures deformed at lower shear rates. Coincident theoretical and experimental

discontinuities in the transient profiles of the dichroic orientation angle appear to confirm the prior statement.

Part III: Additional Experimental Research in Polymer Melt Rheology

Shear flow of low-density polyethylene was investigated in other non-dissertation related work. Small amplitude oscillatory shear experiments and steady shear experiments were performed on an industrial grade LDPE and the experimental data was used in modeling work of rheological properties of polymeric fluids. I am the co-author on two published articles on this work, and a third currently under preparation. My contributions included performing several types of experiments, such as transient and steady shear experiments, small amplitude oscillatory shear flow, elongational flow, and step-strain experiments. This additional research is not considered as part of this dissertation, so only a brief summary is described in this document.

TABLE OF CONTENTS

LIST OF TABLES

Part I

Part II

LIST OF FIGURES

Part I

Part II

Part III

NOMENCLATURE AND ABBREVIATIONS

Nomenclature

Part I

$\underline{\underline{\dot{\gamma}}}$	Rate-of-strain tensor
$\underline{\underline{\tau}}$	Stress tensor
$\underline{v}$	Velocity vector field
$\dot{\varepsilon}(t)$	Elongational strain rate
l	Distance separating two fluid particles
η_e	Elongational viscosity
η	Shear viscosity
η_{eff}	Effective elongational viscosity
$\tau_{11,}\tau_{33}$	Normal stresses
ε_h	Hencky strain
z	Axial flow direction
R	Radius of the flow channel
C,B	Constants
R_o	Inlet radius
R_e	Exit radius
L	Length of the die
Ψ	Stream function
Φ	Potential function
ρ	Density
v_r	Velocity component in r direction

v_z	Velocity component in z direction
$\underline{q}$	Heat flux
$\hat{H}$	Enthalpy per mass unit
a	Radius of the capillary tube
Q	Flow rate
E_β	Flow rate due to slip
E_φ	Flow rate due to fluidity
P	Pressure gradient
r	Distance from the axis of the capillary
v_{slip}	Velocity of slip
β	Coefficient of the slip at the stress s, defined by $v_{slip} = s\beta$
$\sigma_{rz}(r)$	Shear stress at the distance r from the axis
s	Shear stress at the surface of the capillary
$\frac{1}{\mu(r)}$	Fluidity at the stress σ, or reciprocal of the viscosity

Part II

$\dot{\gamma}_c$	Critical shear rate
$\dot{\gamma}_m$	Shear rate at the onset of shear thinning
$\mathbf{c}^1, \mathbf{c}^2$	Second-rank mode-conformation tensors
$\psi(\mathbf{x}, \mathbf{R}, t)$	Orientational distribution function
$\mathbf{R}$	End-to-end vector
$\mathbf{x}$	Eulerian coordinate
$f(\mathbf{x}, \mathbf{a}, t)$	Size distribution function
k_B	Boltzmann's constant
T	Absolute temperature

K_1, K_2	Hookean spring constants
λ_1, λ_2	Relaxation times of the modes
n_1, n_2	Effective concentrations
θ	Degree of interaction between two modes
N_A	Avagadro's number
Ψ_1, Ψ_2	First and second normal stress coefficients
$\Delta n''$	Dichroic signal
k	Wave number
c	Polymer concentration
M	Molecular weight
m_s	Refractive index of solvent
$\left(\alpha_1^2 - \alpha_2^2\right)$	Polarizability difference
p	Anisotropy function
V_p	Volume of the structure
η_s	Viscosity of the solvent
$\langle aa \rangle_0$	Squared diameter of the average structure
λ_p	Primary eigenvalue
ξ	Number of polymeric units per statistical chain length
e_s	Optical shape factor
$\dot{\gamma}_{ss}$	Steady-state shear rate
f_{obj}	Objective function
n_T	Total number of experimental data points
n_{set}	Number of transient dichroism profiles
n_d^i	Number of data points in the *i*-th data set
$w(j)$	Weighting factor

Abbreviations

ACER	Advanced Capillary Extrusion Rheometer
ARES	Advanced Rheometric Expansion System
SHCD	Semi-hyperbolically converging die
PP	Polypropylene
LDPE	Low-density polyethylene
HDPE	High-density polyethylene

Part I: Experimental Study of Slip Flow in the Semi-Hyperbolically Converging Dies

CHAPTER 1. INTRODUCTION

1.1. Importance of Elongational Rheometry

The original definition of rheology given by Bingham in 1929 states that 'Rheology is the study of the deformation and flow of matter'. There are two types of standard flows in rheology, namely, shear and elongational. The elongational flow is used for polymer processing in almost all the industrially important operations such as fiber spinning, film blowing, injection molding, and extrusion through converging profiles, where a rapid change of shape is required [1-3]. In these processing operations, the flow in converging or diverging regions of dies and molds has large extensional components. As the extensional flows strongly orient polymer molecules (as we will see in the review of elongational rheology), regions of extensional flow in a process will have a strong effect on the properties of the end products. Hence we need the extensional material function data to model these flows [2]. Due to such a widespread application of elongational flow, it is important to study elongational rheometry.

Rheometry is the process of making measurements of the rheological material functions, such as viscosity, first normal stress difference, etc. Here, an experiment is designed to produce the kinematics required to quantify the material function, then the necessary stresses are measured and the value of the material function is calculated [4]. In the case of elongational flow, the methods for measuring the material functions are not as well developed as in case of shear flow [5]. Thus, in elongational rheometry,

the most challenging part is generating the elongational flow field and maintaining it until the measurements are made.

The scarcity of elongational data can be attributed to the difficulties faced over the years to develop an appropriate experimental method to measure elongational properties. The abundance of shear data available does not make up for the meager proportion of elongational information regarding polymeric fluids undergoing the polymer processing operations mentioned above. These cannot be properly characterized using shear rheometry [4-6]. The importance of elongational rheometry in the polymer processing industry and to a polymer engineer is hard to overstate; thus it is imperative to overcome the daunting challenges that present themselves during these measurements.

1.2. Motivation and Relevance Behind the Presented Work

To understand the motivation behind this research, we have to comprehend the difficulties faced in measuring the elongational viscosities of polymers by prior researchers in this field. The techniques used for measuring elongational viscosities in the past had several drawbacks. Most importantly, these rheometers allowed the measurements at low temperatures (just above the melting point of the polymers) and at very low strain rates. However, the polymers used in industry are processed at high temperatures (well above the melting point of the polymers) and at very high strain

rates. We will discuss most of the widely used extensional rheometers and their shortcomings in Chapter 2 [7-20].

If we have experimental data under processing conditions, it will be very useful to determine which polymer is best suited for the application and delivers the desired end properties. Recent research using the semi-hyperbolically convergent dies has suggested that, in effect, a pure elongational flow can be generated using these dies in a modified capillary-type rheometer [21-23]. Collier and fellow researchers have developed a method of measuring elongational viscosities thereafter, and they have used this technique to measure the effective elongational viscosities of various polymers and polymer solutions at strain rates corresponding to the processing conditions relevant to industry [22-25]. This die, when coupled with the standard capillary rheometer systems, can become the solution to the challenges of measuring elongational flow properties. *The purpose of this research work is the analysis of this 'semi-hyperbolically convergent die'; we are trying to verify the validity of the assumptions used in the derivation of the expression for the elongational viscosity.* To use this die as an integral component of a rheometer, there are certain points that need to be resolved. First, it must be verified that the theoretical velocity profile used in the derivation of the effective elongational viscosity is, in fact, fully achieved under the experimental conditions. In a recent study by Feigl et al. [26] to test the assumptions used in the development of the device, a finite element method was applied to the flow of a Newtonian fluid and a specific polymer melt flowing through the semi-hyperbolically convergent die. The semi-hyperbolic shape of the die supposedly

makes the shear contribution to the overall flow field negligible. The finite element method study mentioned above confirmed that when full slip was assumed at the die walls, one can obtain essentially purely uniaxial elongational flow. The purpose of this study is to investigate whether the full wall slip condition within the die is valid at all times under the experimental conditions, or if, under experimental conditions, an intermediate condition between "no-slip" and "full wall-slip" is realized.

Recent research has shown that the addition of carboxylic acids to polymer melts can reduce the melt viscosities by as much as 50% [27]. This reduction in shear viscosity is attributed to the slip flow experienced by the polymer melt inside the capillary die as the acidic additive, being of lower viscosity, is pushed toward the high shear rate (i.e., the wall) region in the flow field. Thus, the additive essentially acts as a lubricant. Consequently, we want to characterize the qualitative nature of the velocity profile inside the semi-hyperbolically converging dies with and without the use of such lubricants. This study will also investigate the relationship between the extensional flow produced within the die and the resulting elongational viscosity.

CHAPTER 2. LITERATURE REVIEW

2.1. Elongational Rheology

The standard flows for rheology are characterized according to the components of the rate-of-strain tensor, $\dot{\underline{\underline{\gamma}}}$, and the stress tensor, $\underline{\underline{\tau}}$. The shear-free flow, or elongational flow, is one in which all off-diagonal or shear components of $\dot{\underline{\underline{\gamma}}}$ or $\underline{\underline{\tau}}$ vanish. There are three types of elongational flows that can be distinguished based on their velocity profiles. These are, namely, uniaxial elongational flow, biaxial stretching flow, and planar elongational flow. As uniaxial flow is widely used in many polymer processing operations, such as fiber spinning and injection molding, we will concentrate our efforts on this flow.

The uniaxial elongational flow is given by the velocity profile [4, 5]

$$\underline{v} = \begin{pmatrix} v_1 \\ v_2 \\ v_3 \end{pmatrix} = \begin{pmatrix} -\frac{\dot{\varepsilon}(t)}{2} x_1 \\ -\frac{\dot{\varepsilon}(t)}{2} x_2 \\ \dot{\varepsilon}(t) x_3 \end{pmatrix} \tag{I.1}$$

where $\dot{\varepsilon}(t)$ is the elongational rate and $\dot{\varepsilon}(t) > 0$ for this flow. We can see that in this three-dimensional flow, strong stretching occurs in one of the directions, while contraction takes place in the remaining two directions.

The rate-of-strain tensor, $\dot{\underline{\underline{\gamma}}}$, is given as

$$\dot{\underline{\underline{\gamma}}} = \nabla \underline{v} + (\nabla \underline{v})^T = \begin{pmatrix} -\dot{\varepsilon}(t) & 0 & 0 \\ 0 & -\dot{\varepsilon}(t) & 0 \\ 0 & 0 & 2\dot{\varepsilon}(t) \end{pmatrix} \tag{I.2}$$

When we observe the separation between two fluid particles undergoing uniaxial elongational flow, as seen in Figure 1, we see that the separation is exponential in time (not linear in time, as in the case of shear flow). The distance l separating the two particles is given by $l = l_0 e^{\dot{\varepsilon}_0 t}$. Thus, as time increases, the separation between the two particles increases exponentially. Due to this rapid rate of particle deformation, it is very difficult to achieve a steady elongational flow.

The kinematics of steady elongation is given as $\dot{\varepsilon}(t) = \dot{\varepsilon}_0 = \text{constant}$. Under these kinematics, the elongational viscosity is given as

$$\eta_e(\dot{\varepsilon}) = \frac{(\tau_{33} - \tau_{11})}{\dot{\varepsilon}} \tag{I.3}$$

Here, τ_{33} and τ_{11} are the normal stresses. The Hencky strain for a steady elongational flow can be obtained by integrating the elongational strain rate, and is given by the following expression:

$$\varepsilon_h = \dot{\varepsilon}_0 \, t = \ln \frac{l}{l_0} \tag{I.4}$$

Here, l_0 is the distance separating two fluid particles in uniaxial elongational flow initially at time equal to zero, and l is the distance at a time greater than zero. As it is

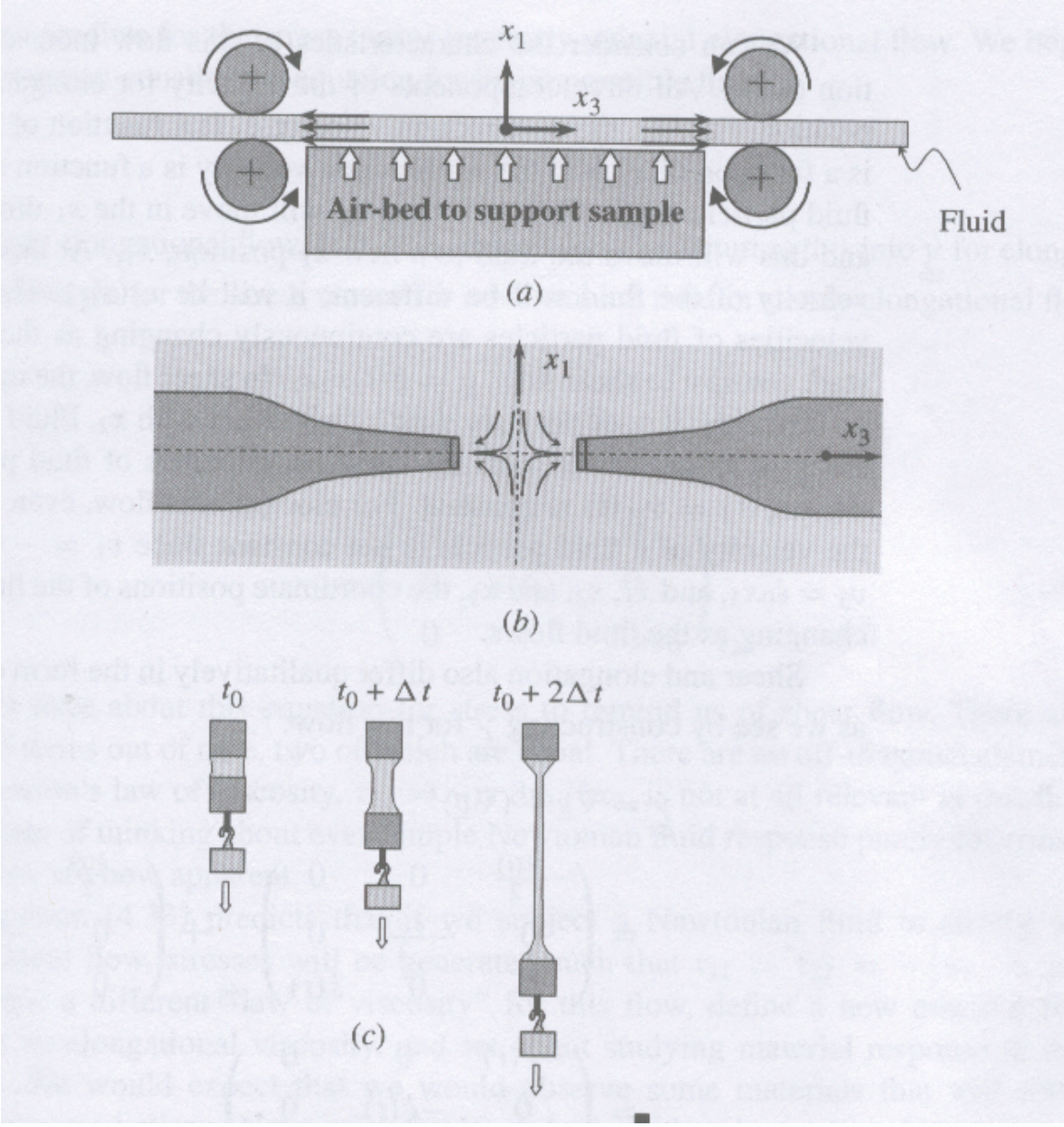

Figure 1: Geometries used to produce uniaxial extensional flow in commercial and research rheometers: (a) using a pulling device; (b) in an opposed-nozzle suction device; (c) uniaxial extension of polymer solutions by filament stretching [4]

difficult to obtain the steady state for this flow, we can only measure the transient elongational viscosity, which is a function of both time and strain rate.

Another useful result, obtained by Trouton [28], states that for Newtonian fluids, the steady uniaxial elongational viscosity is equal to three times the zero-shear viscosity, η_0. In the case of a non-Newtonian fluid, the elongational and shear viscosities are related as follows at the limiting condition when the elongational rates are very low and the shear rates are approaching zero:

$$\eta_e(\dot{\varepsilon}) = 3\eta(\dot{\gamma}) \tag{I.4}$$

2.2. Review of the Existing Elongational Rheometers and Measurement Techniques

As stated earlier in Section 1.1, elongational rheometry is still evolving. In this section, we will review the methods and techniques used in past and contemporary elongational rheometry. There are many methods on the basis of which different rheometers (which are still being used) have been designed. There are melt stretching, filament stretching, constant stress, contraction flow, and spinning techniques. Here, melt and filament stretching methods and constant stress methods are direct measurement techniques for measuring the elongational viscosities of polymer melts and solutions, whereas contraction flow and spinning techniques are indirect methods of measuring apparent elongational properties.

2.2.1 Direct measurement techniques

2.2.1.1 Melt stretching:

Melt stretching can be used to produce uniaxial elongational flow by stretching the polymer melt between separating crossheads. These crossheads serve the purpose of clamping the sample at the ends. The motion of cross heads is adjusted to give the desired elongational rate, $\dot{\varepsilon}(t)$, or a specific tensile stress value experienced by the sample.

We cannot achieve homogeneous uniaxial flow in practice, as illustrated in Figure 2 [4]; any initial defects in the original sample will introduce inhomogeneity in the flow. The process is particularly prone to inhomogeneity at the ends; hence flow in that region is not fully developed. Flow stability is also very much dependent on the surface tension, gravity, and air currents if this method is attempted in air. Consequently, only with extreme care and the usage of chemically inert fluids for thermal insulation and support of the stretching sample, can we obtain credible elongational data at very modest strains with this particular method.

Meissner [7, 9, 10] and coworkers have made very useful contributions to solve this problem and to develop the rheometers that have been extensively used over the years. In Meissner's apparatus, as shown in Figure 3, the constant stretching was provided by counter rotating rollers instead of end clamps. In Meissner's apparatus, a polymer sample (which is prepared according to very strict specifications: it is a solid

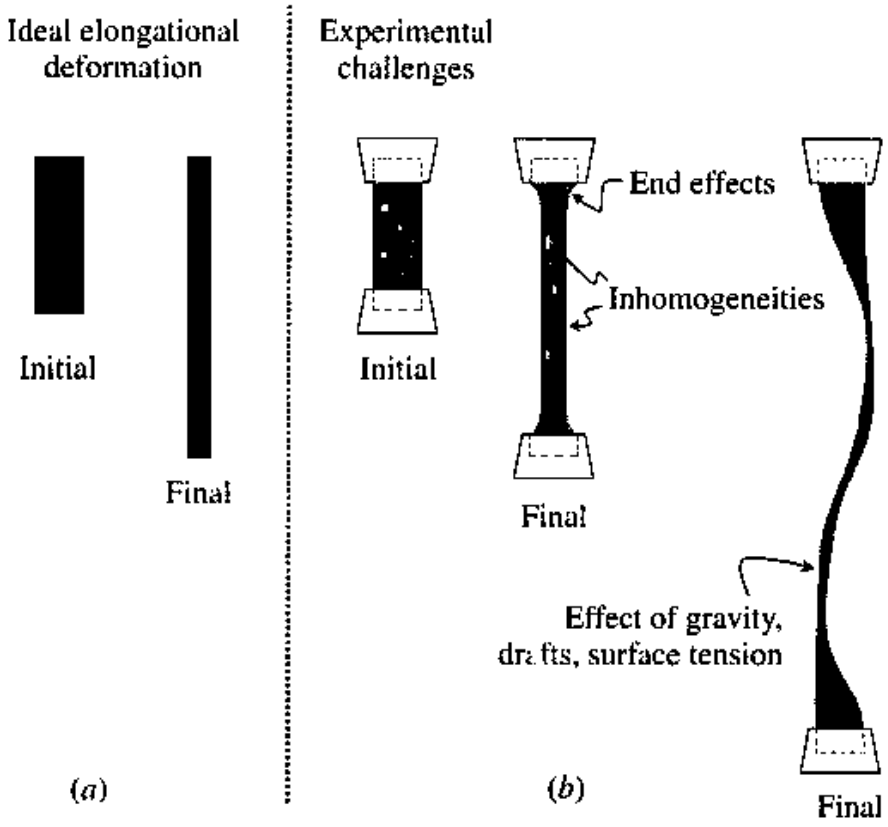

Figure 2: Differences between deformation in (a) ideal uniaxial elongation; (b) difficulties faced in experiments [4]

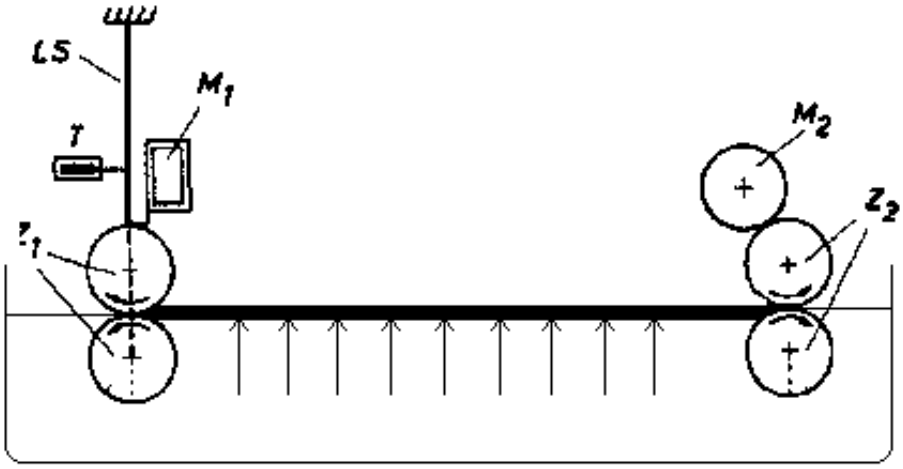

Figure 3: Schematic sketch of Meissner's apparatus, where LS is the leaf spring, Z_1 and Z_2 rotational clamps, M_1 and M_2 the motors, and T is the transducer

rod of a specific diameter) is floating on the surface of a silicon oil bath. The silicon oil is used for heating the sample and compensating gravity by buoyancy. The sample is then heated to the test temperature, after the temperature has reached within 20 degrees Celsius of the melting point of the sample; it is clamped between the two pairs of rotational clamps. These rotational clamps have a constant separation distance from each other and deform the sample at a constant rotational speed to maintain the constant elongational strain rate. The stress can be measured by the degree of deflection of the spring attached to one of the rollers.

In this apparatus, the constant extensional strain rate is provided by the constant rotational speeds of the clamps. Also, it is free from the effects of necking as no necking occurs at the clamps irrespective of the extent of elongation.

Numerous modifications of Meissner's apparatus can be found in the literature [29-32]. Rheometric scientific^{TM} manufactured a commercially available version of the Meissner-type device, which is called the 'Extensional Melt Rheometer'.

Although these devices have enabled measurement of the elongational viscosity, they are prone to several disadvantages. The test temperatures used have to be near the melting point of the polymers, whereas the polymers used in industry are processed at considerably higher temperatures. This is because the polymer is essentially floating on the surface of the oil bath, and it must therefore be in a solid-like state. Due to this reason, only high viscosity polymers can be used in these devices. Also, high strain rates cannot be used, since to keep a high strain rate value constant, the deformation of the material increases exponentially in time, which rapidly leads to the breakage of the

sample. These devices are prone to errors due to inconsistency in sample preparation; the results obtained are not entirely reproducible on the same instrument when used by two different operators. They are also very expensive and complicated to use.

2.2.1.2 Filament stretching:

We cannot use "Meissner-type" viscometers [7, 9, 10] to measure the elongational viscosity of polymer solutions or polymer melts far above the melting point, as these cannot be grabbed at each end and stretched. A variation of "Meissner-type" viscometers was introduced by Sridhar et al. [20]. In this method, a small quantity of the polymer solution is placed between two round plates, and then the plates are separated at a rapid rate to attain a constant elongational rate. A load cell attached to the stationary plate measures the force on the filament. Optical methods or video is used to monitor the deformation rate. In this device, the sample starts from a well-defined initial rest state and, except at the ends of the plates, the sample experiences uniform strain. However, there are disadvantages to this method. The use of this type of apparatus is currently limited to room temperature, and this apparatus still suffers from the problems with inhomogeneities in the flow at the ends and flow instability. The flow at the ends is inhomogeneous uniaxial extensional flow due to gravity, surface tension, and the no-slip boundary condition at the plates.

2.2.1.3 Constant stress method:

In this method, the specimen is stretched at a constant stress value by adjusting the applied force as the sample elongates. This method was first introduced by

Cogswell [14], who used a constant stress device to measure elongational viscosity. The technique was later developed by Münstedt [15-17]; he designed an apparatus that could be operated both at constant elongational rate as well as at constant stress. It was called the 'Universal Extensional Rheometer'.

As seen in the schematic sketch of the 'Universal Extensional Rheometer' from Figure 4, in this apparatus, the sample is vertically suspended in an oil bath. The bath is heated by oil flowing through the hollow walls of the glass vessel. One end of the sample is fixed to a load cell located in the oil bath and its other end is fixed to a thin metal tape, which can be rolled up by a disk. The disk is mounted to the shaft of an extremely rapid DC motor. A displacement transducer serves as an indicator of the sample position. Its signal, recorded as a function of time, gives a direct measurement of the elongation of the sample.

2.2.2 Indirect measurement techniques

As seen in the previous section, the direct measurement techniques for elongational viscosity, such as the stretching or constant stress methods, have several disadvantages. The constant stress systems seem to have an advantage over the constant strain-rate systems as they are quick to reach equilibrium; however, the constant strain-rate systems give more information about the transient behavior [8]. All of the direct measurement techniques for elongational viscosity suffer from disadvantages related to test temperatures, sample preparation, buoyancy, end effects at the clamps, etc. Some of these difficulties can be overcome by using the indirect

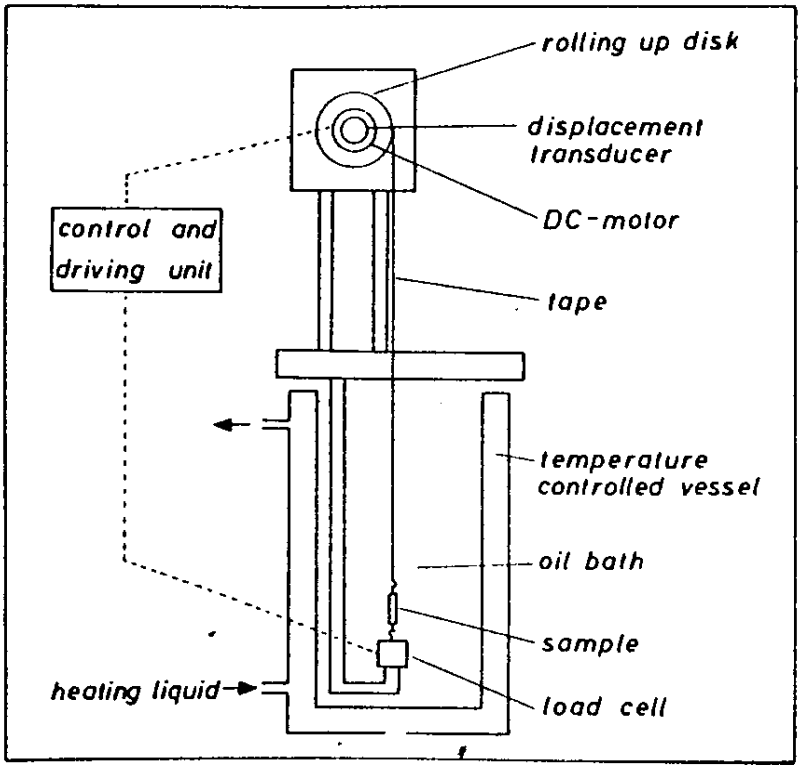

Figure 4: Schematic sketch of the Universal Extensional Rheometer [16]

measurement techniques. As extensional flow is strong in nature, we can use extensional indices. Extensional indices are flows with a mixture of extension and shear; hence they do not give us purely extensional material functions. We will review these methods in this section.

2.2.2.1 Spinning techniques:

Due to its similarity to processing operations, spinning techniques are popular methods of measuring extensional rheological functions. Here, the polymer sample is continuously extruded from a die and stretched by a wheel or vacuum suction, as shown in Figure 5. The force on the tube or on the take-up system is measured. The fiber diameter is measured as a function of the distance along the fiber with the help of an imaging device, such as a camera or video recorder. The extension rate can be determined from measurements of fiber diameter and flow rate. If we assume constant extension rate along the fiber, then the analysis is simpler [2] and leads to a hyperbolic shape. This technique can be used for both polymer melts [33] and for low viscosity polymer solutions [34, 35].

The spinning technique suffers from a lot of errors, such as variable extensional strain rate, effect of shear history in the feed die, die swell, and unstable flow. For low viscosity samples, gravity and inertial effects are significant. It is also nonisothermal. As the strain rate is changing, the force measured over the entire fiber is an integration of stresses due to various strain rates and the shear history in the feed

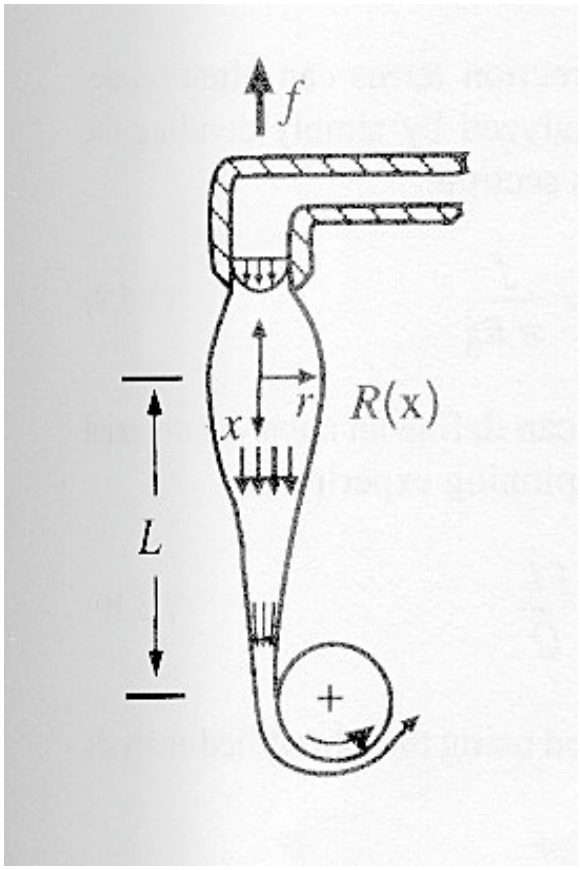

Figure 5: Schematic sketch of a fiber spinning apparatus [2]

die. Hence, we can only measure an apparent uniaxial extensional viscosity with this apparatus, which is not necessarily the same as the true material function.

2.2.2.2 Contraction flows:

In 1972, Cogswell introduced an indirect method of measuring apparent elongational properties by studying converging flows [11]. Here, a melt flowing from a reservoir into a die is observed and pressure drop measurements are made in the die entry region for applied flow rates. The flow into a sudden contraction has a strong extensional characteristic along the centerline; however, this is not a homogeneous elongational flow. Hence, only the apparent elongational viscosity can be calculated. As this flow can be generated in standard capillary rheometers, this technique offered a simpler way to observe the change in the apparent elongational viscosity with respect to different elongational rates.

The flow of the fluids from a reservoir into the die is said to be composed of both shear and extensional flow, as depicted in the Figure 6. The shear flow arises due to the "no-slip" condition at the die walls, whereas the extensional flow arises at the centerline due to the stretching of the material elements. It was suggested by Cogswell that these two components of the flow could be studied separately, and added to give the total flow.

Cogswell [8, 11] and Binding [12, 13] carried out extensive analyses of these contraction flows. They both have made assumptions in the analyses to arrive at feasible solutions. The Binding analysis is more complicated than the Cogswell

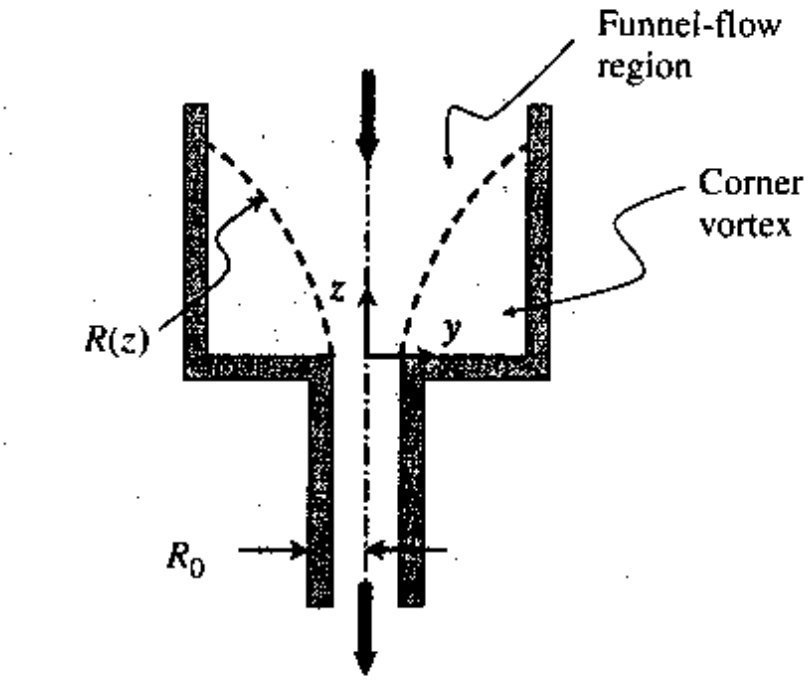

Figure 6: Schematic sketch of the flow geometry addressed by Cogswell [11] and Binding [13] while analyzing contraction flow [4]

analysis, and it is more accurate in the case of commodity polymers, such as linear low-density polyethylene.

In Binding's analysis, elongational viscosity varies with deformation rate, unlike in Cogswell's analysis. Binding and co-workers [36-38] have used this analysis to measure the extensional viscosity of polymer solutions as well. James et al. [18, 19] used this methodology for developing an extensional rheometer. This rheometer can be used to measure elongational properties of polymer solutions and melts at very high Reynolds number.

White et al. [39] provided an excellent overview of the entry flow problem in their review. The most attractive quality of this method is the simplicity of obtaining extensional data, unlike the other methods we have seen so far in this section. However, using contraction flow to get elongational viscosities also has some drawbacks. The flow is unstable at high strain rates, and it is susceptible to pressure effects; therefore it is suited to only low strain rates. Also, the biggest problem is that it is based on a funnel shaped flow, which may not take place under all circumstances. However, this method could be used for wide temperature ranges.

2.2.3 Other measurement techniques

Other techniques for measuring the elongational properties of polymer melts and solutions include the bubble collapse method [40, 41] and stagnation flows [39, 42-47]. The bubble collapse method is less stable, and has not been used as a rheometer. Stagnation flows can be generated using lubricated or unlubricated dies or opposing-jets. Stagnation flows can be used for large strain rates, however, they are

inhomogeneous. They also suffer from shear effects at the walls and instability of the flow.

2.2.4 Summary

In order to summarize all the methods used to measure elongational viscosities, it is very important to look at a report that gives an overview of a collaborative project undertaken by various researchers [48]. In this project, elongational viscosity measurements were made on test fluid M1 [49] using different techniques. The fluid M1, which needed to satisfy many constraints, was prepared at Monash University, Australia. It contained 0.244% polyisobutylene in a mixed solvent consisting of 7% kerosene in polybutene. While comparing the results from all the researchers, it was seen that the various fiber spinning techniques [38, 50-52] yielded data over a similar range (0.75-5s^{-1}) of deformation rates, and that the measured stresses were within an order of magnitude of each other. Converging flow measurements [38, 53] based on Cogswell's analysis gave a much wider range of data, and these measurements used much larger deformation rates. The converging flow channel rheometers of James et al. [54, 55] provided deformation at constant extension rates, but the viscosities measured were lower than those obtained using flow through sudden contractions [38, 53]. The data on extensional viscosities from the opposing-jet rheometers [56, 57] covered the largest range of viscosities (10-1000 Pa s). In general, different opposing-jet rheometers provide good agreement amongst each other; however, the measured viscosities were much lower than those obtained using fiber spinning devices.

As we can see, all the different types of methods described in the sections above for measuring elongational viscosities had several different shortcomings. We can see that some of the drawbacks were eliminated as we went from Meissner's apparatus to using contraction flow and so on, but these rheometers still did not properly function at parameter ranges comparable to those being used in industry (such as high strain-rate flows, high temperatures, etc.). In the coming section, we will discuss a new method for measuring apparent elongational viscosity of polymers using the 'semi-hyperbolically converging die' [21-24].

2.3. Theoretical Development of the Semi-hyperbolically Converging Dies

Collier and coworkers [21-23] have developed a semi-hyperbolically converging die that can be used to generate a uniform uniaxial elongational flow field under specific assumptions. Figure 7 depicts the geometry of this die. To generate a constant elongational strain rate throughout the core of this die, the flow channel decreases in the axial flow direction according to the relation

$$R^2(z) = \frac{C}{z + B} \tag{I.6}$$

where z is the axial flow direction, R is the radius of the flow channel, and C, B are constants. These constants can be determined from the inlet radius R_o at $z = 0$, and the exit radius R_e at $z = L$. They are given by

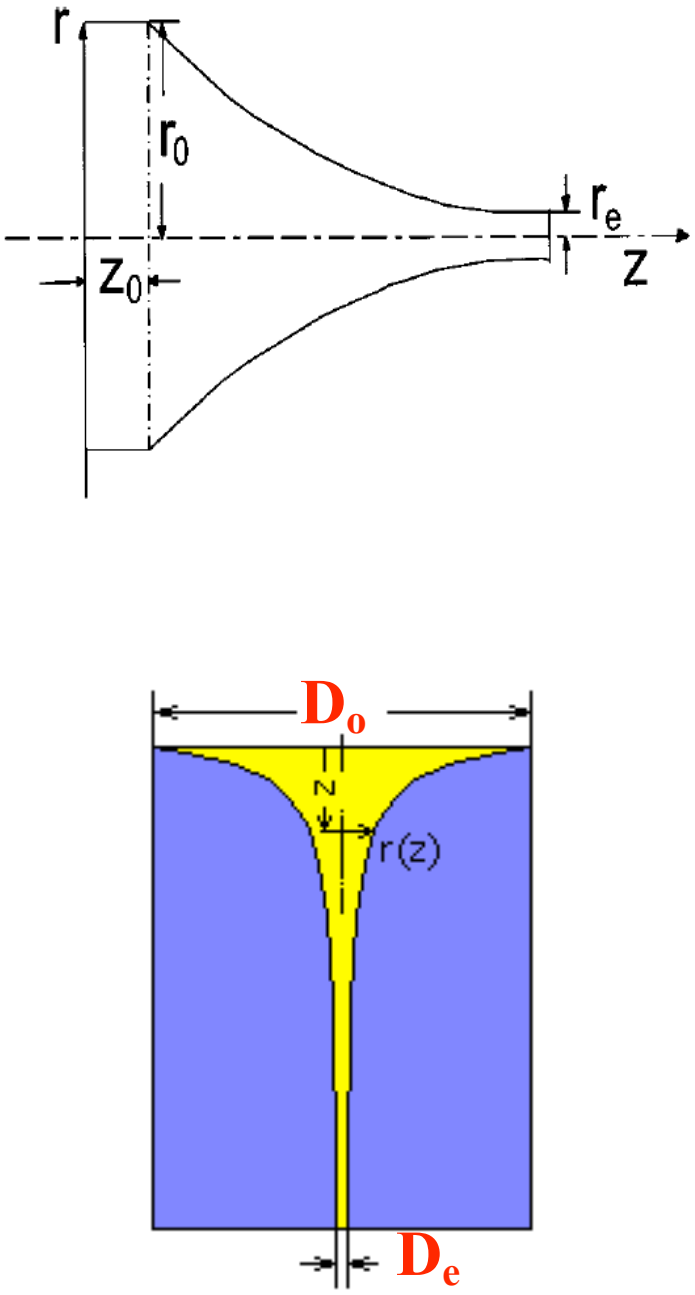

Figure 7: Schematic diagram of semi-hyperbolically convergent die [23]

$$C = L\frac{R_o^2 R_e^2}{R_o^2 - R_e^2} \quad \text{and} \quad B = L\frac{R_e^2}{R_o^2 - R_e^2} \tag{I.7}$$

Dies are designed to have a specific Hencky strain (ε_h) value; we use semi-hyperbolic dies with ε_h values 4, 5, 6 and 7.

In this section, we give a brief overview of the theoretical development of these dies [23]. The shape of the dies was defined in such a way that the interface between the polymer melt or solution and the die wall should be a part of the set of natural streamlines for uniaxial elongational flow. These streamlines are required to have identical conditions, including the value of the stream function, Ψ, which satisfies the continuity equation.

Streamlines form two-dimensional surfaces. For shear-free flows, the potential function, Φ, satisfies the irrotationality equation and describes a constant pressure surface. The potential function and stream function, which satisfy all of the above conditions, are given in cylindrical coordinates as follows. The stream function is

$$\Psi = -\frac{\dot{\varepsilon}}{2} r^2 z \tag{I.8}$$

and the potential function is

$$\Phi = \dot{\varepsilon}\left(\frac{r^2}{4} - \frac{z^2}{2}\right) \tag{I.9}$$

In this system, the pressure, *P*, is directly proportional to $\rho\dot{\varepsilon}\Phi$, where $\dot{\varepsilon}$ is the elongational strain rate, and ρ is the density. The velocity components are

$$v_z = -\frac{1}{r}\frac{\partial \Psi}{\partial r} = -\frac{\partial \Phi}{\partial z} = \dot{\varepsilon} z \tag{I.10}$$

$$v_r = \frac{1}{r}\frac{\partial \Psi}{\partial z} = -\frac{\partial \Phi}{\partial r} = -\frac{\dot{\varepsilon}}{2} r \tag{I.11}$$

$$\frac{\partial v_z}{\partial z} = \dot{\varepsilon},\ \frac{1}{r}\frac{\partial (r v_r)}{\partial r} = -\dot{\varepsilon},\ \frac{\partial v_r}{\partial r} = -\frac{\dot{\varepsilon}}{2} \tag{I.12}$$

Equation (I.12) gives the non-zero velocity gradients.

The basic equations describing the flow are, namely, the equation of continuity, conservation of energy expressed in terms of enthalpy per mass unit, $\hat{H}$, conservation of momentum; and the irrotationality equation for potential flow. Mass, momentum, and energy balances are conserved separately, and are given as

$$\frac{D\rho}{Dt} = -\rho\left(\underline{\nabla} \cdot \underline{v}\right) \tag{I.13}$$

$$\rho \frac{D}{Dt}\underline{v} = -\left(\underline{\nabla} P\right) + \left[\underline{\nabla} \cdot \underline{\underline{\tau}}\right] \tag{I.14}$$

$$\rho \frac{D\hat{H}}{Dt} = -\left(\underline{\nabla} \cdot \underline{q}\right) + \left(\underline{\underline{\tau}} : \underline{\nabla}\underline{v}\right) + \frac{DP}{Dt} \tag{I.15}$$

The irrotationality equation is $\underline{\nabla} \times \underline{v} = 0$, and the material derivative is defined by $\frac{D}{Dt} = \frac{\partial}{\partial t} + \underline{v}.\underline{\nabla}$. Above, $\underline{\underline{\tau}}$ is the stress tensor, $\underline{q}$ is the heat flux, and $\underline{v}$ is the velocity vector field.

The semi-hyperbolic die is designed to produce a constant strain rate; hence the flow should be at constant acceleration, as shown by the velocity gradient equations. However, in the case of shearing flow, this is not valid as the stress gradient acts in the normal direction to the sheared surface, and the stress tensor includes a shearing component. Due to the constant elongational strain rate and strong orientation

development, the flow through the semi-hyperbolically converging die is assumed to be essentially purely elongational. The only significant velocity gradients in this essentially purely elongational flow are in the flow and the radial directions; hence, the only significant non-zero components of the deformation rate tensor, Δ, are the normal components. Whether or not this assumption is valid was initially examined by Feigl et al. [26] (as discussed in Sec. 3.2), and is the continuing subject of this investigation.

The main postulates in the original theoretical development [23] are listed below:

1. The die geometry dictates that the only significant non-zero deformation rate components are the normal components. These normal components are not functions of position; hence the only significant non-zero stress components are the normal components, and the stress components are in turn not functions of position. Therefore, $\underline{\nabla} \cdot \underline{\underline{\tau}} = 0$. The analysis of Feigl et al. [26] removed this assumption.
2. The fluid is incompressible; therefore, $\underline{\nabla} \cdot \underline{v} = 0$.
3. The system is isothermal; therefore, $\underline{\nabla} \cdot \underline{q} = 0$.
4. The inertial terms are negligible; therefore, $\underline{v}.\underline{\nabla v} = 0$.

This assumption was also investigated by Feigl et al. [26].

5. The flow is at steady state; therefore, $\frac{\partial}{\partial t} = 0$.

The constant elongational strain rate of the flow channel ensures that the axial and transverse normal components of the stress tensor, τ_{rr} and τ_{zz}, are also constant. Their values are dictated by the strain rate ($\dot{\varepsilon}$). Experiments performed with a lubricating layer [23] provided an initial indication that shear effects were negligible.

The definition of the true elongational viscosity assumes that any enthalpy change is included:

$$\eta_e = \eta_{eff} + \frac{\Delta H}{\dot{\varepsilon}\varepsilon_h} \tag{I.16}$$

The analysis of Feigl et al. [26] suggests that ΔH can be neglected safely, so that

$$\eta_e = \eta_{eff} \tag{I.17}$$

The elongational strain rate is defined as

$$\dot{\varepsilon} = \left(\frac{v_0}{L}\right)\left(\exp\varepsilon_h - 1\right) \tag{I.18}$$

where ε_h is the Hencky strain as defined previously, L is the centerline length of the die, and v_0 is the initial velocity.

2.4. Wall Slip: Background and Quantification

2.4.1 Background

One of the well-known boundary conditions in fluid flow through a capillary is "no slip" at the walls, which represents the adhesion of the flowing fluid to solid boundaries. However, this assumption does not always hold true. Many times it has

been observed that the fluid slips at the wall, and has a finite velocity instead of a zero velocity at the wall. This often results in extrudate abnormalities, such as sharkskin, stick-slip melt fracture, etc. [58-68]. It has been observed that, in capillary flows, the "no-slip" condition does not hold beyond a critical value of shear stress [60].

Many researchers have tried to study the nature of slip and the causes behind it. From the findings of Kalika and Denn [60] in the studies of capillary extrusion of linear low density polyethylene, we can get a good idea of transitions between various flow regimes. They report a stable flow region below the critical stress, which produces smooth and regular extrudate. At the critical stress, they observed the onset of the sharkskin texture, after which the extrudate showed high-frequency surface variations. At higher stresses, the extrudate showed alternating regions of smooth surface and sharkskin. At even higher stresses, melt fracture was observed, which was indicated by a grossly distorted extrudate. In all, there seems to be a general agreement among the researches that the main cause of slip and the resulting onset of surface irregularities in the extrudate is the breakdown of the adhesion between the polymer and metal interface [58, 60, 62, 63].

During extrusion, the extrudate abnormalities are first observed when the volumetric flow rate exceeds a critical value. As the flow rate increases, the amplitude of these distortions also increases. These instabilities in the flow give rise to extrudate surface defects, and hence the production rates of commercially acceptable products would have to be limited to flow rates below the critical values. This is economically taxing, and hence to improve the process, aids are used frequently.

Processing aids help eliminate these flow instabilities, or help delay their occurrence to higher flow rates. Processing aids used typically include various types of additives or surface coatings. When used in low concentrations, dispersed in the neat polymer, additives act as lubricants. They reduce the apparent viscosities, and hence reduced values of pressures can be used in extrusion. Surface coatings modify the melt-wall interactions and decrease the shear stress required for a specific flow rate. They prevent the rupture of the polymer as it exits the die. Fluoropolymers, stearates, hydrocarbons, boron nitride, and carboxylic acids are examples of some additives that have been the subject of active research in past years [27, 69-80].

2.4.2 Quantification

We can visualize the slip at the wall as depicted in Figure 8. In shear flow, slip decreases the amount of deformation experienced by the fluid. As can be seen from the figure, the shear rate is reduced throughout the region of the flow. However, the shear stress, which depends on the pressure gradient and the flow geometry, remains unchanged at the wall. In case of slip flow, to get the true viscosity we need to calculate the shear rate at the wall.

Mooney's analysis [81] corrects the apparent shear rate for slip. To use this analysis, we need to have flow rate measurements for a given fluid under various pressures at constant temperature in capillaries of various diameters. From this data we can determine the fluidity and surface slip as functions of shear stress. In the following paragraphs, we reproduce Mooney's analysis for completeness. This will also allow us

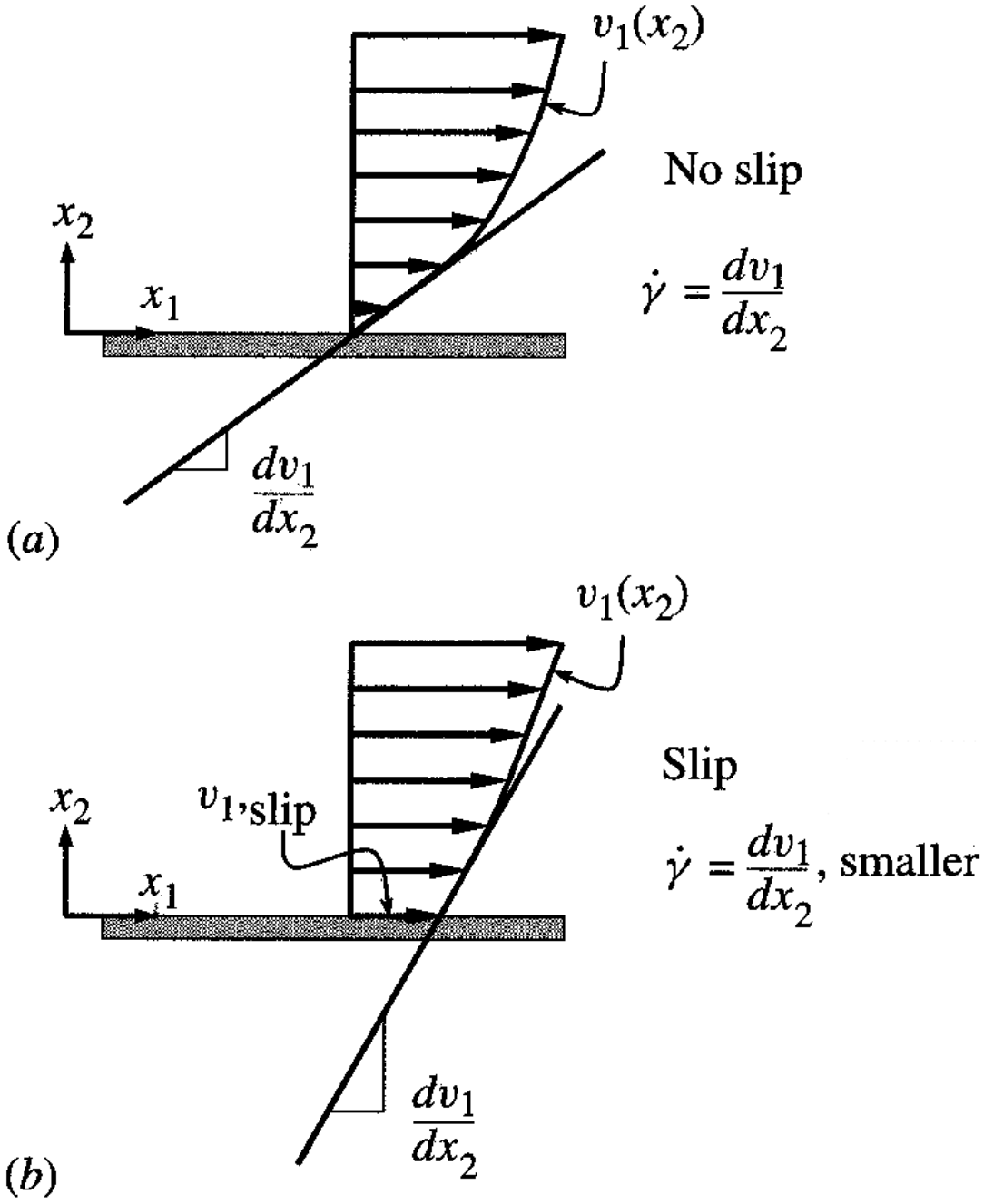

Figure 8: Shear flow in a capillary: (a) no slip; (b) slip at the wall [4]

to modify his analysis in Sec. 3.4 for the semi-hyperbolically converging dies.

The shear stress at a point within a straight-walled capillary is given by the well-known equation [81]

$$\sigma_{rz}(r) = \frac{\pi r^2 (P_0 - P_L)}{2\pi r L} = \frac{r(P_0 - P_L)}{2L} = \frac{rP}{2} \tag{I.19}$$

Here r is the distance from the axis of the capillary, L is the length of the capillary die measured along the z-direction, and P is the pressure gradient, which is given by $\frac{(P_0 - P_L)}{L}$.

The shear stress at the fluid/wall interface is defined as

$$\sigma_{rz}(r)_{wall} = s = \frac{a(P_0 - P_L)}{2L} = \frac{aP}{2} \tag{I.20}$$

where a is the radius of the capillary tube.

The velocity, v_z, at any point in the capillary tube can be given as

$$\int_{v_z(a)}^{v_z(r)} dv_z = \int_a^r \frac{dv_z(r')}{dr'} dr'$$

Since v_z is assumed to be a function of r only, for a Newtonian fluid, the stress is given as,

$$\sigma_{rz}(r) = -\mu \frac{dv_z}{dr}.$$

Hence, $$v_z(r) - v_z(a) = -\int_a^r \frac{\sigma_{rz}(r')}{\mu(r')} dr' \tag{I.21}$$

or

$$v_z(r) = v_z(a) + \int_r^a \frac{\sigma_{rz}(r')}{\mu(r')} dr' = v_{slip} + \int_r^a \frac{\sigma_{rz}(r')}{\mu(r')} dr'$$

Therefore, the velocity at any point is

$$v_z(r) = \frac{aP}{2}\beta + \int_r^a \frac{r'P}{2\mu(r')} dr' = \frac{P}{2}\left[a\beta + \int_r^a \frac{r'}{\mu(r')} dr'\right] \tag{I.22}$$

where β is defined as the coefficient of the slip at the wall stress s, such that $v_{slip} = s\beta$. The flow rate is given by

$$Q = \int_0^a 2\pi r v_z(r) dr$$

$$= \int_0^a 2\pi r \left(\frac{aP}{2}\beta + \int_r^a \frac{r'P}{2\mu(r')} dr'\right) dr$$

$$= \int_0^a \pi P \beta a r dr + \int_0^a 2\pi r \left[\int_r^a \frac{r'P}{2\mu(r')} dr'\right] dr$$

$$Q = \frac{\pi P \beta a^3}{2} + \pi P \int_0^a \left[\int_r^a \frac{r'}{\mu(r')} dr'\right] r dr \tag{I.23}$$

The definite integral in Eq. (I.23) can be simplified using integration by parts:

$$\int_0^a \left[\int_r^a \frac{r'}{\mu(r')} dr'\right] r dr = \left[\frac{r^2}{2}\int_r^a \frac{r'}{\mu(r')} dr'\right]_0^a + \int_0^a \frac{r^2}{2}\frac{d}{dr}\left(\int_r^a \frac{r'}{\mu(r')} dr'\right) dr$$

$$= -\int_0^a \frac{r^2}{2}\left(\frac{r}{\mu(r)}\right) dr$$

$$= \int_0^a \frac{r^3}{2\mu(r)} dr$$

Hence, Eq.(I.23) becomes

$$Q = \frac{\pi P \beta a^3}{2} + \pi P \int_0^a \frac{r^3}{2\mu(r)} dr$$

$$Q = \frac{\pi P}{2}\left[\beta a^3 + \int_0^a \frac{r^3}{\mu(r)} dr\right] \tag{I.24}$$

Using Eq. (I.19), we can change the independent variable from r to σ, since $\sigma_{rz}(r) = \frac{rP}{2}$ and $s = \frac{aP}{2}$. Consequently, the limits of the integration change from $r = 0$ to $\sigma_{rz} = 0$ and from $r = a$ to $\sigma_{rz} = s$:

$$Q = \pi a^2 s\beta + \frac{\pi a^3}{s^3} \int_0^s \frac{{\sigma_{rz}}^3}{\mu(\sigma_{rz})} d\sigma_{rz} \tag{I.25}$$

$$\frac{Q}{\pi a^3} = \frac{s\beta}{a} + \frac{1}{s^3} \int_0^s \frac{{\sigma_{rz}}^3}{\mu(\sigma_{rz})} d\sigma_{rz} \tag{I.26}$$

By differentiating Eq. (I.26) with respect to $\frac{1}{a}$, keeping s constant, we obtain

$$\left.\frac{\partial\left(\frac{Q}{\pi a^3}\right)}{\partial\left(\frac{1}{a}\right)}\right|_s = s\beta = v_{slip} \tag{I.27}$$

According to Eq. (I.27), slip velocity can be determined experimentally. This is the so-called "Mooney Equation". By carrying out experiments with the same test fluid in tubes of differing radius, curves of apparent shear rate versus reciprocal radius can be constructed. The slopes of those curves are then used to determine the slip velocity as a function of the wall shear stress.

CHAPTER 3. WHY THE 'SEMI-HYPERBOLICALLY CONVERGING DIES'?

3.1. Recent Efforts in the Study of 'Abrupt Die Entrance' Flows

In this chapter, we will go over some recent developments toward determining elongational viscosity in *abrupt* die entrance flows, and we will also elucidate the advantages of the proposed approach and the semi-hyperbolically converging die (SHCD). Recent attempts have been made by Gotsis and Odriozola [82] and Beaupre and Gupta [83] to extract elongational viscosities from measured entrance pressure-loss data in abrupt die entrance flows.

The work of Gotsis and Odriozola [82] is based on a modified Cogswell or Binding analysis with simple power-law models for the shear viscosity and a power-law model for the extensional viscosity. It was shown with the help of experimental data for several different materials that, for constant values of strain, the power-law model for the extensional viscosity generally holds true. These authors determined the parameters of the power-law model for elongational viscosity from the knowledge of the parameters of the shear models, the geometry of the die, entrance pressure drop, and the flow rate. Then, the elongational viscosity data taken from a Meissner-type device was integrated over strain to interpret the die entrance data as an *average*, over strain, of the material's true transient elongational viscosity. The two sets of data

agreed well over certain ranges of strain rate for some of the materials at constant strain.

In another recent effort with the abrupt die entrance techniques, Zatloukal et al. [84] proposed and verified improvements that eliminate some of the shortcomings reported previously. They proposed a new procedure, the so-called ‘effective entry length correction, to improve the capability of the Cogswell, Binding, and Gibson models to predict the transition of the extensional viscosity from linear viscoelastic behavior into the non-linear flow regime. Their simulations have shown that these suggested improvements lead to effective evaluation of the extensional viscosity data from capillary die measurements.

Beaupre and Gupta [83] have combined measured entrance pressure-loss data in an abrupt die entrance flow with finite element (FE) simulations for estimating elongational viscosity. Their approach involves optimization of the material-dependent parameters in their model for elongational viscosity by minimizing the difference between the measurements of pressure loss and those predicted by the FE simulations. They then use these parameters in the model for various strain rates to generate predictions of elongational viscosity as a function of strain rate. The predicted elongational viscosity is assumed to be the material's true elongational viscosity. The model used there is essentially a generalized Newtonian model, which has been assumed to describe the stress-strain relationship of the polymers under consideration. However, this type of model is only applicable to steady-state flows. The stress-strain relationship of viscoelastic fluids like polymers is more complicated

as the stress experienced by them depends on the strain history of the flow. Hence any realistic constitutive models attempting to describe them must take into account both transient and steady-state effects. Therefore, the model used by Beaupre and Gupta [83], although computationally easier to use than a truly time-dependent viscoelastic constitutive equation of integral and differential type, cannot depict the transient behavior of these polymers.

To account for the transient effects in polymers and predict their behavior closely in viscometric and complex flows, constitutive equations of differential type and integral type are used. In the study by Feigl et al. [26], where the finite element method was applied to the flow of polymeric fluids through the semi-hyperbolically convergent die, the integral type of constitutive model was used. This model accounted for transient effects and had an inherent viscoelastic nature.

3.2. Recent Study of the 'Semi-hyperbolically Converging Dies'

Converging die entrance geometries have been used by both James et al. [18, 19] and Collier and coworkers [21, 23-25, 85, 86] to extract the elongational viscosity data. However, even though both these research groups proposed the use of a semi-hyperbolically converging die, their analyses and expressions for the elongational viscosity differed. The validity of the assumptions and analysis of James et al. was scrutinized by Park et al. [87] using numerical simulation of the fluid M1 in the converging die entrance geometry. They reported disagreement between the

simulations and the elongational viscosities measured by James et al. The study by Feigl et al. [26] investigated the analysis of semi-hyperbolically converging dies performed by Collier et al. rigorously, and they have reported good agreement between experimental data taken using the semi-hyperbolically converging die with that obtained from the simulation data.

Feigl et al. [26] studied the velocity profile developed in the semi-hyperbolically dies under two different cases. The first case assumed that the fluid does not slip along the wall of the die. Figure 9 (a) shows the axial velocity profiles of the LDPE melt within the die of Hencky strain $\dot{\varepsilon}_h$ = 6 at various cross-sections for a volumetric flow rate of Q = 10 mm^3/s. This result for the axial velocity profiles shows the presence of notable shear effects throughout the die. This negates the 'shear-free' flow assumed in the analysis. Hence, if there is no slip present along the walls of the SHCD, then it does not provide a good means to determine the true elongational viscosity. Also, from Figure 9 (b), we can see that the dashed horizontal lines, which are representing the elongational rate $\dot{\varepsilon}$ in the elongational flow, become nearly constant within the die along each streamline. $\dot{\varepsilon}$ does not reach the same value along all streamlines, but rather $\dot{\varepsilon}$ increases as the radial distance of the streamline increases.

In the second case, the fluid is allowed to slip along the tube walls after entering the die. The results of this case can be seen in Figure 10, where part (a) shows the axial velocity profiles of the low-density polyethylene melt within the die of

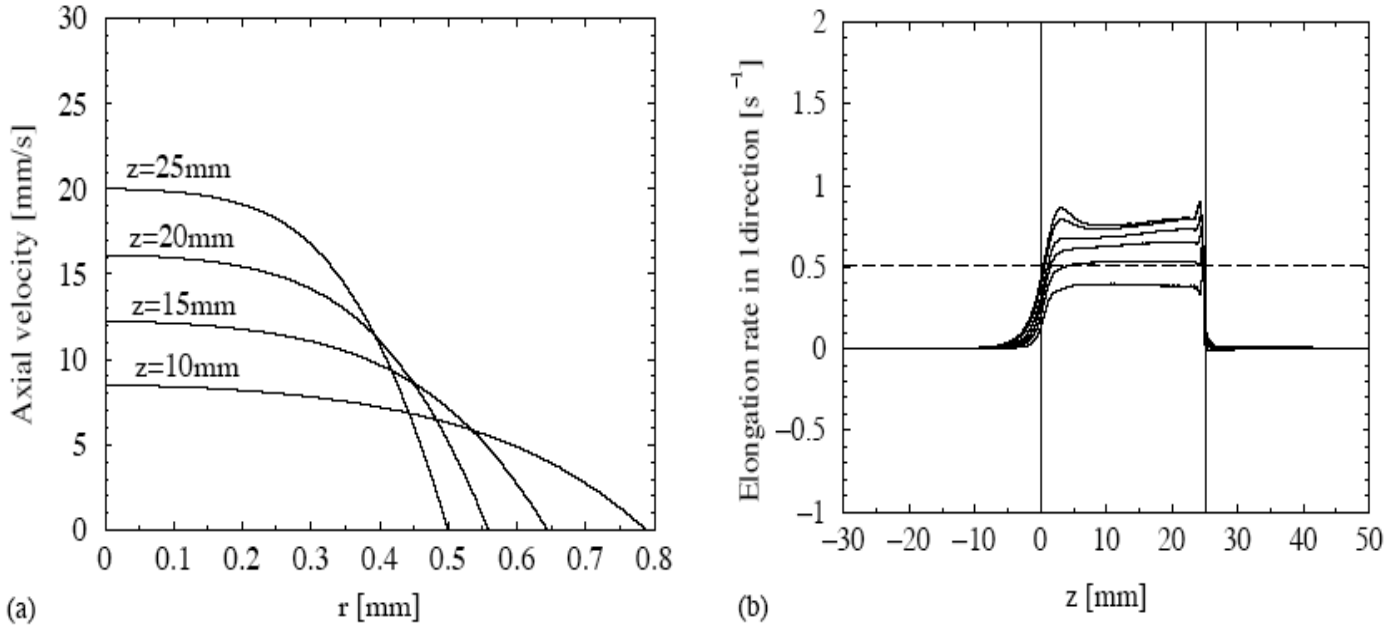

Figure 9: Results for the LDPE melt with no-slip boundary conditions for a Hencky strain ε_h= 6 and a volumetric flow rate of Q = 10 mm^3⁄s showing (a) axial velocity profiles at various cross-sections and (b) elongation rates along various streamlines. The elongation rate curves in (b) correspond to the streamlines (from top to bottom) r = 1, 3, 5, 6, 7 and 8 mm, where r is the radial position of the streamline in the fully-developed upstream flow. The dashed horizontal line in (b) indicates the value of $\dot{\varepsilon}$ in elongational flow [26]

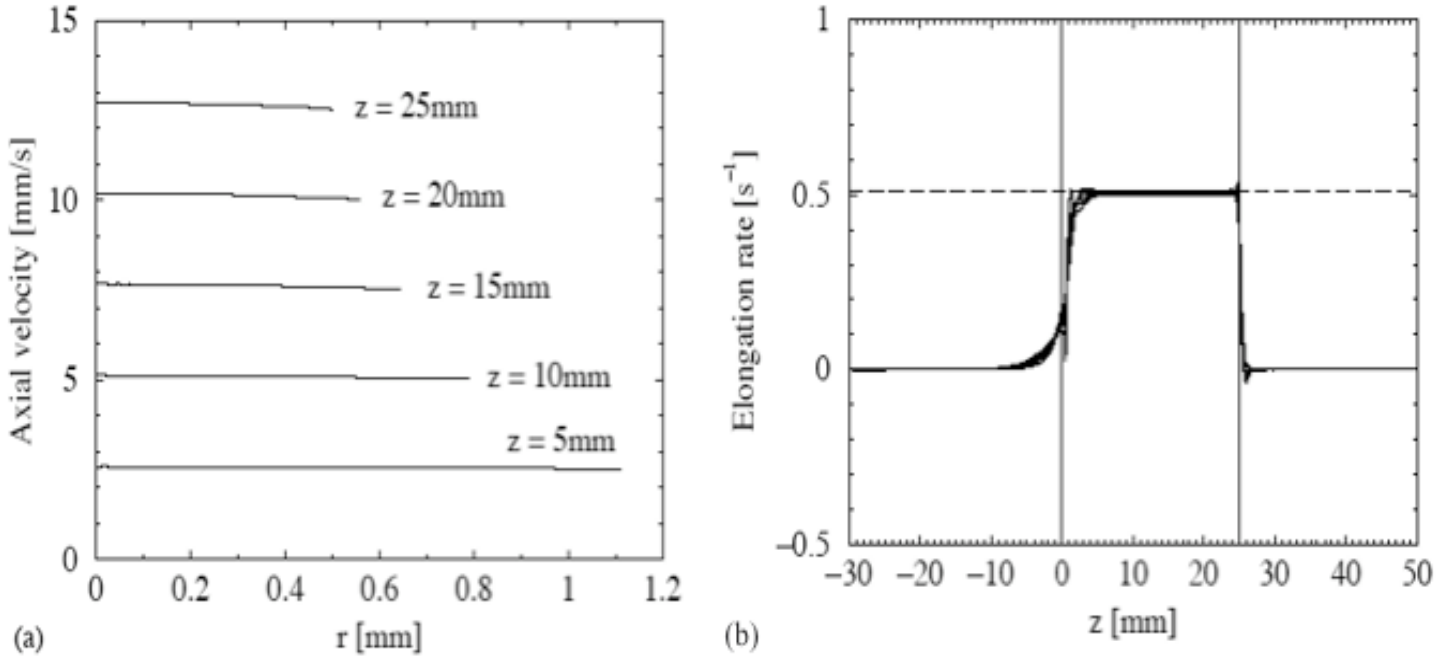

Figure 10: Results for the LDPE melt with the slip boundary conditions for a Hencky strain ε_h = 6 and a volumetric flow rate of Q = 10 mm^3⁄s showing (a) axial velocity profiles at various cross-sections and (b) elongation rates along various streamlines. The dashed horizontal line in (b) indicates the value of $\dot{\varepsilon}$ in elongational flow [26]

Hencky $\dot{\varepsilon}_h$ = 6 at various cross-sections for a volumetric flow rate of Q = 10 mm^3/s. The axial velocity profiles are shown as functions of r for several axial cross sections, which are constant throughout the die. Figure 10 (b) shows that elongational rate, except for a short distance near the die entry, is constant and identical along several streamlines. Thus, these results indicate the presence of slip is necessary to generate a nearly uniaxial elongational flow field inside of the semi-hyperbolically converging dies.

Comparison between Meissner data and SHCD data:

Figure 11 shows the comparison between the data taken by Hachmann and Meissner (filled symbols) and data taken using the semi-hyperbolically converging dies by Petrovan (open symbols) for two different polymers. The top figure shows data for LDPE at 150^{o}C, where we can see that the Meissner data is limited to lower strain rates while the SHCD can be used over a large range of strain rates. The data from these two different sets shows good agreement.

The second plot in Figure 11 shows the comparison between the data for polystyrene at 170^{o}C. This data, although taken over the similar strain rate range, does not agree very well. The reason behind this disagreement between the two sets of data is subject of active study in our research program. Why do SHCDs work well for one polymer and not the other? One possible reason is that the two polymers experience different degrees of slip in the SHCDs. In other words, polymers that exhibit a higher degree of slip will experience a nearly perfect uniaxial elongational

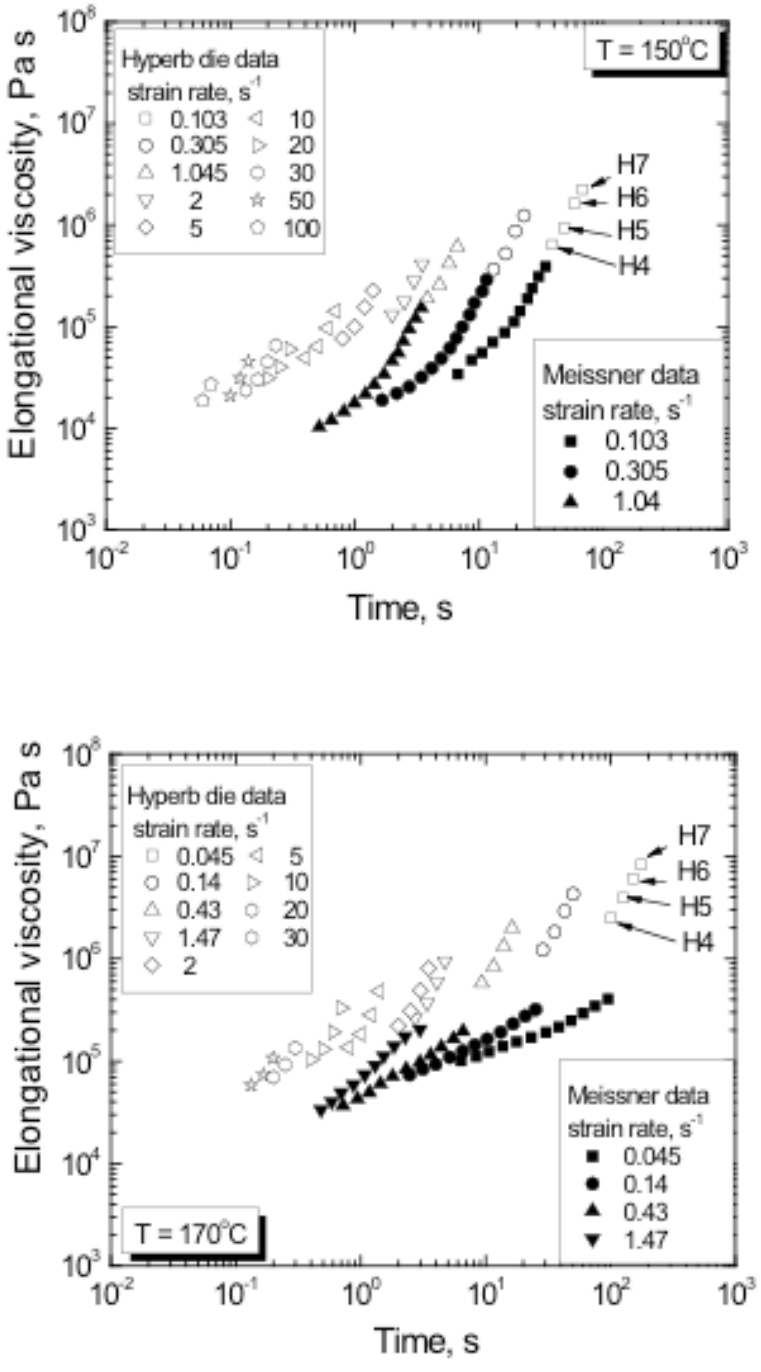

Figure 11: Comparison between the data taken by Meissner and by using the semi-hyperbolically converging die for LDPE 1810H (top figure) and for polystyrene PS 158K (bottom)

flow as they flow through the die, whereas the converse statement is not true. Thus, for polymers with a high degree of slip, the assumptions used in the analysis of these dies are valid, whereas for polymers with a low degree of slip, the assumptions are not valid.

Our working hypothesis going forward is that the amount of slip experienced by a flowing polymeric fluid is related to its degree of orientation in a particular flow field. When the degree of orientation is low, the fluid will experience a low degree of slip, and vice-versa. This statement is already implicitly verified by many experimental studies of slip in shear flow. These studies universally show the increase of slip velocity with increasing wall shear stress, which is corresponds to increased orientation. Given the particularly strong elongational flow characteristics of the SHCDs (even in the case of no-slip boundary conditions – see Figure 9), it is thus hypothesized that the SHCDs will produce a much greater degree of orientation of the polymer than it would have experienced in a purely shear flow. Consequently, the SHCDs exhibit higher degrees of slip than in straight-walled tubes. Since this is exactly the condition necessary to produce a purely elongational flow field in these dies, it warrants further study. Thus the purpose of Part I of this dissertation is to determine the degree of slip present in SHCDs under various conditions.

3.3. Advantages of the 'Semi-hyperbolically Converging Dies'

Using the semi-hyperbolically converging die has certain advantages over the abrupt die entrance methods. As in Meissner-type devices, the elongational viscosity

data taken in an abrupt die entrance flow is restricted to low strains and strain rates. Also, the abrupt die entrance models require both shear material functions and the elongational viscosity functions due to the presence of shear effects in the flow. The semi-hyperbolically converging die requires no consideration of the lingering shear effects, provided that the full wall-slip condition bears out. Furthermore, steady shear data is needed to fix the parameters in the shear models so that elongational viscosity can be predicted using the specified model. No additional viscometric data is required when using the semi-hyperbolically converging die. In the abrupt die entrance approach, it is not exactly known how to convert the raw experimental data obtained to transient data in the form of elongational viscosity versus time at constant strain rates, while in case of the semi-hyperbolically converging die, this can be done using the theoretical residence time of a fluid element in the die, which is given by $t = \varepsilon_H / \dot{\varepsilon}$.

Also, in the techniques involving abrupt die entrance flow, the streamlines do not have a uniform value of strain rate, as in the case of the semi-hyperbolically converging die. A further advantage of the SHCD is that one is not limited to low temperatures near the melting point, which are of little interest industrially.

3.4. Derivation of the Slip Velocity Equation for the Semi-hyperbolically Converging Dies

In this section, we will derive the equation for slip velocity in the semi-hyperbolically converging die, which will be used for quantifying the amount of slip

taking place in these dies from experimental results. Apart from the computational study conducted by Feigl et al. [26], there are other results that suggest that there is a greater amount of slip taking place in these dies than in case of the capillary dies. For instance, the experimentation with the semi-hyperbolically converging dies has often revealed extrudate abnormalities typical of the onset of the slip flow [85]. Hence, as mentioned in Sec. 1.2, the purpose of this study is to investigate and validate the nature of the velocity profile developing in the semi-hyperbolically converging dies, especially the amount of slip occurring within the die. If we quantify the slip velocity at the wall of this die, then it can be used to validate the nature of the velocity profile inside the die. In the end, all this information can be related to the elongational viscosity measured using this die. We plan to use additives along with the neat polymers to investigate how much of the slip observed is due to the additive and how much of it is due to the inherent nature of the dies.

The Mooney analysis has been discussed in Section 2.4, and more refinements have been made to the original analysis by many researchers [68, 88]. We intend to extend the original methodology to measurements made using the semi-hyperbolically converging dies. However, the original analysis performed by Mooney cannot be directly applied to these semi-hyperbolically converging dies, as they differ in some respects from the original conditions. First, in the original analysis, constant-radius capillary dies were used, whereas in the case of semi-hyperbolic converging dies, the radius decreases with axial distance (see Figure 7). Second, the flow is no longer a purely shear flow, but it has strong extensional characteristics. The shear contribution

to the flow field is hopefully almost negligible, and limited to a boundary region near the die wall. Indeed, this point is suggested by the analysis of Feigl et al. [26]. In that study, a typical industrial LDPE was simulated in the SHCD using a sophisticated constitutive model of integral type, namely, a factorized Rivlin–Sawyers equation. Even in the case of absolutely no-slip boundary conditions, the shear effects in this die were confined close to the die walls. As more slip occurs, the shear region gets pushed closer and closer to the walls, until it eventually disappears completely for full-slip boundary conditions.

Performing a similar derivation to the Mooney analysis for straight-walled capillary tubes is very difficult for the SHCD under general conditions. This would involve numerical integration of the partial differential equations for the momentum equation, coupled with a constitutive model for the fluid under investigation. Although such a detailed simulation might be warranted for future work, we need some approximate method by which we can judge whether or not our gross hypothesis is correct. In other words, we want to make some limiting assumptions, whereby we can get an easy-to-use version of the Mooney equation to judge if the geometry of the SHCD really does induce more slip than in a capillary die of the same length.

The assumption we are going to make to simplify the analysis is the following. We are going to assume a priori that a fair degree of slip is occurring within the SHCD. According to the results of Feigl et al. [26], the shear effects are then all contained within a very thin boundary layer near the die walls. As such, the bulk of the flow is experiencing purely elongational flow. Hence, the pressure drop measured by

the die is almost entirely due to the elongational effects. Whether or not this assumption is valid can be indirectly tested experimentally by comparing measured pressure drops in the dies for neat polymers with that for the same polymer plus viscosity reducing additives. These experiments have been carried out, as described below, and seem to indicate that this assumption is reasonably valid.

Based upon our assumption, the bulk fluid is going to follow the stream function imposed by the shape of the SHCD. Therefore, we can set [26]

$$\Psi = -\frac{r^2 z}{2} \tag{I.28}$$

which implies that

$$d\Psi = d\left(\frac{-r^2 z}{2}\right) = -rz\,dr - \frac{r^2}{2}dz \tag{I.29}$$

However, along a streamline, $d\Psi = 0$, so that $dr = -\frac{r}{2z}dz$.

In these dies, the z-component of the velocity is a function of both r and z. Consequently,

$$dv_z = \frac{\partial v_z}{\partial r}dr + \frac{\partial v_z}{\partial z}dz \tag{I.30}$$

but given Eq. (I.29) and the fact that $\frac{\partial v_z}{\partial r} = \dot{\gamma}$ and $\frac{\partial v_z}{\partial z} = \dot{\varepsilon}$, this expression can be written as

$$dv_z = \dot{\gamma}\,dr - \frac{2\dot{\varepsilon} z}{r}dr \tag{I.31}$$

Note that the shear stress is still defined by $\sigma_{rz}(r,z) = -\mu(r,z)\,\dot{\gamma}(r,z)$. Also note that, under our primary assumption, $\dot{\varepsilon}$ is a constant. Therefore, at any location in the die, v_z is given by the integral of Eq. (I.31):

$$v_z(r,z) - v_z(R,z) = -\int_R^r \frac{\sigma_{rz}(r',z)}{\mu(r',z)}\,dr' - 2\dot{\varepsilon} z \int_R^r \frac{dr'}{r'} \tag{I.32}$$

where $R(z)$ is the die radius at any value of z. Evaluating the second integral in this expression leads to

$$v_z(r,z) = v_{slip}(z) + \int_r^R \frac{\sigma_{rz}(r',z)}{\mu(r',z)}\,dr' - 2\dot{\varepsilon} z \ln\frac{r}{R} \tag{I.33}$$

This equation should be valid near to the wall of the die given our primary assumption. As before, v_{slip} can be expressed as $v_{slip} = s(z)\beta$, where s is the shear stress at the wall.

Since the radius of the die changes axially, the flow rate in the die is also a function of z. The expression for the flow rate is given by

$$Q(z) = \int_0^R 2\pi r\, v_z(r,z)\,dr \tag{I.34}$$

Substitution of Eq. (I.33) into this expression yields

$$Q(z) = \pi R^2 s(z)\beta + 2\pi \int_0^R \left(r \int_r^R \frac{\sigma_{rz}(r',z)}{\mu(r',z)}\,dr' \right) dr - 4\pi \dot{\varepsilon} z \int_0^R r \ln\frac{r}{R}\,dr \tag{I.35}$$

The third term on the right side of Eq. (I.35) can be solved via integration by parts to give $\pi \dot{\varepsilon} z R^2$. The second term on the right side can also be solved via integration by parts, under the definition

$$\frac{\partial g(r,z)}{\partial r} = \frac{\sigma_{rz}(r,z)}{\mu(r,z)} \tag{I.36}$$

for the function g. Hence,

$$2\pi \int_0^R \left(r \int_r^R \frac{\partial g}{\partial r'} dr' \right) dr = \left[\pi r^2 \int_r^R \frac{\partial g}{\partial r'} dr' \right]_0^R - \pi \int_0^R r^2 \frac{\partial}{\partial r} \left(\int_r^R \frac{\partial g}{\partial r'} dr' \right) dr \tag{I.37}$$

The first term on the right side vanishes, leaving

$$2\pi \int_0^R \left(r \int_r^R \frac{\partial g}{\partial r'} dr' \right) dr = -\pi \int_0^R r^2 \frac{\partial}{\partial r} \big(g(R,Z) - g(r,z) \big) dr$$

$$= \pi \int_0^R r^2 \frac{\sigma_{rz}(r,z)}{\mu(r,z)} dr \tag{I.38}$$

In the shear layer near the wall, the shear stress is still proportional to r, as in the Mooney analysis, so that changing variables from r to σ_{rz} yields

$$Q(z) = \pi R^2 s\beta + \frac{\pi R^3}{s^3} \int_0^s \frac{{\sigma_{rz}}^3}{\mu} d\sigma + \pi \dot{\varepsilon} z R^2 \tag{I.39}$$

or

$$\frac{Q}{\pi R^3} = \frac{s\beta}{R} + \frac{1}{s^3} \int_0^s \frac{\sigma^3}{\mu} d\sigma + \frac{\dot{\varepsilon} z}{R} \tag{I.40}$$

Moving the last term on the right side of Eq. (I.40) to the left side, and then differentiating with respect to $\frac{1}{R}$, gives

$$\left.\frac{\partial\left(\frac{Q}{\pi R^3}-\frac{\dot{\varepsilon} z}{R}\right)}{\partial\left(\frac{1}{R}\right)}\right|_{z,s} = s\beta = v_{slip} \tag{I.41}$$

This is the equivalent expression for an SHCD as the original equation of Mooney for a straight-walled capillary. However, it is very important to keep in mind the assumption under which it was derived. The Mooney equation is universally valid, whereas Eq. (I.41) is only valid if the assumptions leading to it are valid. In other words, the fluid in the die has to be experiencing a large degree of slip for the preceding analysis to quantify even approximately the slip velocity.

CHAPTER 4. MATERIALS, EQUIPMENT, AND DATA ACQUISITION

4.1. Materials

We have conducted experiments with three different polymers, namely polypropylene (PP), low-density polyethylene (LDPE), and high-density polyethylene (HDPE). The polymer properties, such as melt index and density values, are listed in Table 1.

To study the effects of wall slip, we used a lubricant. We used commercially available stearic acid ($C_{18}H_{36}O_2$) from Fisher Scientific. The molecular weight of the stearic acid was 284.49 g/mole, and it mainly consists of steric acid ($C_{18}H_{36}O_2$) and palmitic acid ($C_{16}H_{32}O_2$). The melting point of stearic acid is 67-69^{o}C and the boiling point is reported to be 361^{o}C at 760mm Hg.

Various weight percentages of stearic acid were initially added to the neat thermoplastics, namely 1%, 2% and 5%. After the preliminary analysis was carried out, we used 2% stearic acid with the neat thermoplastics to perform the experiments to quantify the amount of slip. The stearic acid was added to the polymer samples using a twin screw extruder at about 200^{o}C. The extrudate was then pelletized using an in-line pelletizer. All the experiments were carried out at 220°C.

Table 1: Resin properties for PP, LDPE, and HDPE

Resin properties	PP	LDPE	HDPE
Melt Index (g/10min)	24 ASTM D1238	7.5 ExxonMobil Method	2.4 ExxonMobil Method
Density ($g/cm^{3)}$	0.90 ASTM D792	0.915 ExxonMobil Method	0.964 ExxonMobil Method

4.2. Equipment and Data Acquisition

The viscosity measurements were performed using the Advanced Capillary Extrusion Rheometer (ACER) and the Advanced Rheometric Expansion System (ARES) manufactured by Rheometric Scientific™. Their schematics are shown in Figures 12 and 13.

4.2.1 Advanced Capillary Extrusion Rheometer (ACER)

The structure of ACER can be construed from the schematic shown in Figure 12. The pellets of polymer are charged into the barrel. Three independent electrical band heaters located around the cylindrical barrel are used for heating. After the polymer and additive have melted and reached the desired steady-state temperature we start the experiment. A ram is used to extrude the sample. The velocity of the ram can be controlled to apply a certain flow rate. ACER performs each measurement by pushing the ram through a uniformly-bored cylinder, which is filled with the sample. From the cylinder, which acts as a reservoir, the sample is further forced through a die of known diameter and length. The ACER records the pressures via a transducer located right above the entrance of the die. ACER calculates the apparent shear rate or shear viscosity from the measured steady-state pressure, depending on the test. ACER can also apply the Bagley and Cogswell corrections. The capillary die, when replaced by the semi-hyperbolically converging die, enables us to use ACER for elongational measurements.

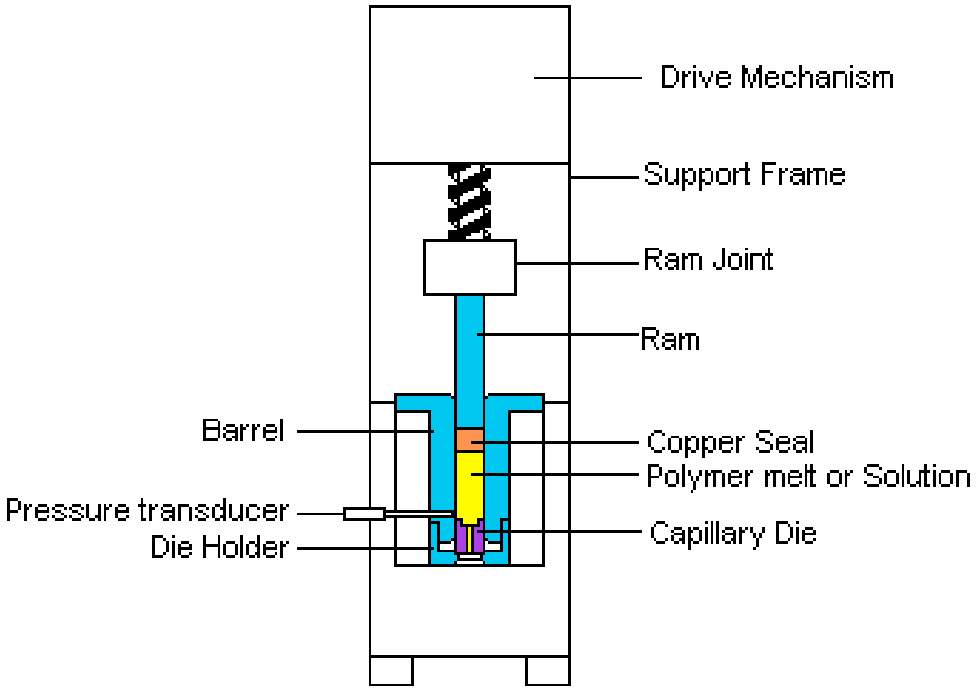

Figure 12: Schematic diagram of the Advanced Capillary Extrusion Rheometer (ACER)

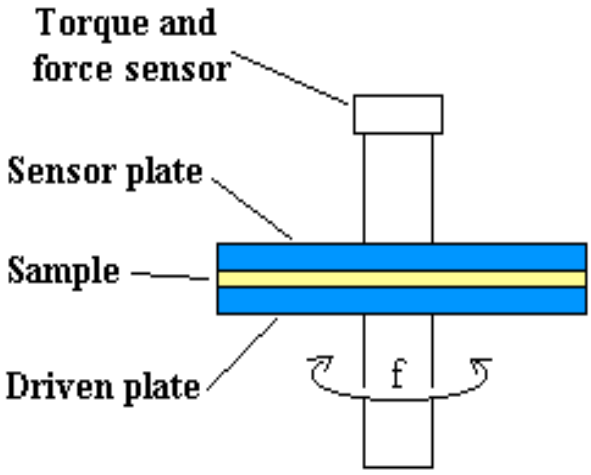

Figure 13: Simplified schematic of the Advanced Rheometric Expansion System (ARES)

4.2.2 Advanced Rheometric Expansion System (ARES)

A simplified schematic of the ARES with parallel plate geometry is shown in Figure 13. A cone-plate geometry was actually used for the measurements. In ARES, the lower plate of the rheometer is attached to a motor and the upper plate is attached to the torque and force transducers. The motor has two modes of rotation, namely, steady and oscillatory mode. ARES has two transducers with different torque ranges (but only one normal force range). During a test, the instrument can switch from the lower range transducer to the higher range transducer automatically, if needed. The plates are heated in a forced air convection oven. Two resistive heaters are mounted in the oven, which control the temperature of the compressed air or nitrogen used for heating. The temperature of the lower plate can also be controlled by a platinum resistive thermometer. The polymer needs to be loaded between the plates in the form of circular disks. These disks were prepared by compression molding at the experimental temperatures.

Figures 12 and 13 are reproduced with the permission from Dr. Petrovan, Chemical Engineering Department, University of Tennessee, Knoxville.

4.3. Types of Experiments

We wanted to obtain both shear and elongational experimental data on the samples to study the nature of wall slip. Steady shear-rate sweeps at higher shear rates and elongational data were obtained using ACER. Transient shear stress data and

dynamic frequency sweep data were gathered using ARES. We also used ARES to obtain the steady-state shear data at low shear rates.

Steady-state shear viscosity data:

We gathered shear viscosity data over a wide range of shear rates (0.001 s^{-1}-10000 s^{-1}). To cover the entire range of shear rates, we used ARES at low shear rates and ACER at higher shear rates.

Elongational data:

Four semi-hyperbolically convergent dies of Hencky strains 4, 5, 6, and 7 were used to obtain the elongational viscosity data. The current commercial software of the ACER accounts for the unconventional shape of the semi-hyperbolic dies. Knowing the measured steady-state pressure from the experiment, elongational strain rate, and Hencky strain, the steady-state effective elongational viscosity can be calculated.

CHAPTER 5. RESULTS AND DISCUSSION

5.1. Shear Experiments

In this section, we will present results of the shear experiments obtained using ARES and ACER. We will also give a detailed description of the slip velocity calculation from the shear stress sweep data.

5.1.1 Characterization of polymer samples

Various polymer samples were characterized using ARES to determine the extent of reduction in the shear viscosity values after the additive was used compared with the neat thermoplastics. We used different weight percentages of the stearic acid, namely, 1, 2, and 5% in these thermoplastics. Steady-state shear rate sweeps were performed on all these samples using the cone-plate geometry at 220^{o}C, and the reduction observed in the shear viscosity with respect to the shear viscosity of the neat thermoplastic is reported here.

5.1.1.1 Experiments with polypropylene (PP)

In Figure 14, shear stress is plotted against shear rate for four different polymer samples namely, PP, PP+1% stearic acid (SA), PP+2% SA and PP+5% SA. We observe reduction in the shear stress in all the samples that contained the stearic acid additive. We see that the extent of shear stress reduction is large between PP and PP+1% SA, about 30%. The shear stress reduction continues to increase with increasing percentages of the stearic acid, although the rate of reduction is very small.

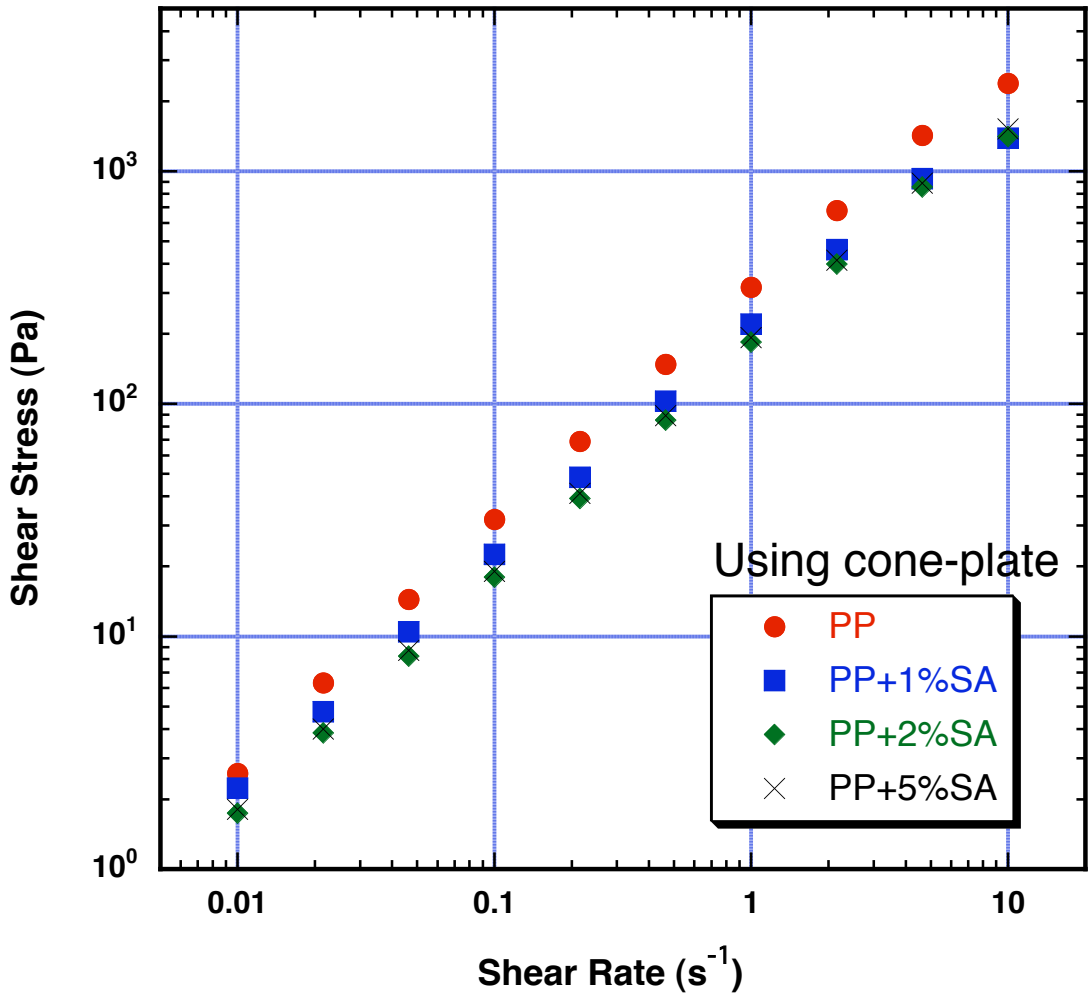

Figure 14: Effects of the stearic acid additive on the shear stress of PP in pure homogeneous shear flow using a cone-plate geometry and 220°C

with 5% stearic acid, we observe about 40% reduction in the shear stress values on average.

5.1.1.2 Experiments with high-density polyethylene (HDPE)

In Figure 15, shear stress is plotted against shear rate for HDPE, HDPE+1% SA, and HDPE +2% SA in the cone-plate geometry at 200^{o}C. As in the case of PP, we observe reduction in the shear stress as we go from the neat HDPE to the samples that contain small quantities of stearic acid. We also see similar behavior regarding the extent of shear stress reduction. With 1% stearic acid, we observe reduction in the shear stress values up to about 27%, and with 2% additive the largest reduction in shear stress observed is about 28%. Hence, we can see that the extent of shear stress reduction is not overly dependent on the weight percentage of additive used, irrespective of the type of the polymer.

5.1.1.3 Experiments with low-density polyethylene (LDPE)

We learned from the experiments with PP and HDPE that a higher weight percentage of the additive does not bring about much more reduction in the shear stress. Therefore, in the case of LDPE, we only used 1% of stearic acid to quantify the amount of reduction. The results are shown in Figure 16 where shear stress reduction of as much as 51.6% is obtained. We also see from the Figures 14 - 16 that the degree of shear stress reduction decreases as the shear rate increases, and the highest shear stress reduction is recorded at the lower shear rates in each experiment.

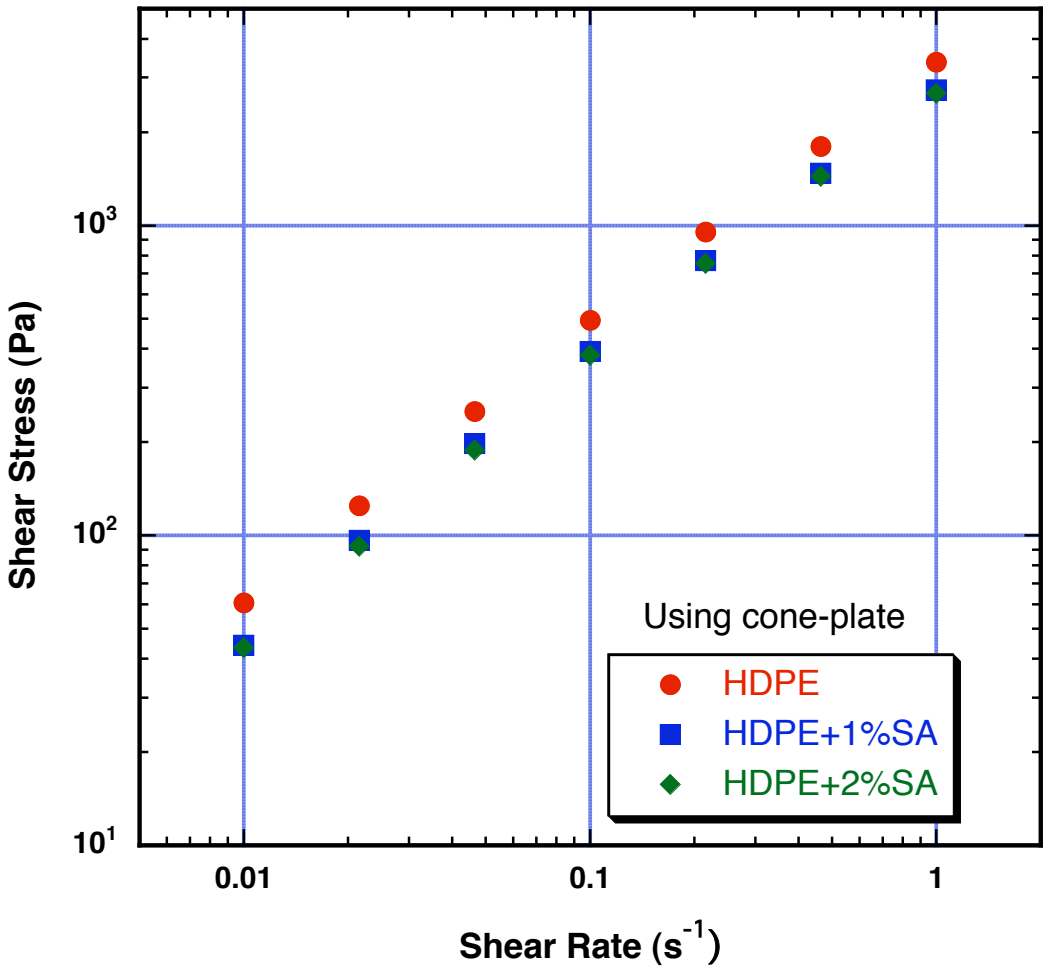

Figure 15: Effects of the stearic acid additive on the shear stress of HDPE in pure homogeneous shear flow using a cone-plate geometry and 200°C

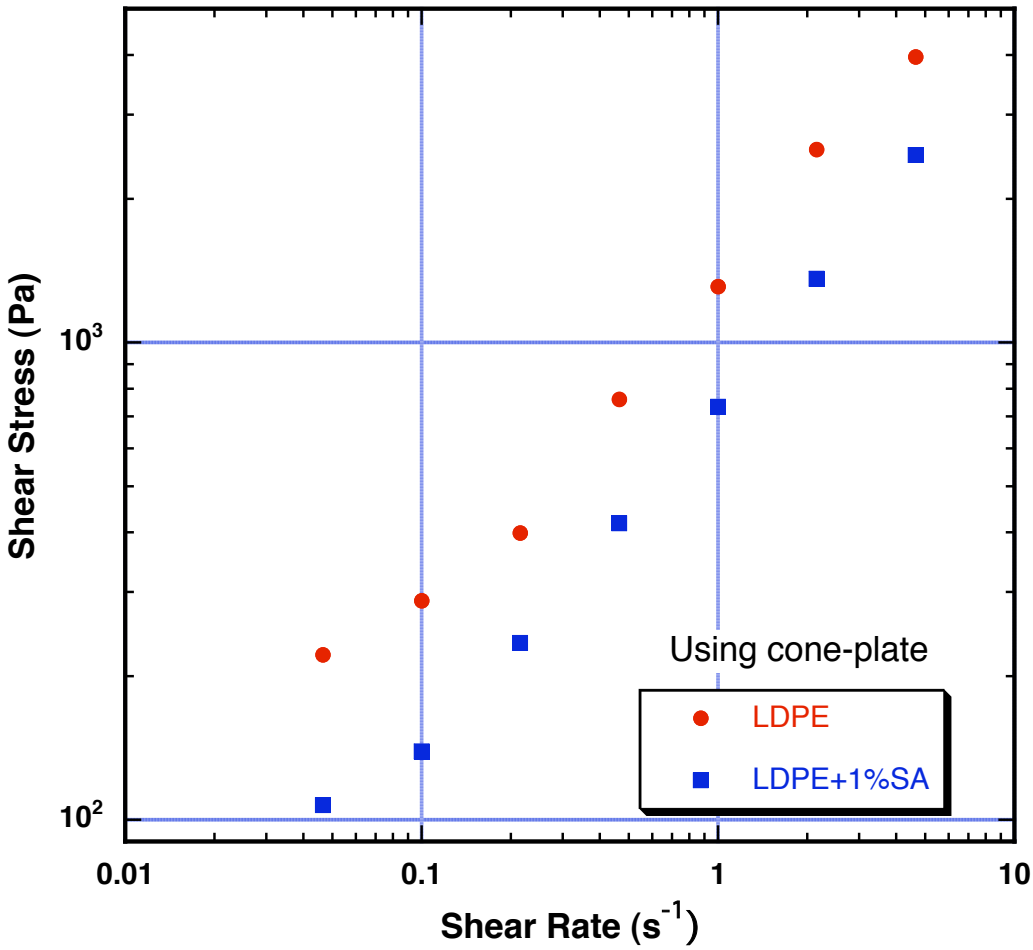

Figure 16: Effects of the stearic acid additive on the shear stress of LDPE in pure homogeneous shear flow using a cone-plate geometry and 220°C

5.1.2 Study of shear flow using ACER

We carried out steady shear-rate sweeps for polymers using six capillary dies of different diameters. The diameters of the capillary dies were 0.9, 1.0, 1.25, 1.5, 1.75, and 2.0 mm, respectively. The following experiments were all carried out using ACER at 220^{o}C.

Figure 17 shows the effect of the stearic acid additive on the shear viscosity of the LDPE at higher shear rates. The shear rate range used was $10s^{-1}$-$10000s^{-1}$. We have used the capillary die with 0.9 mm diameter. From the shear viscosity curves, we see that as we increase the value of shear rate, the reduction in shear viscosity due to the effect of additive decreases; at very high shear rates, the reduction due to the additive is less, almost 5%. As the shear rate increases, the samples shear thin and the viscosity drops dramatically. It seems reasonable, then, that at high shear rates the reduction in viscosity due to the additive would lessen.

We have grouped together all the shear rate sweeps for LDPE and for LDPE + 2% SA in the Figures 18 and 19, obtained with capillary dies of varying diameters. In the shear viscosity data of the neat LDPE, we observe some scatter in the data. The data for the LDPE + 2% SA samples shows lower values of shear viscosity than that of neat LDPE.

Figure 20 shows the effect of the stearic acid additive on the shear viscosity of HDPE using a capillary die of diameter 1.25 mm. The data shows similar trends as seen in the case of LDPE. The rate of reduction in shear viscosity values decreases as the shear rates increase, so that at very high shear rates the viscosity data points are

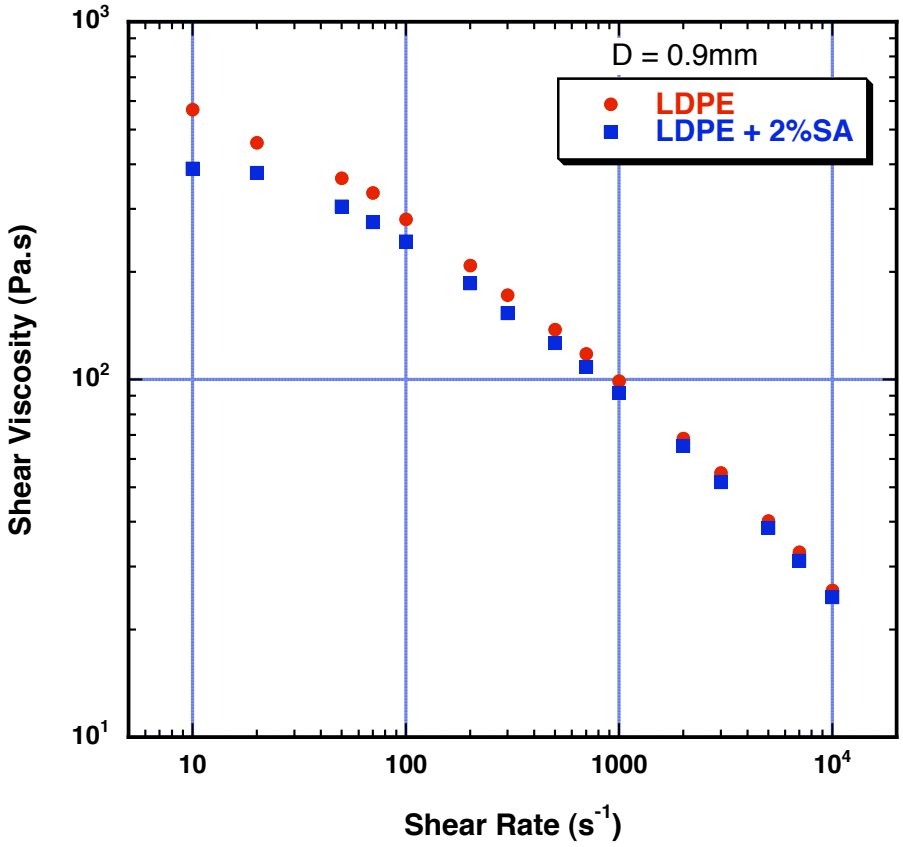

Figure 17: Effects of the stearic acid additive on the shear viscosity of LDPE in ACER using a capillary die of 0.9 mm at 220°C

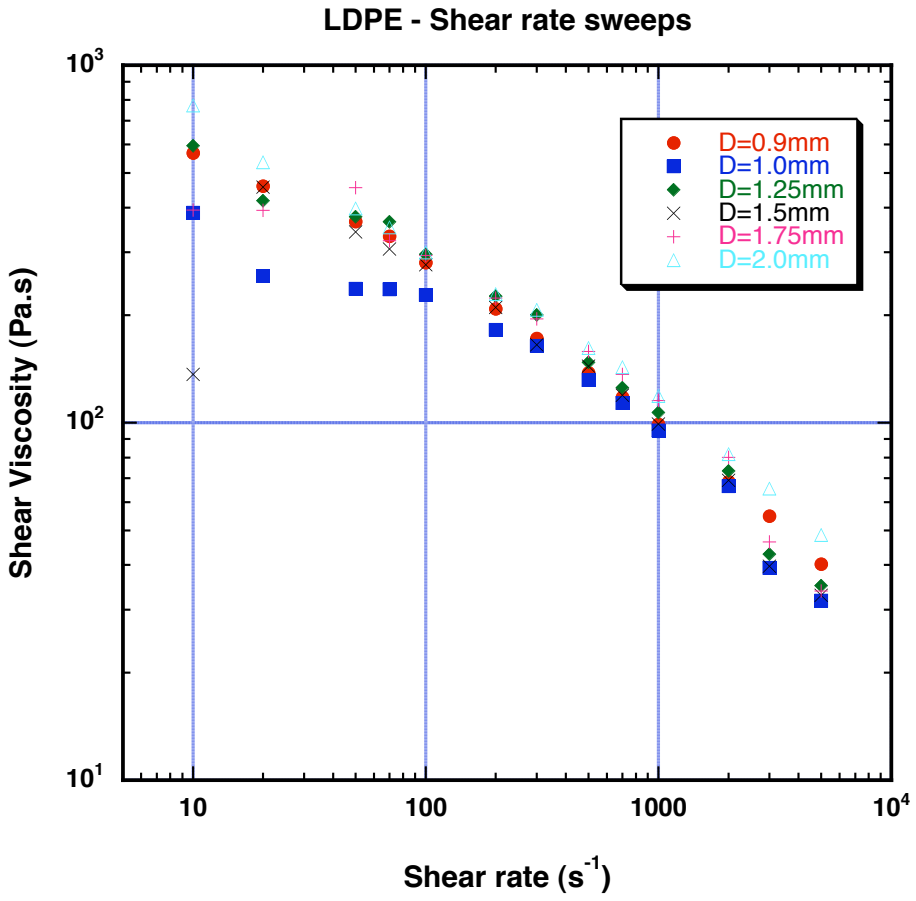

Figure 18: Shear viscosity data for LDPE in ACER using six capillary dies of different diameters at 220°C

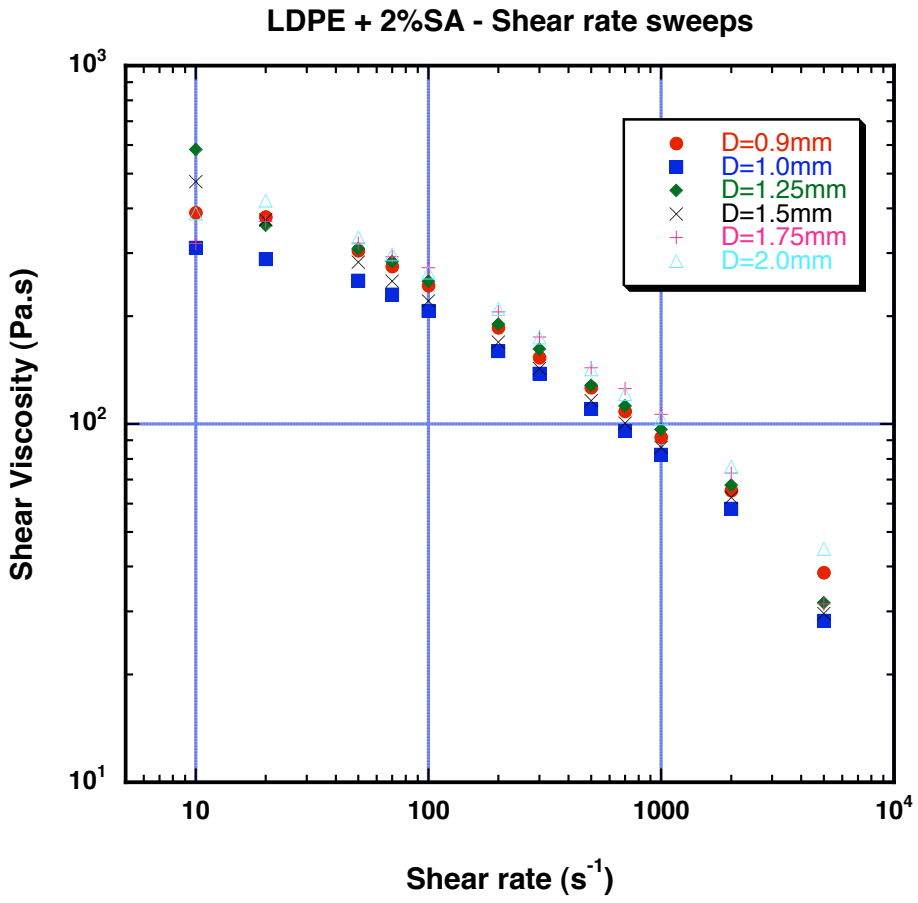

Figure 19: Shear viscosity data for LDPE + 2% stearic acid in ACER using six capillary dies of different diameters at 220°C

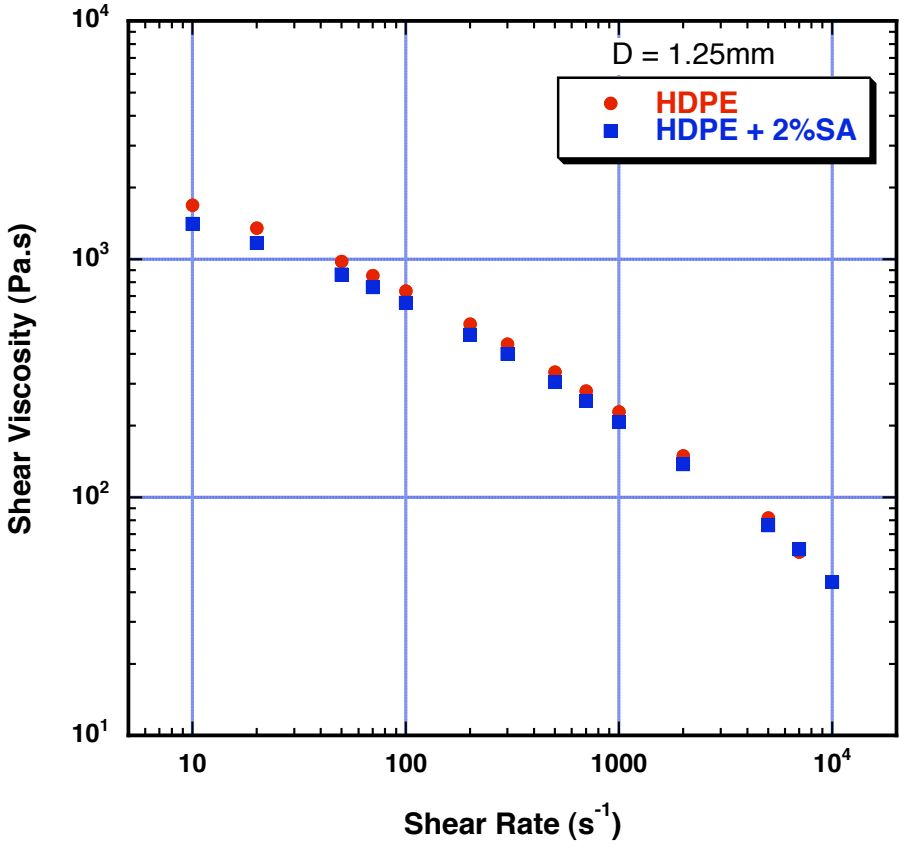

Figure 20: Effects of the stearic acid additive on the shear viscosity of HDPE in ACER using a capillary die of 1.25 mm at 220°C

overlapping. Figures 21 and 22 display the shear rate sweeps for HDPE and HDPE + 2% SA samples for six different capillary dies. In this case, the shear viscosity curves are close together and well defined. As the HDPE samples showed viscosity reduction of about 27% for the lowest shear rate in the experiments with the cone-plate geometry, the percentages of rate of reduction, which are about 15% at low shear rates in the capillary dies, are in accordance with the decreasing trend that was previously observed.

It has been suggested that the low viscosity carboxylic acids coat the walls of the die and essentially act as lubricants for the polymers, which introduces more slip at the walls. Hence, we study the effect of the stearic acid concentration by using increasing weight percentage of stearic acid in the neat polymer, we see that the largest decrease occurs with a very small amount of additive. With increasing percentage of additive, the reduction in the shear viscosity continues, however, it is not very pronounced. This can be explained by considering the surface area of the tube the capillary dies of constant radii. The additive coats the walls of the die; hence, as we increase the amount of additive, more and more additive coats the die walls until there is no more free area left to coat. Hence we see the maximum effect of the additive as we approach 5%, but the additive concentration does not really have a strong effect on the rate of reduction in the shear viscosity.

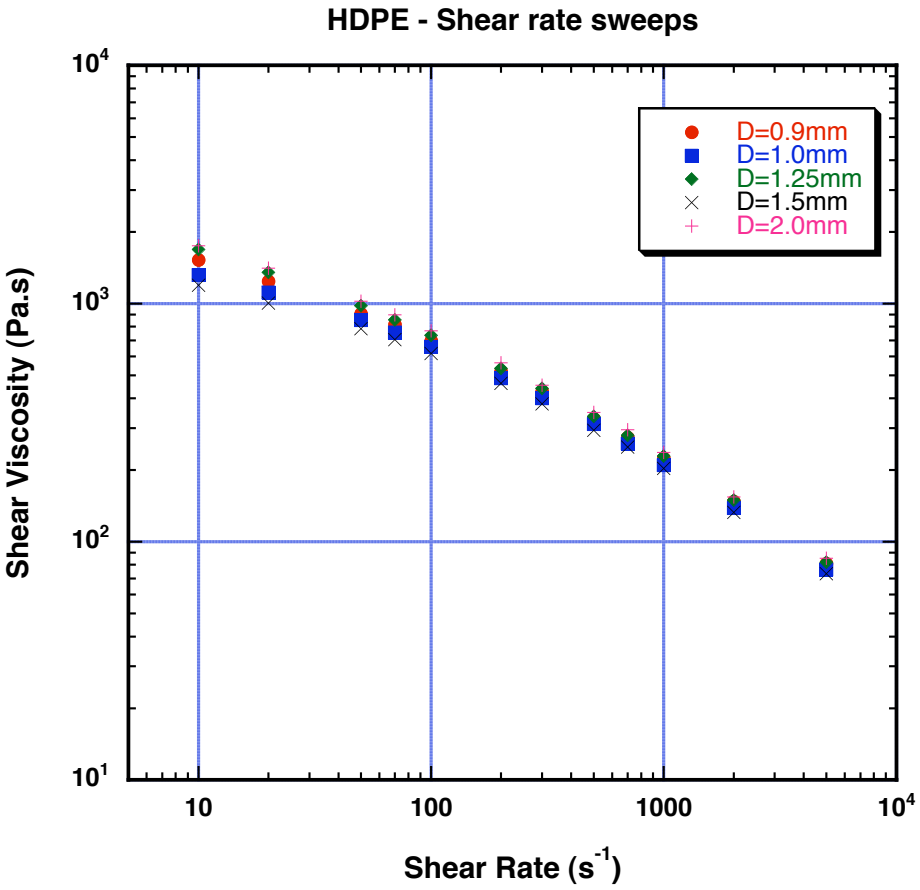

Figure 21: Shear viscosity data for HDPE in ACER using five capillary dies of different diameters at 220°C

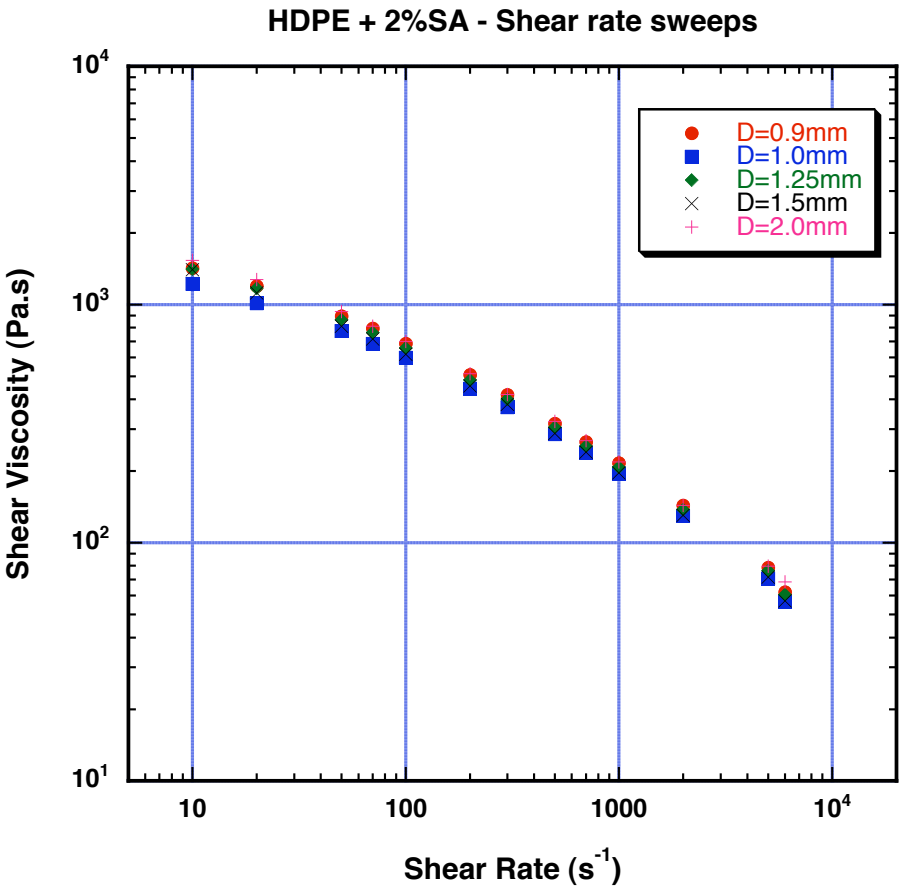

Figure 22: Shear viscosity data for HDPE + 2% stearic acid in ACER using five capillary dies of different diameters at 220°C

5.1.3 Slip velocities in shear flow

In this section, we show how Mooney's Analysis [27, 81] is used to calculate the slip velocities from the experimental data gathered for shear flow in the capillary rheometers. We calculate slip velocities in both the neat thermoplastics and the thermoplastics containing 2% additive (stearic acid).

5.1.3.1 Experiments

To follow the Mooney analysis, we need to have experimental flow rate measurements for a given sample at various constant shear stress values (at constant temperature) in capillaries of various diameters, as mentioned in Sec. 2.4.2. Hence we carry out shear stress sweeps for all the polymers using ACER and the six different diameter capillary dies mentioned previously. We used shear stress values of 0.01, 0.02, 0.03, 0.05, 0.07, 0.1, and 0.15 MPa. Here, we present some of the data for PP, LDPE, and HDPE from the shear stress sweep experiments.

In Figure 23, shear stress sweep results show that at a particular shear stress value the apparent shear rate measured for the polypropylene sample containing stearic acid is always higher than the neat polypropylene for the range of shear stress studied. We see that overall shear viscosity plots obtained from the shear stress sweeps are in agreement with the results obtained from the shear rate sweeps, as seen in the previous subsection. The shear viscosity plots show that the viscosity decreases due to the presence of the additive. Also, we can see that, as the measured shear rate values

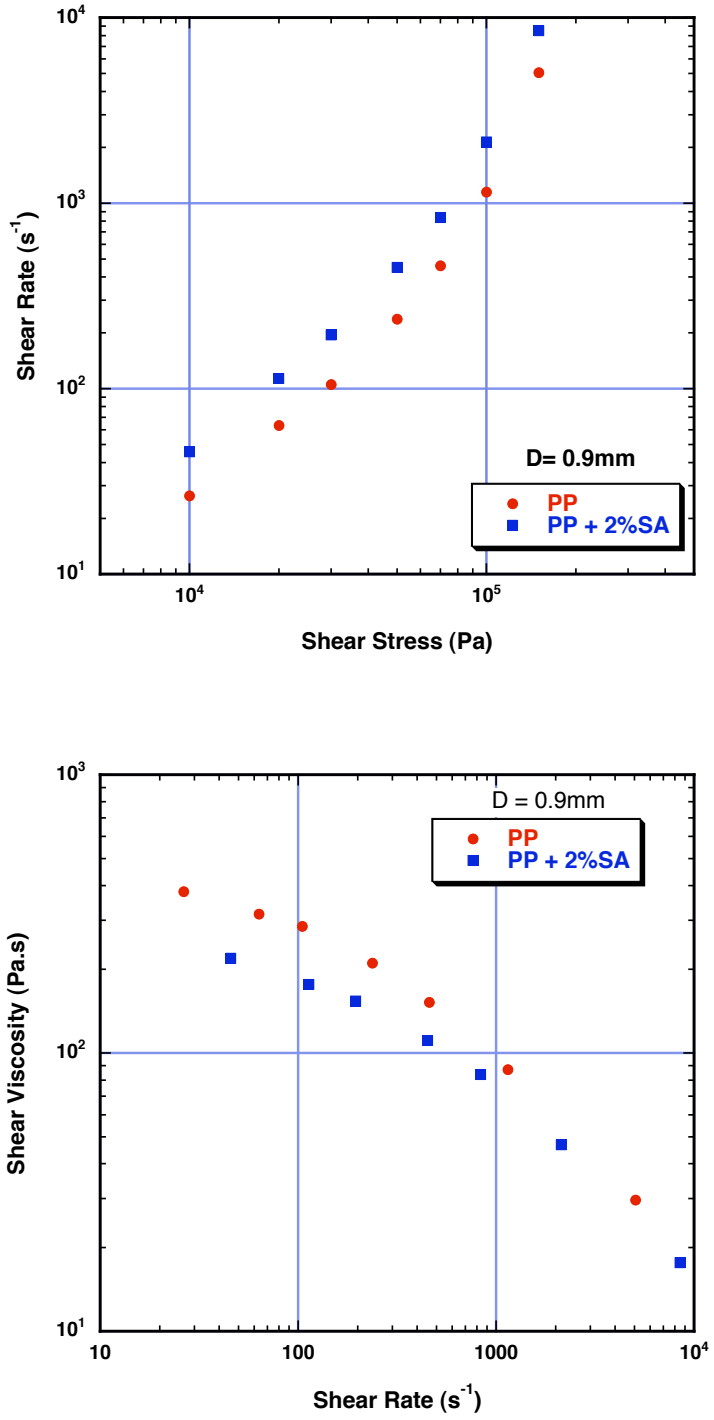

Figure 23: Shear stress sweep data for PP and PP + 2% stearic acid in ACER using a 0.9 mm capillary die at 220°C

increase due to the application of the higher stress, the reduction in the shear viscosity decreases.

When we look at figures 24 and 25, we see similar qualitative results in the cases of LDPE and HDPE as seen with PP. As the shear stress value applied to the sample increases, the apparent shear rate or flow rate increases. Consequently, we can deduce that the velocity inside the capillary tube increases. Also, for a constant stress value, the apparent shear rate for the polymer with additive is higher than that of the neat polymer. This implies that the slip velocity is greater due to the presence of the additive.

5.1.3.2 Analysis

In this section, we calculate the slip velocity values for the neat polymers as well as the polymers containing stearic acid. We need to plot $\frac{Q}{\pi a^3}$ vs. inverse of the radius of the capillary dies at constant shear stress values. The slope of this plot will give us a numerical value for the slip velocity for that particular sample. However, as we obtain the value of the apparent shear rate from the experiments shown in Sec. 5.1.3.1, and as apparent shear rate is given by $\frac{4Q}{\pi a^3}$, the value of the slip velocity will equal to the value of the slope divided by four.

Figures 26 and 27, demonstrate the slip velocity calculation by showing the plots of apparent shear rate vs. inverse radius of capillary dies at various constant shear stress values for polypropylene at 220^{o}C. From these plots, we can see that for

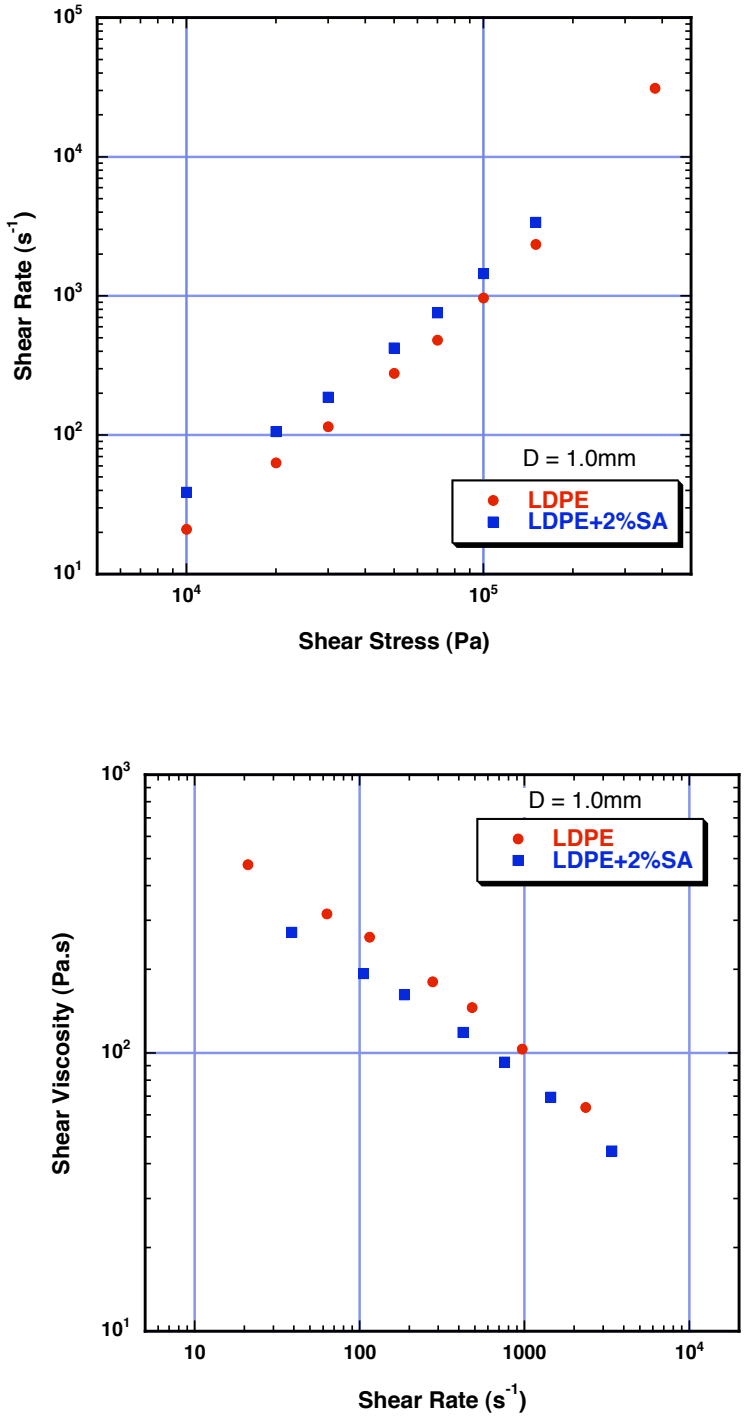

Figure 24: Shear stress sweep data for LDPE and LDPE + 2% stearic acid in ACER using a 1.0 mm capillary die at 220°C

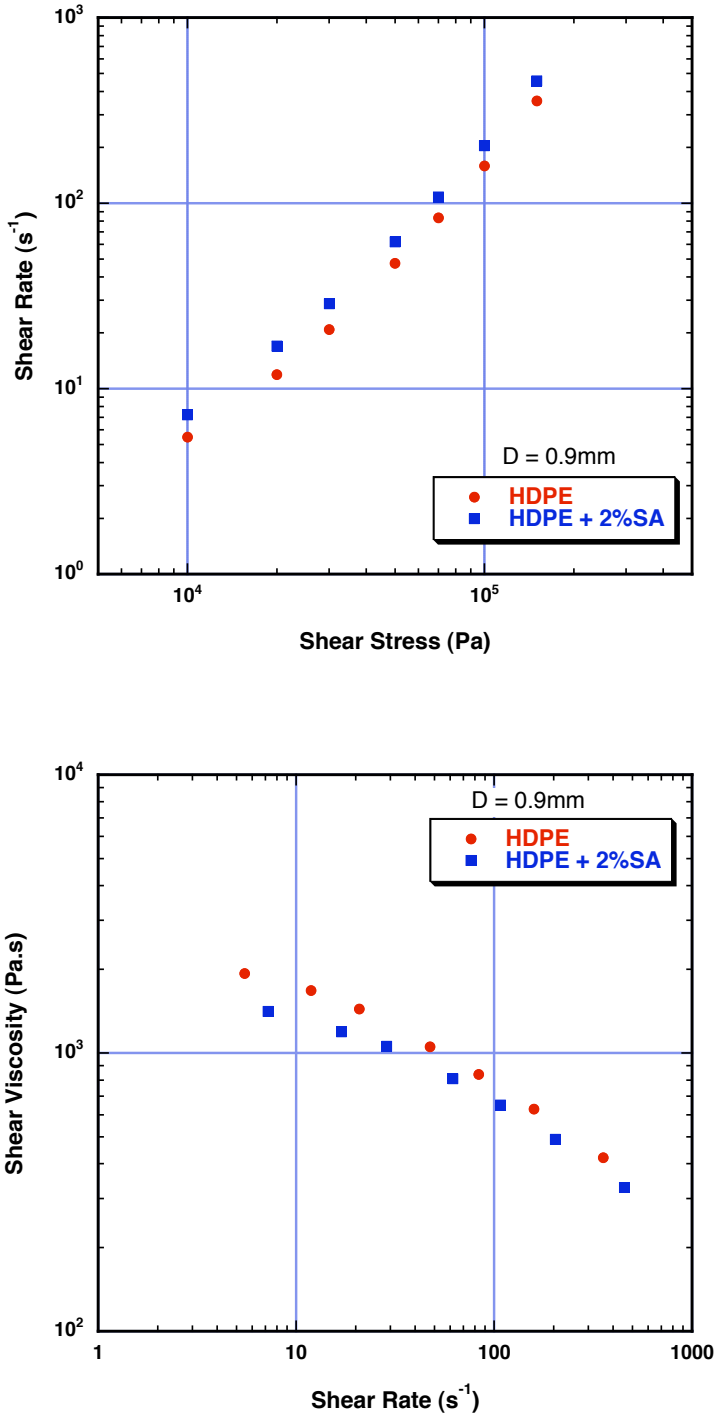

Figure 25: Shear stress sweep data for HDPE and HDPE + 2% stearic acid in ACER using a 0.9 mm capillary die at 220^{o}C

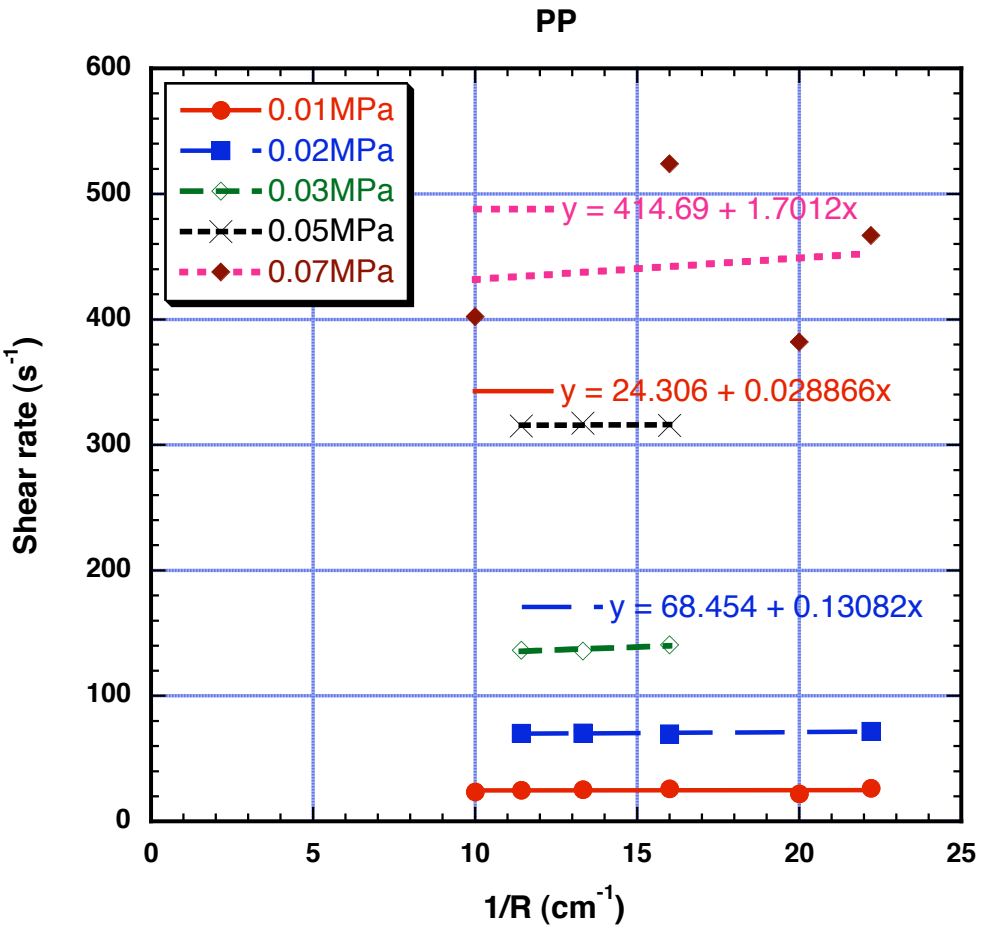

Figure 26: Plot of apparent shear rate vs. inverse radius of capillary die at various constant shear stress values for PP at 220°C

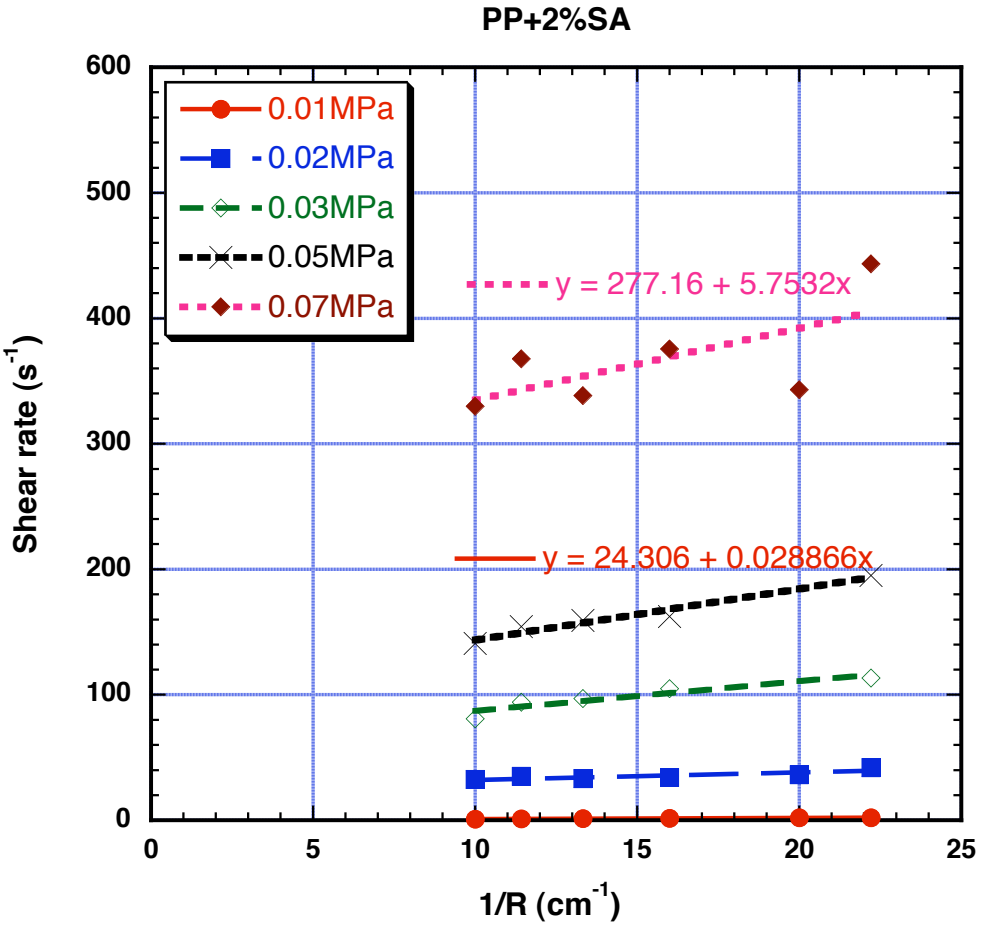

Figure 27: Plot of apparent shear rate vs. inverse radius of capillary die at various constant shear stress values for PP + 2% stearic acid at 220°C

neat PP, the slopes of the individual fits for various shear stress values are very close to zero. The values of the slopes increase as the shear stress increases, thus indicating a greater degree of slip is experienced by the neat polymer at higher shear stress values. When we look at Figure 27, the slopes are higher than that in case of the neat PP at the same constant shear stress values. The calculated slip velocities are plotted against the respective constant shear stress values in Figure 28 for both the neat polymer and corresponding sample containing the 2% Stearic acid. From this figure, we see that the neat thermoplastic experiences a finite amount of slip at the die walls, although this amount is very close to zero. In the case of PP samples containing stearic acid, the slip velocities are much higher than those observed in the neat PP. The slip velocities for PP plus additive increase nearly exponentially with increasing shear stress values.

Results for slip velocities of low-density polyethylene are reported in Figures 29, 30, and 31. Plots of apparent shear rate vs. inverse radius of capillary dies at various constant shear stress values for LDPE at 220^{o}C are presented in Figures 22 and 30. These show that the slopes for neat LDPE are higher than those seen for neat PP; however, they are still very small. When stearic acid is present in LDPE, then the corresponding slopes increase by a large quantity and the rate of increase in the slope is also dependent on the constant shear stress value, as seen in case of PP. The slip velocities in cm/s reported in Figure 31 are qualitatively very much similar to the ones reported for PP. The slip velocities for neat LDPE are very small and are more or less

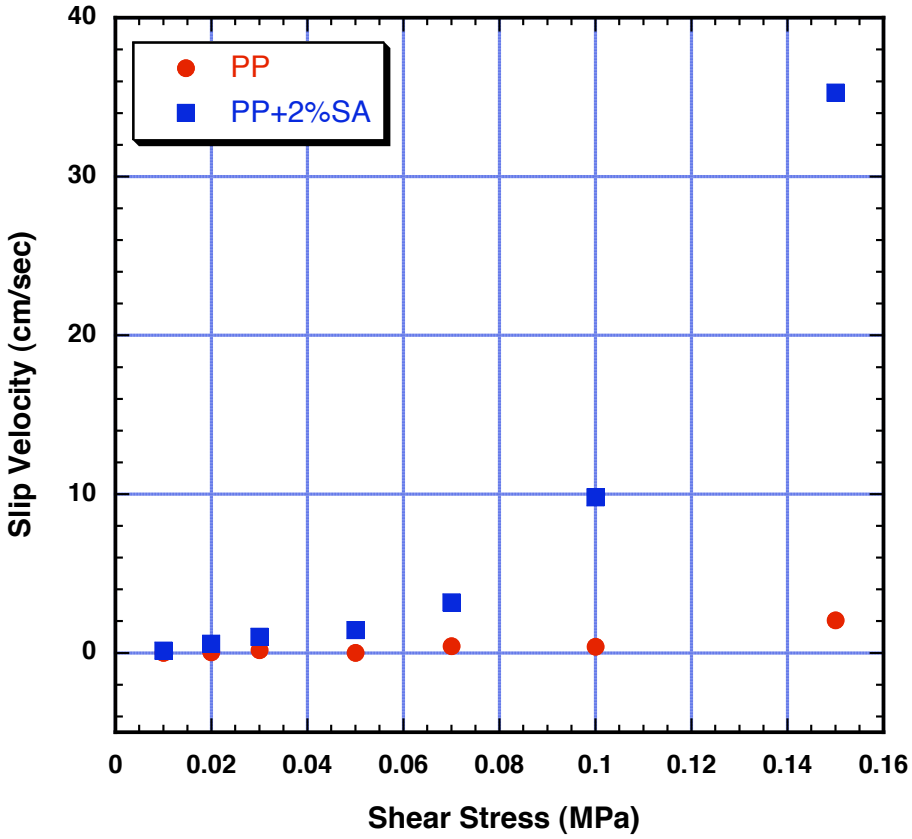

Figure 28: Plot of slip velocity vs. shear stress values for PP and PP + 2% stearic acid at 220°C in capillary dies

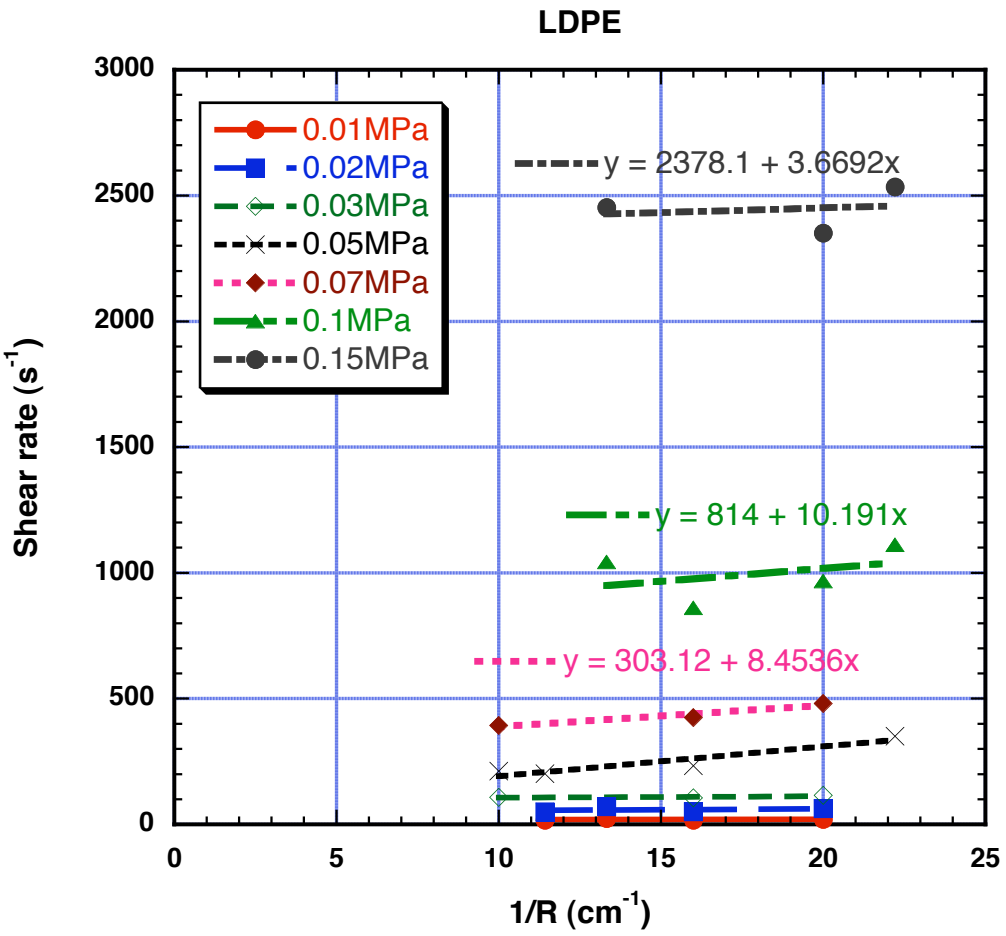

Figure 29: Plot of apparent shear rate vs. inverse radius of capillary die at various constant shear stress values for LDPE at 220°C

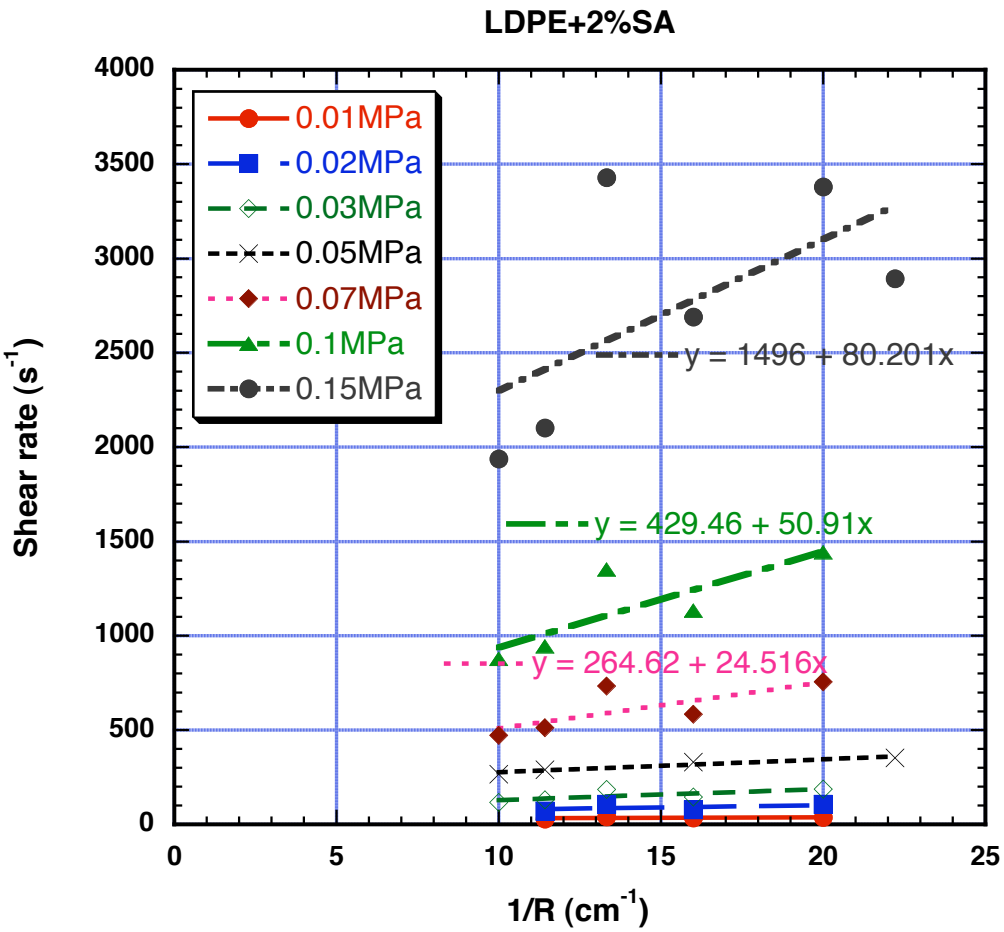

Figure 30: Plot of apparent shear rate vs. inverse radius of capillary die at various constant shear stress values for LDPE + 2% stearic acid at 220°C

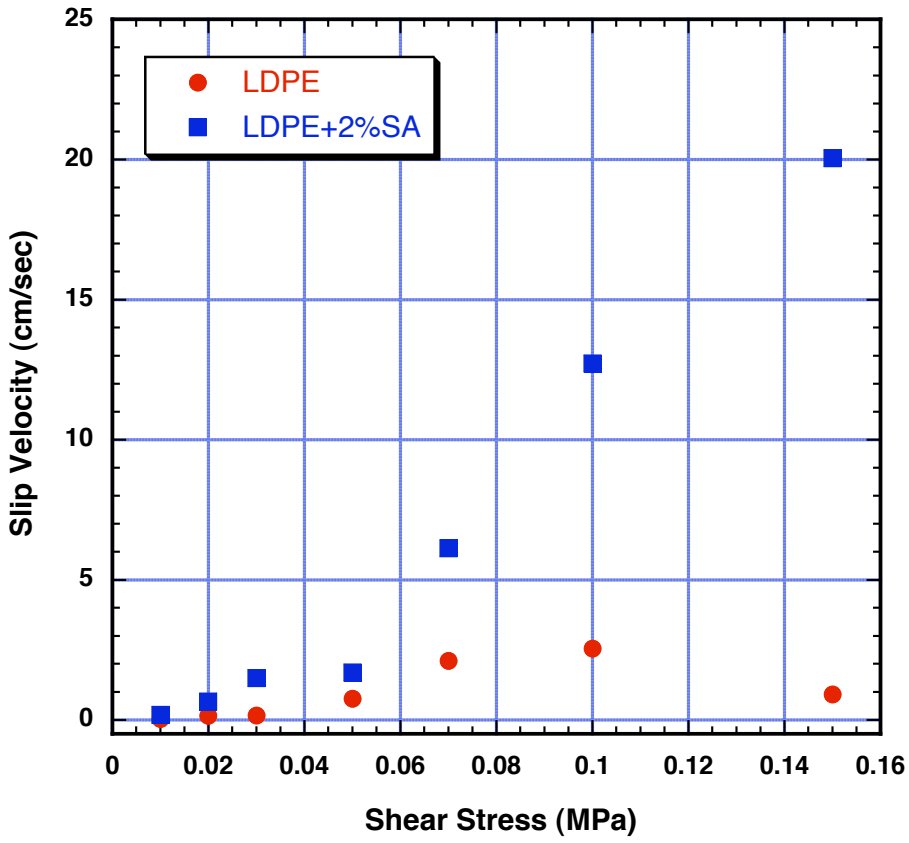

Figure 31: Plot of slip velocity vs. shear stress values for LDPE and LDPE + 2% stearic acid at 220°C in capillary dies

constant over the range of shear stresses studied; however, For LDPE+2% SA the slip velocities increase exponentially with increasing shear stress values.

We have obtained similar qualitative results in the case of high-density polyethylene, which can be seen in Figures 32, 33, and 34. Figures 32 and 33 present the plots of apparent shear rate vs. inverse radius of capillary dies at various constant shear stress values for LDPE at 220^{o}C. Figure 34 shows the slip velocities for both neat HDPE and HDPE plus stearic acid. Slip velocities for neat HDPE are close to zero initially at low constant shear stress values; however, they increase gradually with increasing shear stress. Slip velocities for HDPE plus 2% stearic acid increase exponentially with increasing shear stress; however, they show the lowest slip velocity values among the three polymers with the additive.

Tables 2–4 list the slip velocities for all three polymers and the corresponding samples with 2% stearic acid. There are two important points to be made regarding this data. First, the slip velocity increases dramatically with the imposed value of the shear stress. This indirectly implies that the slip velocity increases dramatically with increasing degree of molecular orientation of the polymer sample. Second, the additive has a huge effect on the slip velocity of the neat polymer. This implies that the neat polymer is probably not experiencing a large degree of slip in the capillary dies without the additive, except at the higher stress values.

The error in the calculated values of slip velocities can originate from the error in shear rate measurement when the experiments are carried out. In Tables 5 and 6, we report the percentage error in the shear rate measurement for the constant stress

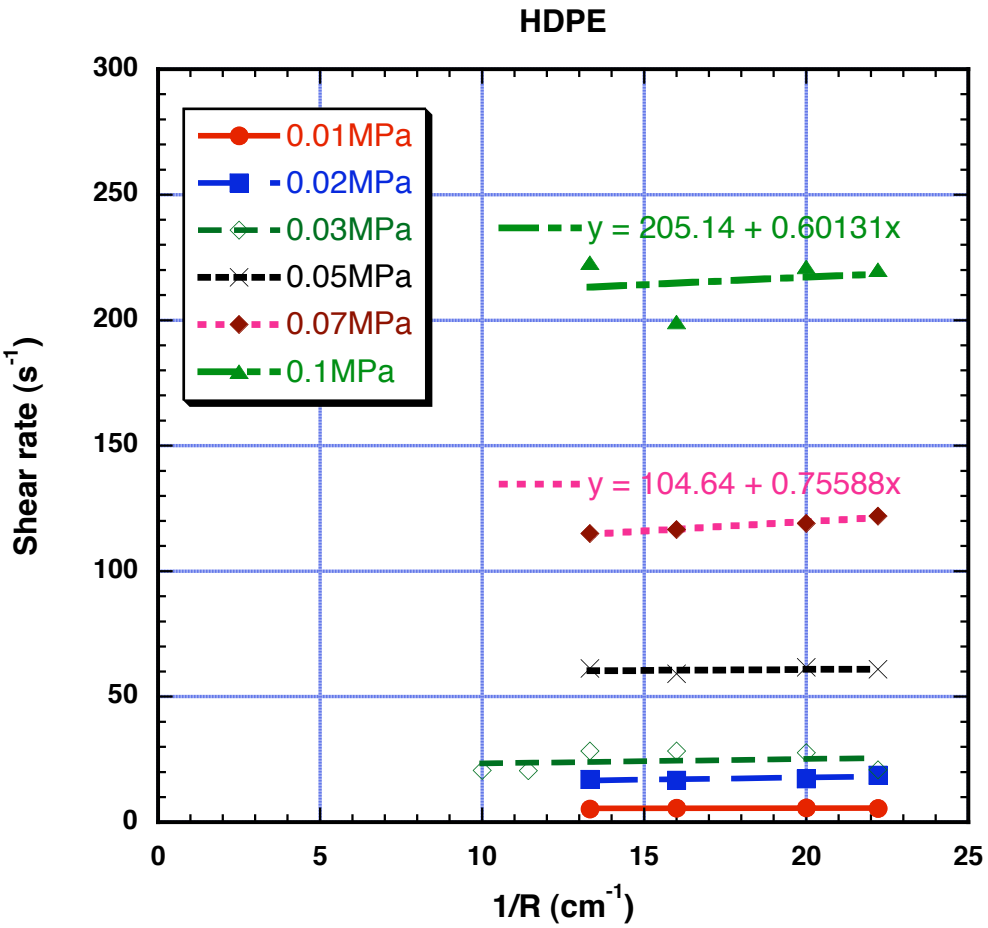

Figure 32: Plot of apparent shear rate vs. inverse radius of capillary die at various constant shear stress values for HDPE at 220°C

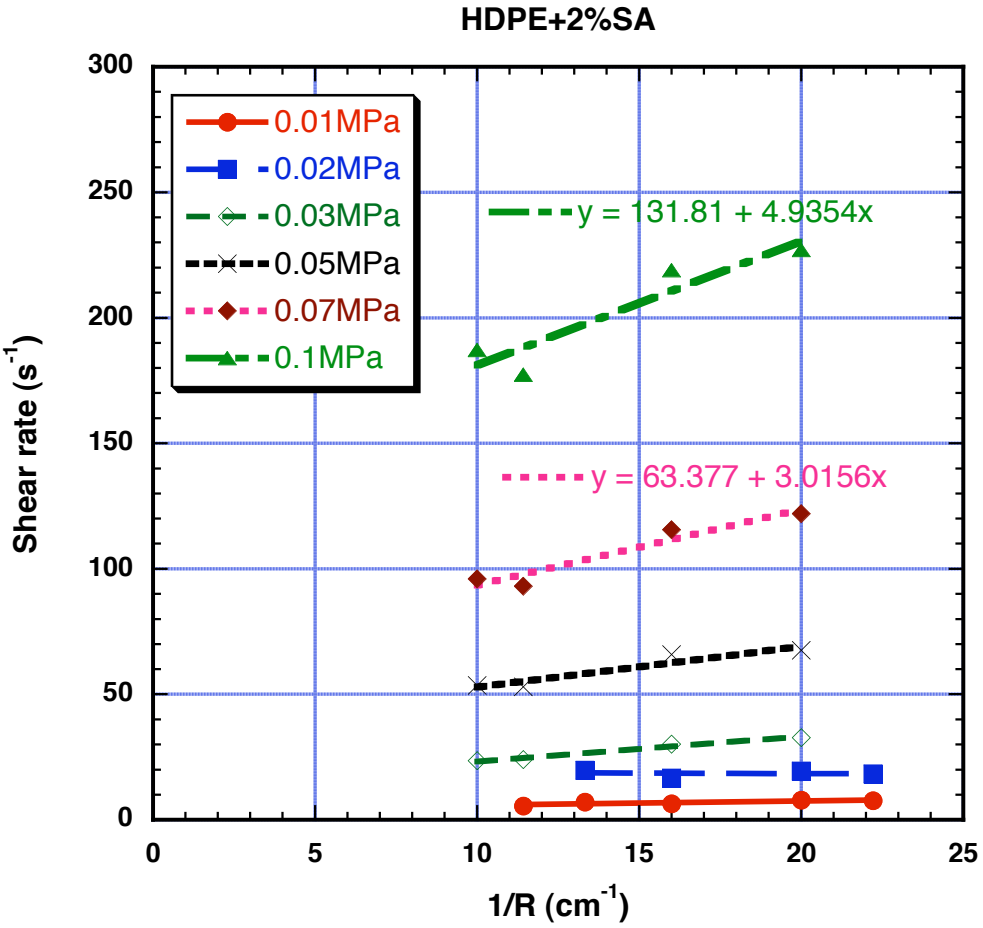

Figure 33: Plot of apparent shear rate vs. inverse radius of capillary die at various constant shear stress values for HDPE + 2% stearic acid at 220°C

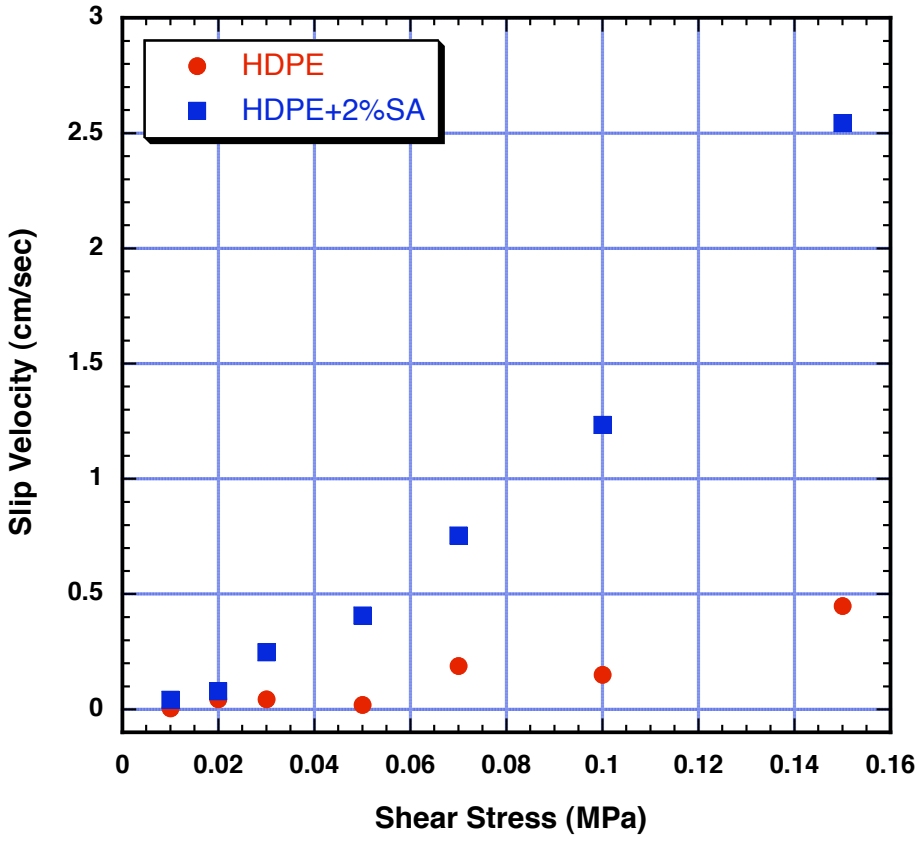

Figure 34: Plot of slip velocity vs. shear stress values for HDPE and HDPE + 2% stearic acid at 220^{o}C in capillary dies

Table 2: Slip velocities for PP and PP + 2% SA

Shear stress	Vs (PP)	Vs (PP + 2% SA)
MPa	**(cm/sec)**	**(cm/sec)**
0.01	0.0072	0.1494
0.02	0.0327	0.5899
0.03	0.1666	1.0160
0.05	0.0137	1.4383
0.07	0.4253	3.1833
0.1	0.4021	9.8048
0.15	2.0488	35.2750

Table 3: Slip velocities for LDPE and LDPE + 2% SA

Shear stress	Vs (LDPE)	Vs (LDPE + 2% SA)
MPa	(cm/sec)	(cm/sec)
0.01	0.0357	0.1777
0.02	0.1489	0.6564
0.03	0.1585	1.4869
0.05	0.7537	1.6928
0.07	2.1135	6.1290
0.1	2.5470	12.7200

Table 4: Slip velocities for HDPE and HDPE + 2% SA

Shear stress	Vs (HDPE)	Vs (HDPE + 2% SA)
MPa	**(cm/sec)**	**(cm/sec)**
0.01	0.0052	0.0420
0.02	0.0444	0.0788
0.03	0.0445	0.2476
0.05	0.0192	0.4067
0.07	0.1890	0.7539
0.1	0.1503	1.2339
0.15	0.4487	2.5438

Table 5: Percentage variation in the measurement of the shear rates for different constant shear stress values for PP

Capillary die diameter (mm)	Percentage variation in shear rate measurements (%)						
	0.01 (MPa)	**0.02 (MPa)**	**0.03 (MPa)**	**0.05 (MPa)**	**0.07 (MPa)**	**0.1 (MPa)**	**0.15 (MPa)**
0.9	8.065	3.856	1.906	1.784	2.529	1.009	1.553
1	3.589	4.091	3.980	3.982	3.950	2.969	0.989
1.25	-	1.190	9.017	1.189	8.191	6.983	5.058
1.75	-	1.065	6.138	15.370	7.135	4.771	2.198
2	3.171	1.804	0.678	0.893	1.584	0.494	0.436

Table 6: Percentage variation in the measurement of the shear rates for different constant shear stress values for PP + 2% SA

Capillary die diameter (mm)	Percentage variation in shear rate measurements (%)						
	0.01 (MPa)	**0.02 (MPa)**	**0.03 (MPa)**	**0.05 (MPa)**	**0.07 (MPa)**	**0.1 (MPa)**	**0.15 (MPa)**
1	3.589	4.091	3.980	3.982	3.950	2.969	0.989
1.5	-	1.190	9.017	1.189	8.191	6.983	5.058
2	3.171	1.804	0.678	0.893	1.584	0.494	0.436

experiments for neat polypropylene and PP+2%SA. It can be observed that the percentage error is higher at small values of constant shear stress, however as the shear stress values increase the percentage error becomes insignificant. When these error bars were included in the plots of apparent shear rate versus shear stress values for the particular polymers, they can only introduce a small change in the slopes of the curves corresponding to the lower constant shear stress values. At higher values of shear stress the error bars were not even visible outside the contours of the data symbols, hence we can safely say that errors could only be prevalent at lower shear stress values

5.2. Elongational Experiments

Using semi-hyperbolically converging dies of different Hencky values, elongational rate sweeps were performed on the three different polymers and the polymer samples containing the additive.

5.2.1 Study of elongational flow using semi-hyperbolically converging dies

Each polymer was tested with four different semi-hyperbolically converging dies having Hencky values of 4, 5, 6, and 7. Figures 35 and 36 show the effective elongational viscosity data for polypropylene, PP + 1% stearic acid, and PP + 2% stearic acid. From these plots, we can see that the reduction in the effective elongational viscosity values is highest for H4 and it decreases as we move to higher Hencky strain dies. In the case of PP, reductions of up to 20% are observed with lower Hencky dies, whereas for higher Hencky dies reduction is limited to up to 7%. As in

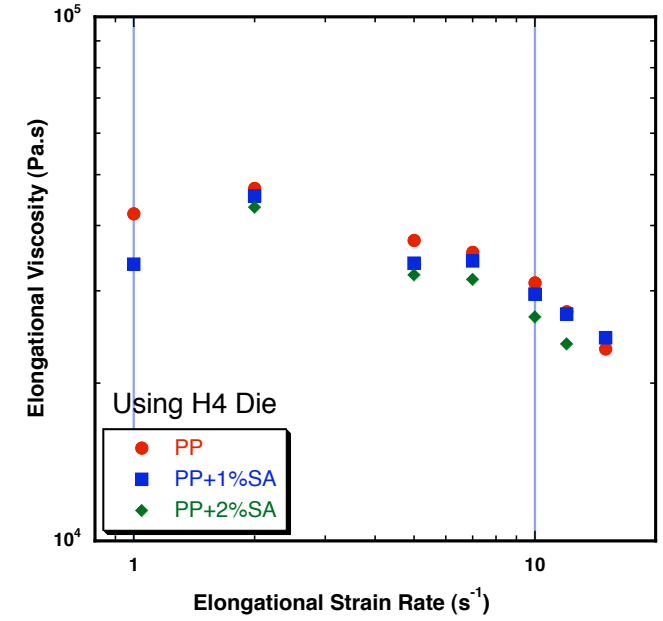

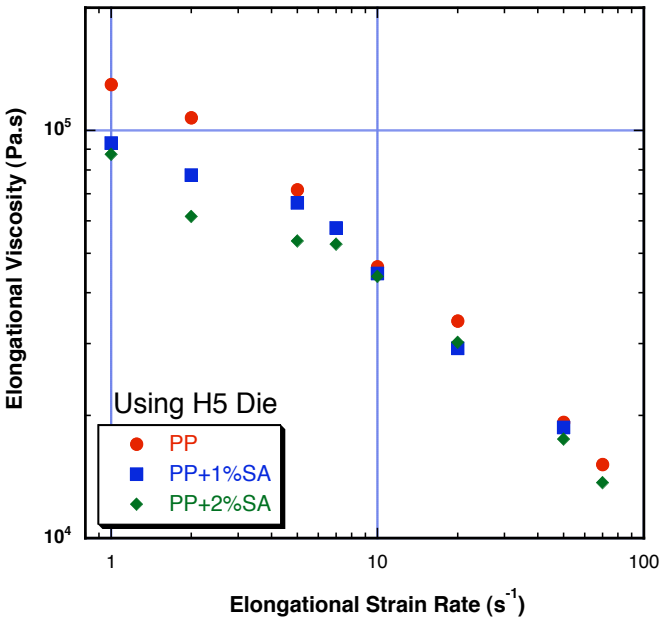

Figure 35: Effective elongational viscosity data for PP, PP + 1% stearic acid, PP + 2% stearic acid obtained using Hencky 4 and 5 dies in ACER at 220°C

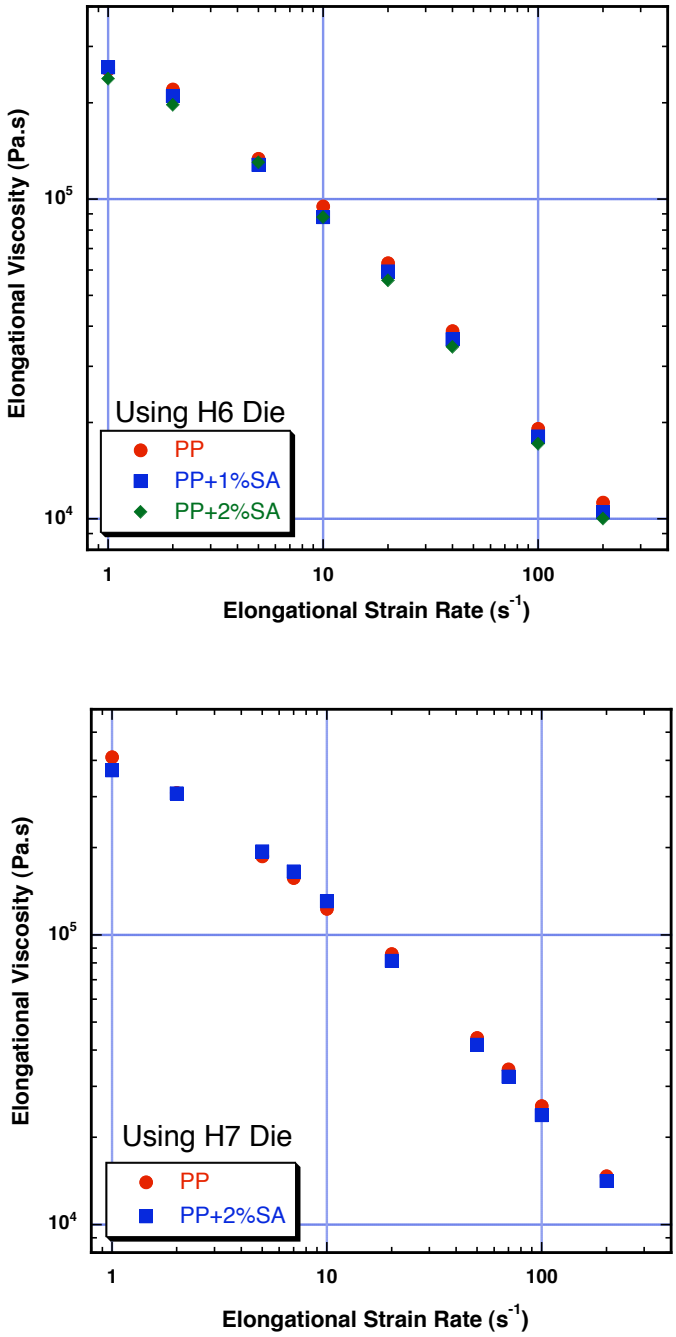

Figure 36: Effective elongational viscosity data for PP, PP + 1% stearic acid, PP + 2% stearic acid obtained using Hencky 6 and 7 dies in ACER at 220°C

case of the capillary dies, it was observed that the amount of additive does not have a large effect on the rate of viscosity reduction, as seen in plots of Figure 36. From the plots for H4 and H5 at low strain rates, one can see that there is scatter in the data and inconsistent trends are observed. This can be explained by the fact that for H4 and H5 dies, the exit diameters are larger as compared to the capillary dies of the higher Hencky strain dies, and hence enhanced gravitational effects are experienced by the polymer melt in these dies and the flow can be rendered unstable. During experimentation, it was observed that the polymer melt would fall under gravity from these dies even at the initial rest state where no force was being applied by the ram in ACER. However, at higher Hencky strains and higher strain rates, the effective elongational viscosity data obtained from the semi-hyperbolically converging dies is well defined and free of the scatter.

Similar experiments were performed with LDPE and LDPE +2% stearic acid and the results are plotted in Figures 37 and 38. In this case, reductions in elongational viscosity of about 25% are observed in dies having lower Hencky values, whereas only up to 10% reductions are seen at higher Hencky values. For LDPE, there is high rate of reduction in the effective elongational viscosity from the neat polymer to the polymer containing the additive, which leads us to believe that this particular polymer experiences less amount of slip in the semi-hyperbolically converging dies than the other two. Therefore, when the additive is present, it has a greater lubricating effect on the sample.

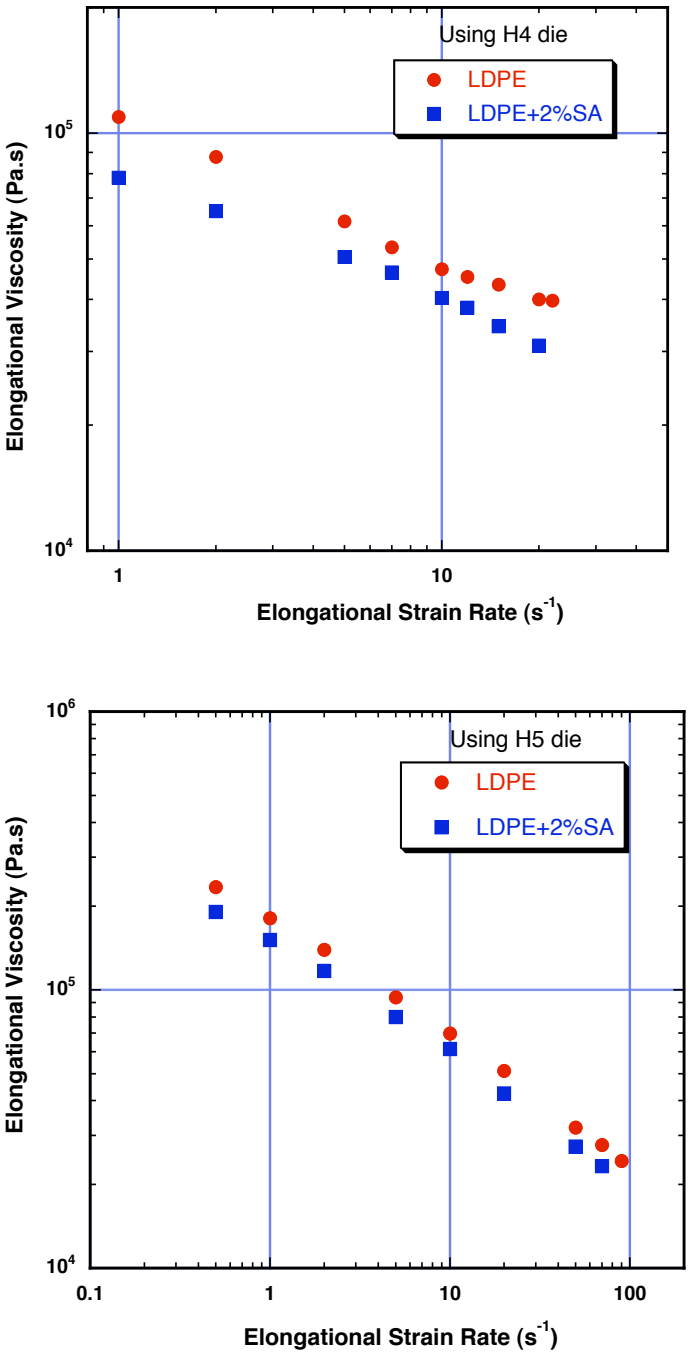

Figure 37: Effective elongational viscosity data for LDPE and LDPE + 2% stearic acid obtained using Hencky 4 and 5 dies in ACER at 220°C

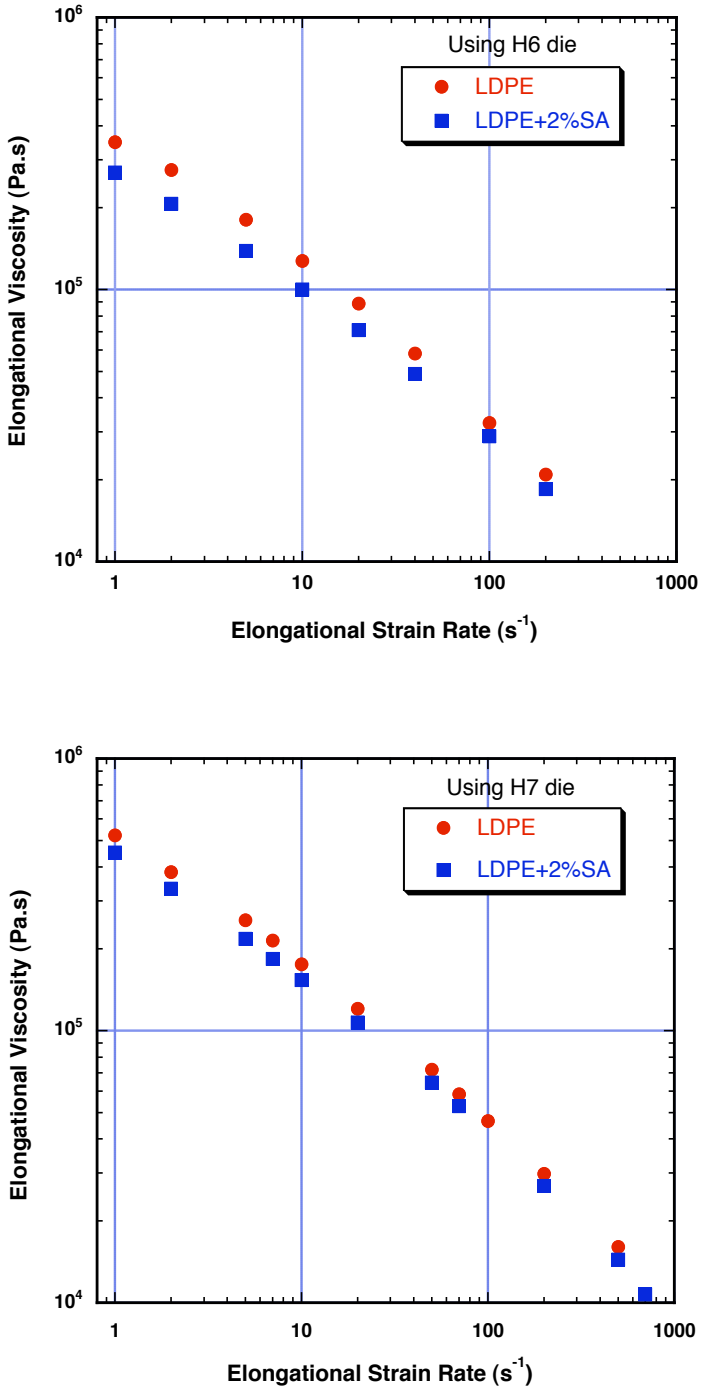

Figure 38: Effective elongational viscosity data for LDPE and LDPE + 2% stearic acid obtained using Hencky 6 and 7 dies in ACER at 220°C

High-density polyethylene provided us with very well-defined data in the semi-hyperbolically converging dies, as seen in Figures 39, 40. Moreover, effective elongational viscosity reductions of only about 9% are observed with lower Hencky strain dies, and at higher Hencky strains reductions less than 4% were recorded. As HDPE samples showed very small reductions amongst all the three polymers studied, it leads us to believe that this polymer experiences the highest slip in the semi-hyperbolically converging dies.

5.2.2 Slip velocities in the semi-hyperbolically converging dies

To calculate slip velocities in the semi-hyperbolically converging dies, we use the modified Mooney equation derived for these dies in Sec. 3.4. The slip velocity is given by the Eq. (I.41) as

$$\left.\frac{\partial\left(\frac{Q}{\pi R^3}-\frac{\dot{\varepsilon} z}{R}\right)}{\partial\left(\frac{1}{R}\right)}\right|_{z,s} = s\beta = v_{slip} \tag{I.41}$$

From this expression, we can see that we need the data at constant elongational stress values. Hence, we calculate $\frac{Q}{\pi R^3}-\frac{\dot{\varepsilon} z}{R}$ at various constant elongational stress values and at $z = 25\,\text{mm}$, which is the exit of the die (where the pressure is known). We know Q and $\dot{\varepsilon}$ from the experimental data. We then plot $\frac{Q}{\pi R^3}-\frac{\dot{\varepsilon} z}{R}$ vs. $\frac{1}{R}$, and calculate the

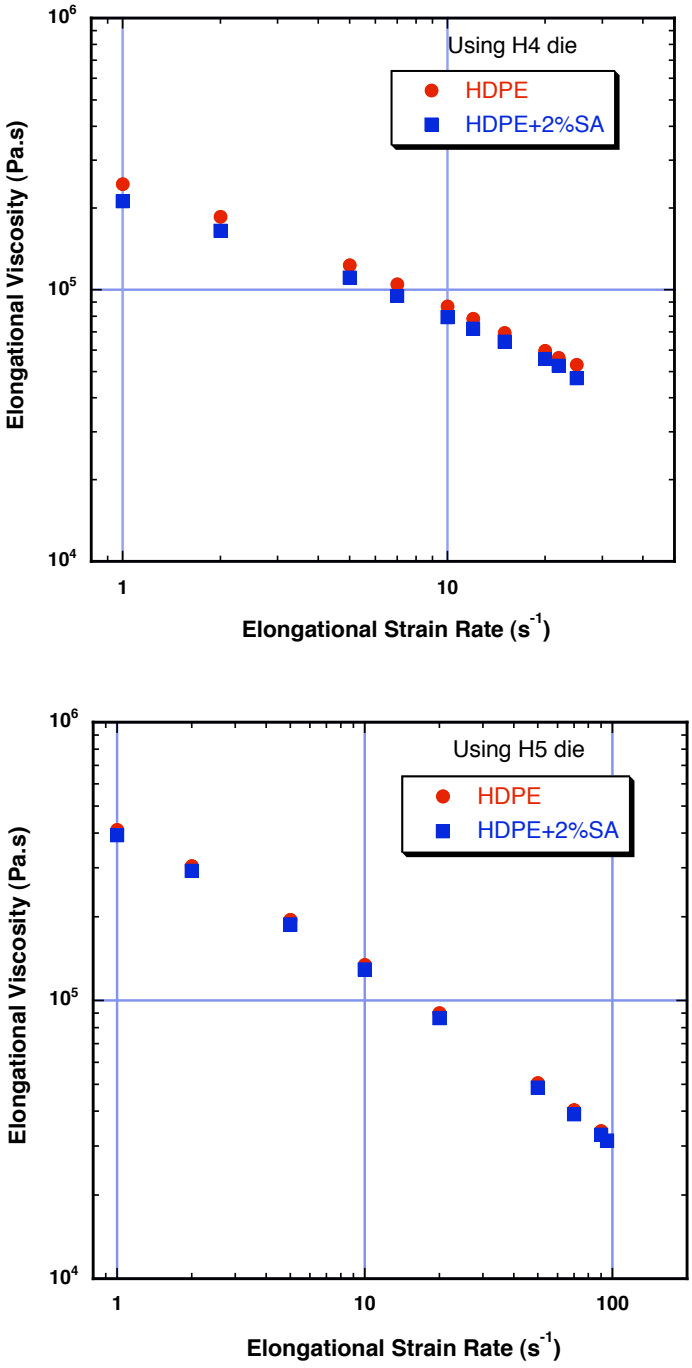

Figure 39: Effective elongational viscosity data for HDPE and HDPE + 2% stearic acid obtained using Hencky 4 and 5 dies in ACER at 220°C

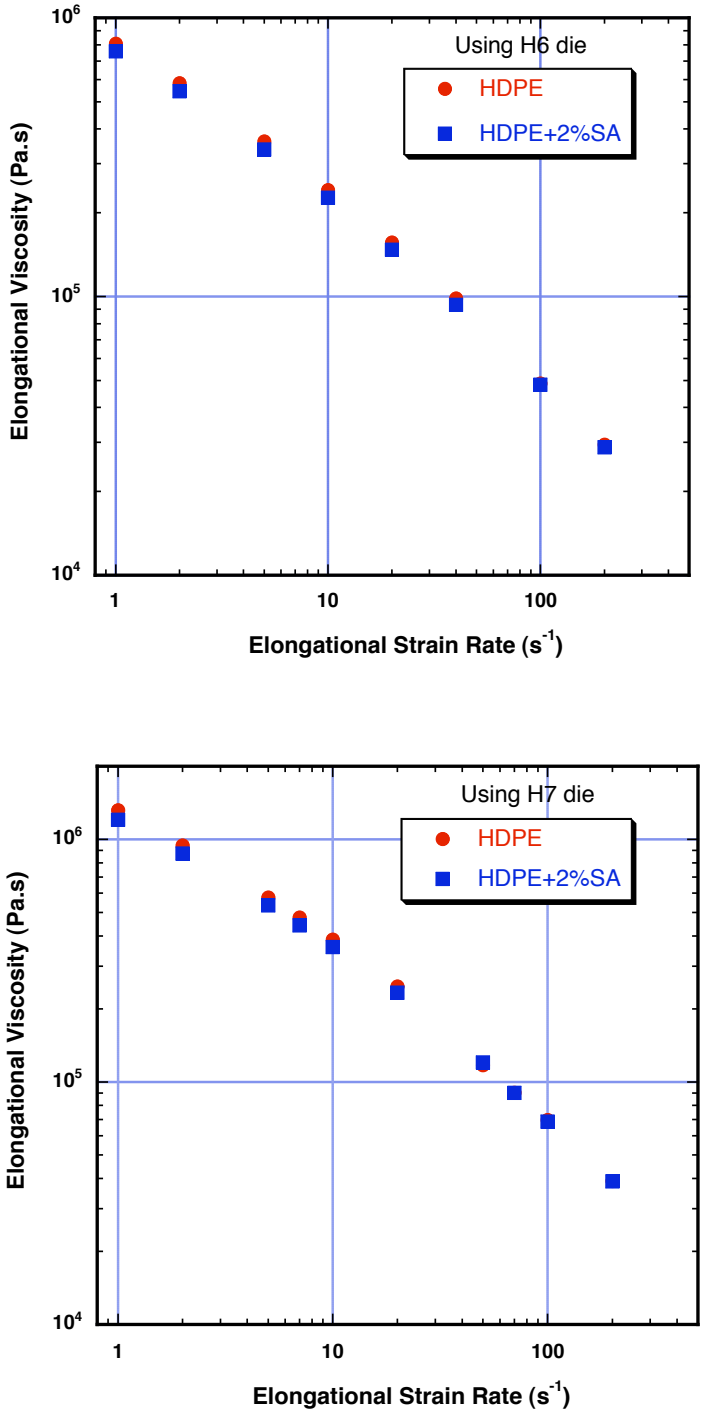

Figure 40: Effective elongational viscosity data for HDPE and HDPE + 2% stearic acid obtained using Hencky 6 and 7 dies in ACER at 220°C

slope, which gives the slip velocity in the semi-hyperbolically converging die.

Figures 41 - 42 show plots for HDPE, HDPE + 2% SA. Here we see that, unlike the plots for capillary dies where the slopes change drastically from the neat polymer to the polymer sample with additive, the plots for both HDPE and HDPE + 2% SA show slopes that are very similar. The slip velocities were calculated, and Figure 43 shows slip velocities for HDPE and HDPE + 2% SA at 220^{o}C. In this plot, the slip velocities increase almost linearly with increasing elongational stress values.

Similarly Figures 44 - 45 show plots of the calculation of slip velocities in the SHCD for PP, PP + 2% SA. Here we observe that the slopes are still very similar to each other when compared with the shear data however the values of the slip velocities for the neat PP and PP+2%SA given in Figure 46 are father apart than in case of HDPE.

Thus, not only the values of slip velocities increase almost linearly with increasing elongational stress values but the slip velocities for neat polymer and polymer with additive also are not much different. Thus the additive does not have a large effect on the viscosity of the neat polymer. This suggests that even the neat polymer is experiencing a large degree of slip in the semi-hyperbolically converging dies. Given the fact that these dies impose strong extensional characteristics to the flow field, this is to be expected: the extensional flow orients the polymer chains much more strongly than shear flow, thus leading to a greater degree of slip at the wall.

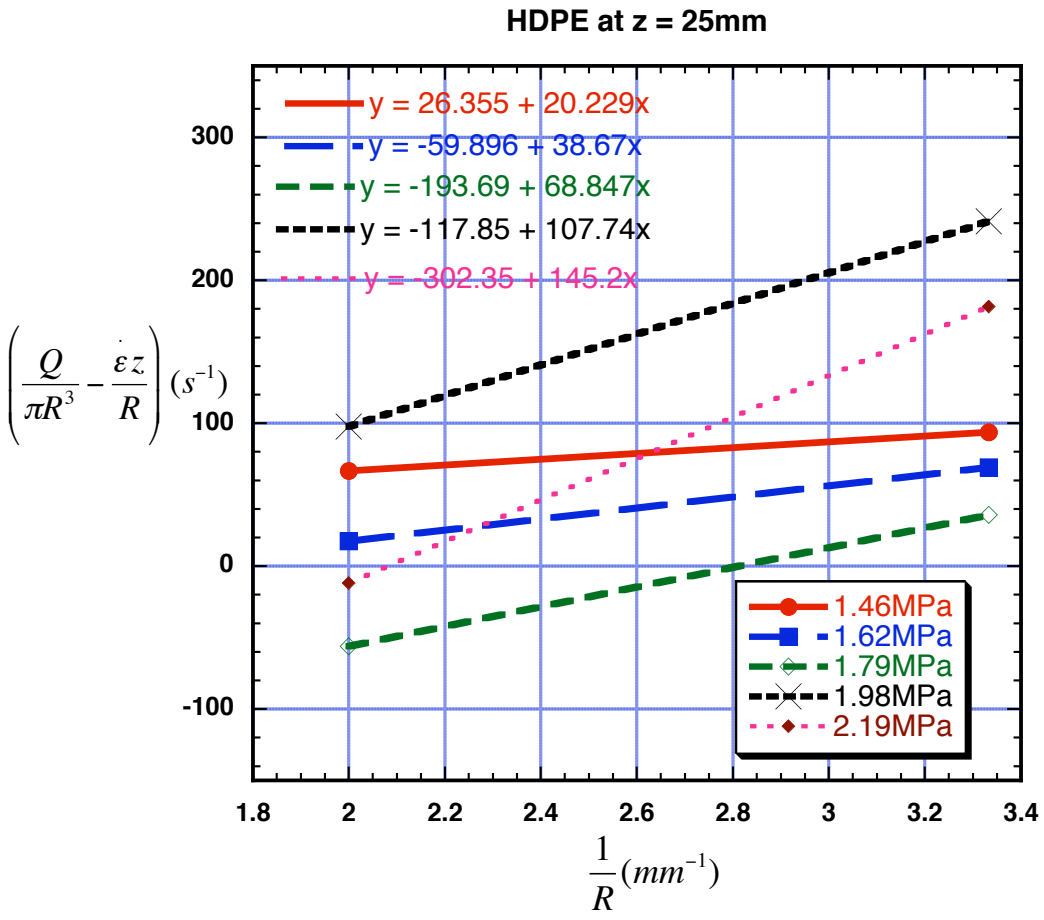

Figure 41: Plot of $\frac{Q}{\pi R^3}-\frac{\dot{\varepsilon} z}{R}$ vs. $\frac{1}{R}$ in semi-hyperbolically converging dies at various constant elongational stress values for HDPE at 220°C at $z=25\,\text{mm}$

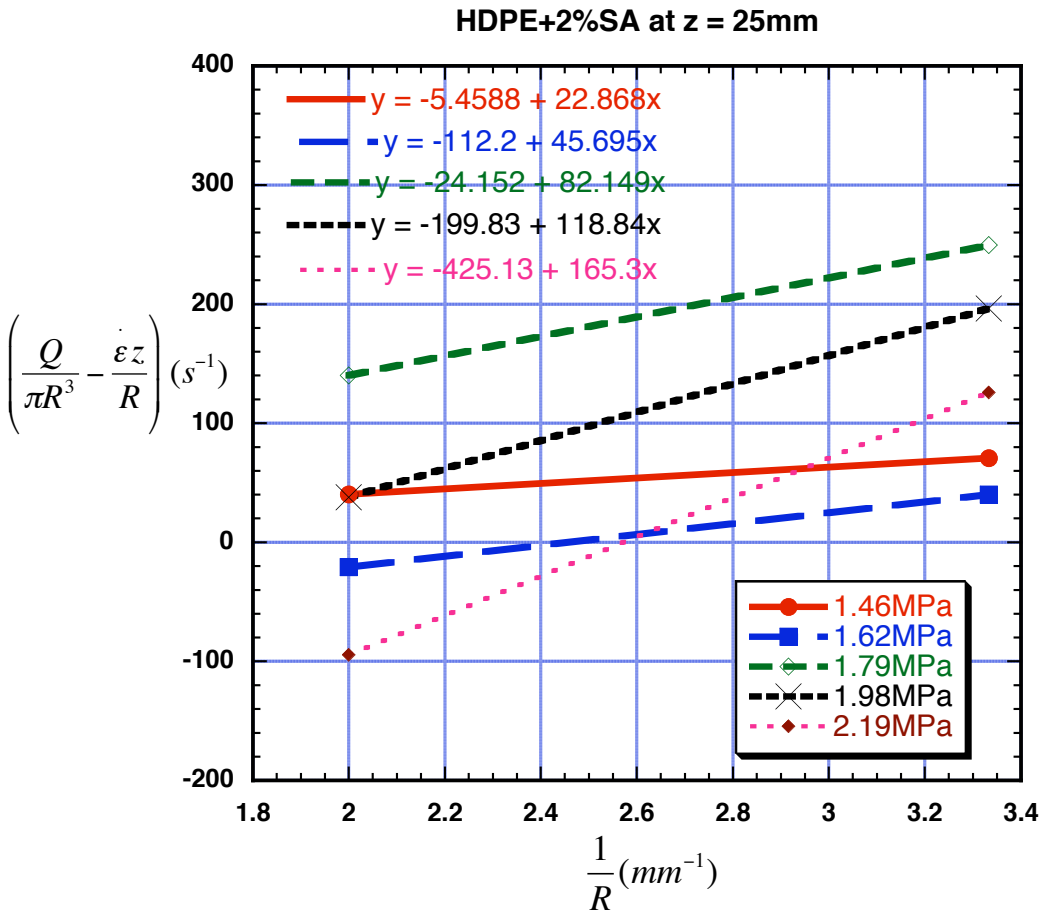

Figure 42: Plot of $\frac{Q}{\pi R^3}-\frac{\dot{\varepsilon} z}{R}$ vs. $\frac{1}{R}$ in semi-hyperbolically converging dies at various constant elongational stress values for HDPE +2% stearic acid at 220°C at $z = 25\,\text{mm}$

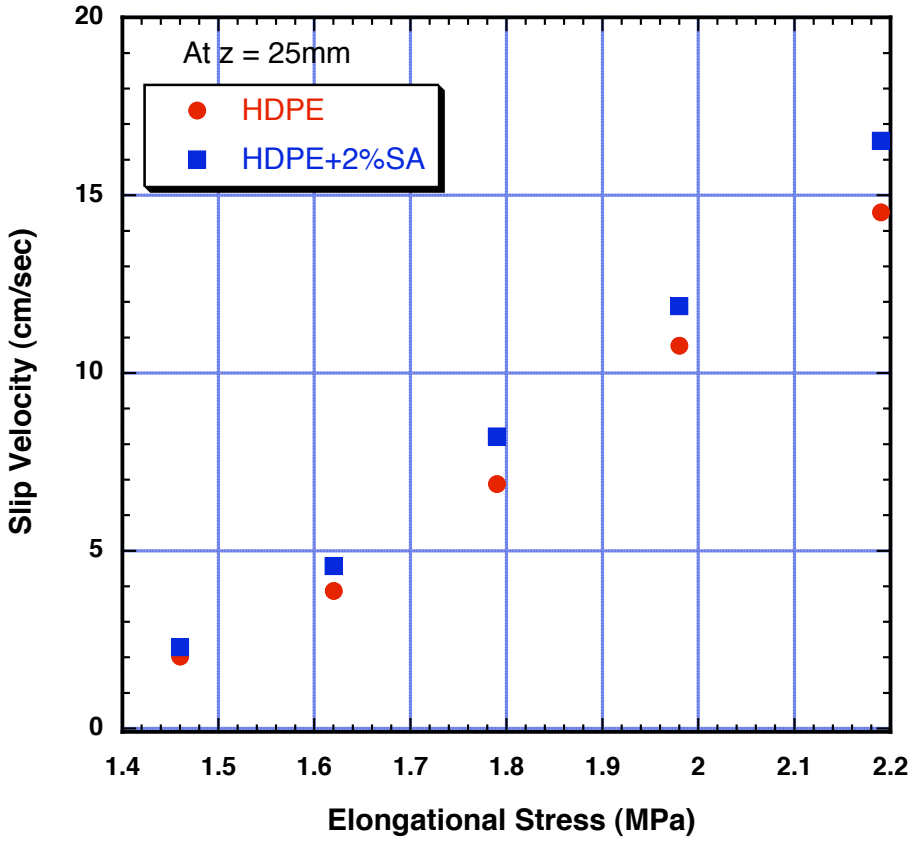

Figure 43: Plot of slip velocity vs. elongational stress values for HDPE and HDPE + 2% stearic acid at 220^{o}C in semi-hyperbolically converging dies

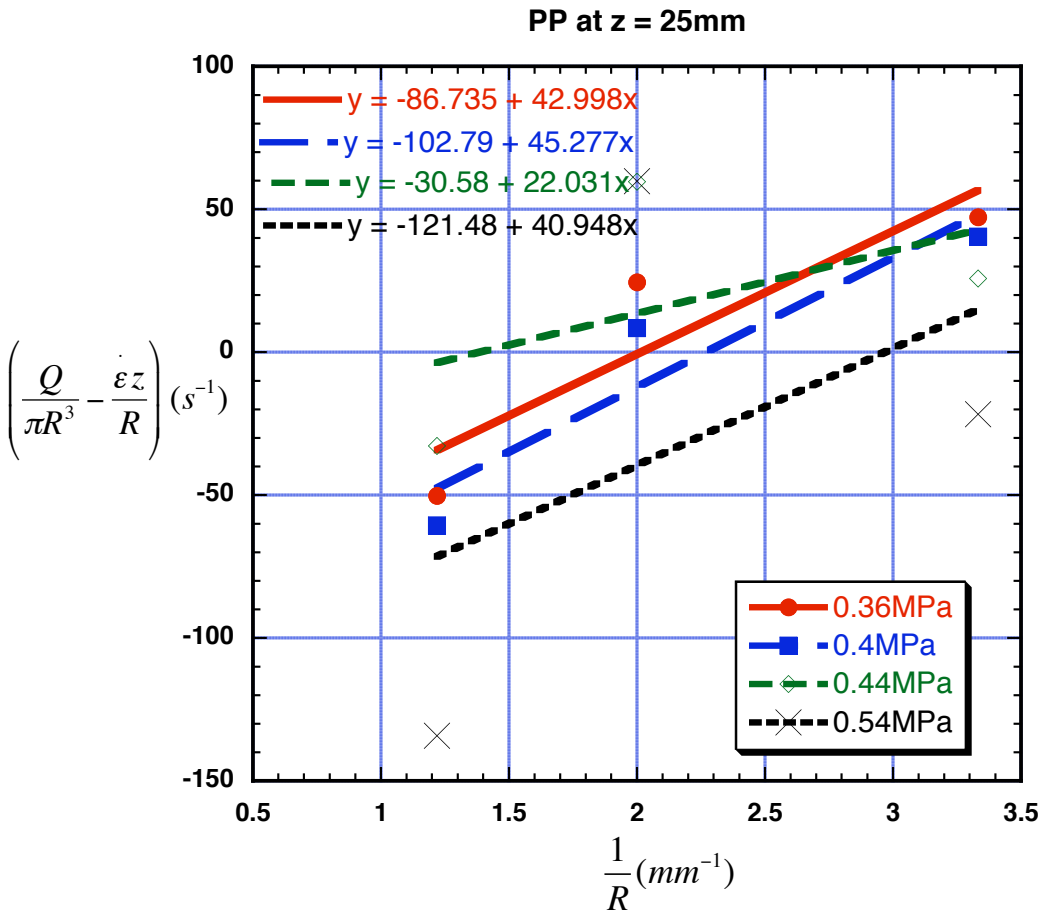

Figure 44: Plot of $\frac{Q}{\pi R^3}-\frac{\dot{\varepsilon} z}{R}$ vs. $\frac{1}{R}$ in semi-hyperbolically converging dies at various constant elongational stress values for PP at 220°C at $z = 25\,\text{mm}$

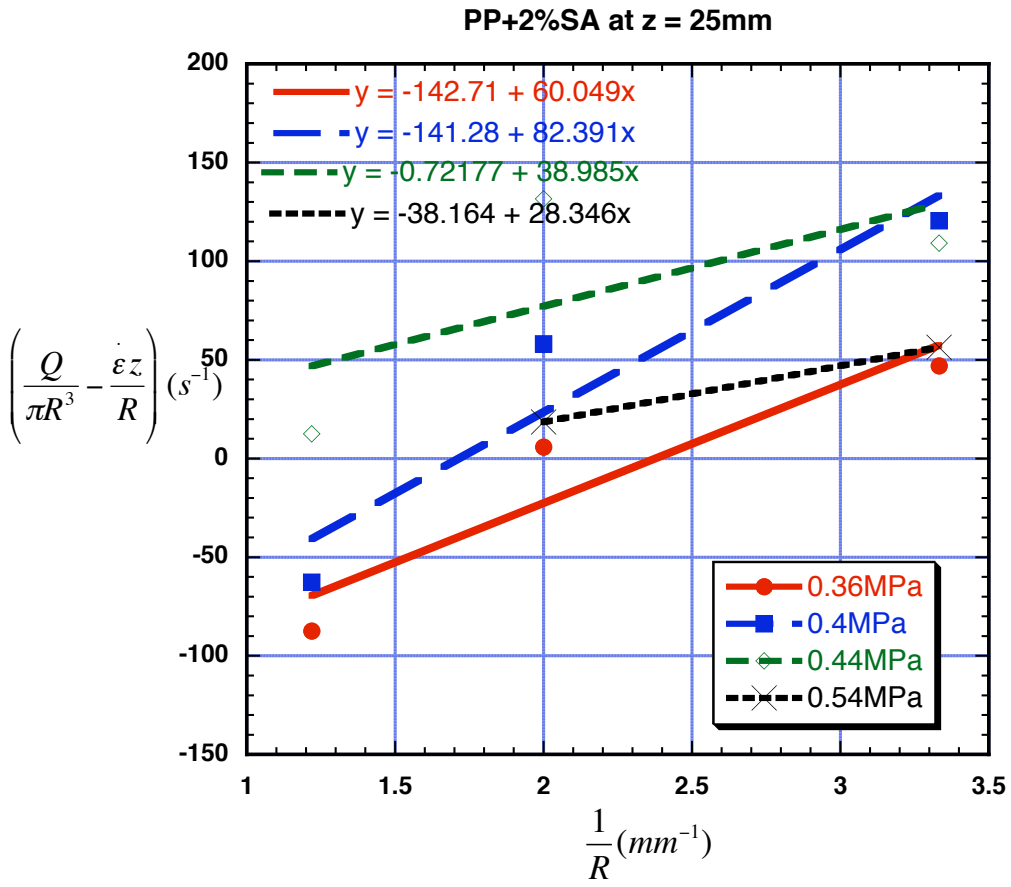

Figure 45: Plot of $\frac{Q}{\pi R^3}-\frac{\dot{\varepsilon} z}{R}$ vs. $\frac{1}{R}$ in semi-hyperbolically converging dies at various constant elongational stress values for PP+2%SA at 220°C at $z = 25\,\text{mm}$

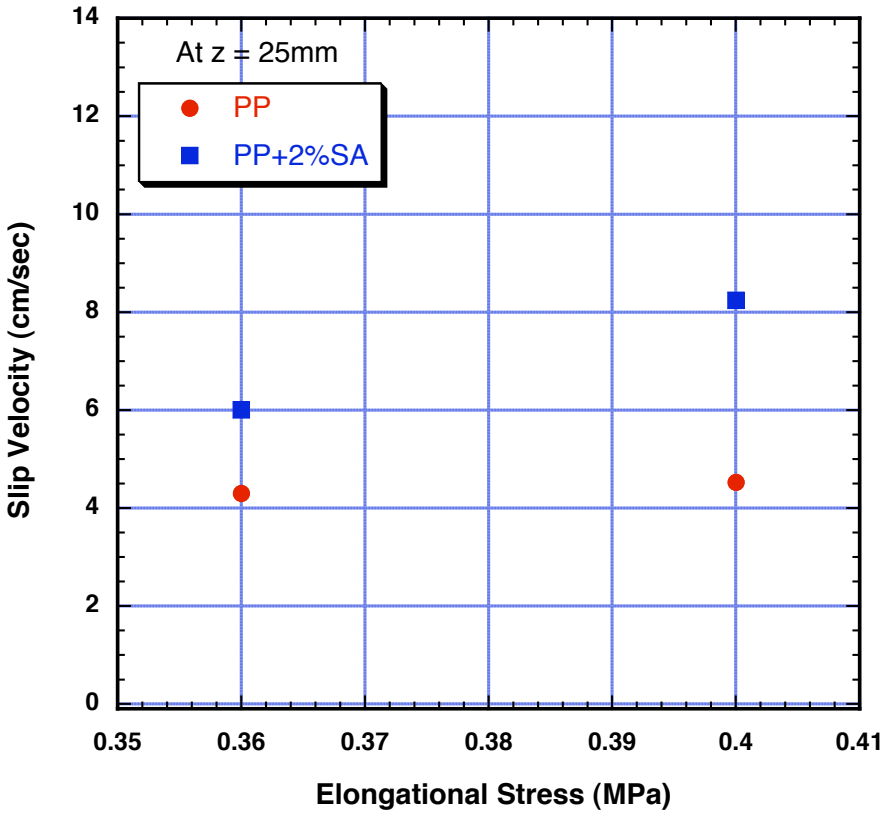

Figure 46: Plot of slip velocity vs. elongational stress values for PP and PP + 2% stearic acid at 220^{o}C in semi-hyperbolically converging dies

5.3. Comparison between the Slip Velocities in Capillary Dies and in Semi-hyperbolically Converging Dies

To summarize our results, we compare the slip velocities of the neat polymers and polymers plus additive. This comparison is quantified by the ratio

$$Ratio = \frac{v_s \, of \; neat \; thermoplastic}{v_s \, of \; neat \; thermoplastic \; plus \; additive} \tag{I.42}$$

This ratio is calculated for both the capillary dies and the semi-hyperbolically converging dies. The results are summarized in Table 7. We see that for capillary dies the ratio is relatively small. The ratio has the least value for PP and the highest for LDPE. This is consistent with the amount of shear viscosity reduction we have obtained for these polymers. In shear flow, the slip velocities for the thermoplastic plus additive increase notably from just the neat thermoplastic; we thus expect this ratio to be small.

From the ratios listed for the SHCDs in Table 7, we see that this ratio is much higher in this case, which implies that the slip velocity values do not increase much when the additive is used. This indicates that the neat polymer already is experiencing a greater degree of slip in the semi-hyperbolically converging dies, and thus the addition of the carboxylic acid does not bring about as great an increase in the slip velocity. For PP, we get a ratio of 0.6103, and for HDPE we get the highest ratio 0.8706. Thus, HDPE experiences the largest amount of slip in the pure form in the SHCD. Unfortunately, there was too much scatter in the experimental data to calculate a meaningful ratio for LDPE. The source of this error is thought to arise in the fact

Table 7: Ratio of slip velocities of neat thermoplastics to the slip velocities of neat thermoplastics plus additive for PP, HDPE, and LDPE

	Ratio in capillary dies	**Ratio in SHCD**
PP	0.0728	0.6103
HDPE	0.2087	0.8706
LDPE	0.2243	?

(already mentioned) that neat LDPE in the SHCDs appeared to have a very low degree of slip; hence the assumptions used to derive the modified Mooney equation were not valid.

We can conclude that the neat thermoplastics experience a greater degree of slip in the semi-hyperbolically converging dies than in capillary dies, and at relatively lower values of $\dot{\varepsilon}$ than of $\dot{\gamma}$. This is most likely due to the greater degree of molecular orientation imposed by the SHCDs on the flowing polymer sample. However, as witnessed by the experimental results for LDPE, this conclusion is not universally valid, and can easily cause the type of discrepancies in elongational viscosity data observed in Figure 11.

CHAPTER 6. CONCLUSIONS AND FUTURE WORK

6.1. Conclusions

We have studied the slip behavior of thermoplastic polymer melts in capillary dies and in semi-hyperbolically converging dies with the help of a carboxylic acid additive. Shear experiments were carried out to characterize the polymers, which showed consistent and high reductions in shear viscosities. Average shear stress reduction of up to 50% was observed with a small amount of stearic acid added to the polymer melt. The degree of stress reduction is not strongly dependent on the stearic acid concentration. The slip velocities were calculated in shear flow using Mooney's analysis. The slip velocities for the neat thermoplastics were more or less constant with increasing shear stress and relatively small; however, the slip velocities for the thermoplastics plus additive were found to increase exponentially with increasing shear stress.

Experiments using the semi-hyperbolically converging dies exhibit viscosity reduction on the order of only 10-15%, at most, at lower Hencky values. As the Hencky value of the die increases, the pure sample experiences more slip in the die, and hence the degree of reduction decreases. The neat polymer melts experience a greater degree of slip in the semi-hyperbolically converging dies than in capillary dies. The slip velocities for the semi-hyperbolically converging dies were calculated using a modified Mooney analysis.

This work corroborated the fact that neat polymer melts can experience greater degrees of slip at the walls of the semi-hyperbolically convergent dies than in capillary dies. Also from the computational results of Feigl et al. [26] and the present experimental work, we can conclude that the semi-hyperbolically convergent dies can give a good approximation of purely elongational flow at high Hencky strains, for many polymer melts.

6.2. Future Work

In the future, more simulation studies of actual polymeric liquids are needed to appreciate more fully the effect of the degree of wall slip on the nature of the flow field within the semi-hyperbolically converging die. These studies should concentrate on simulating various types and degrees of slip boundary conditions at the wall. For example, what is the effect on the flow field within the die of various degrees of stick-slip boundary conditions?

REFERENCES

1. C.D. Han, *Rheology in polymer processing*. 1976, New York: Academic Press, Inc.
2. C.W. Macosko, *Rheology: Principles, Measurements, and Applications*. 1994, New York: VCH Publishers, Inc.
3. H. A. Barnes, J. F. Hutton, and K. Walters, *An Introduction to Rheology*. 1989, Amsterdam: Elsevier science publishers B. V.
4. F.A. Morrison, *Understanding Rheology*. 2001, New York: Oxford University Press.
5. R. B. Bird, R. C. Armstrong, and O. Hassager, *Dynamics of Polymeric Liquids, Vol. 1- Fluid Mechanics*. 2nd ed. 1987, New York: John Wiley and Sons, Inc.
6. R. Darby, *Viscoelastic Fluids*. 1976, New York: Marcel Dekker.
7. J. Meissner, *Experimental aspects in polymer melt elongational rheometry.* Chem. Eng. Commun., 1985. **33**: p. 159-180.
8. F.N. Cogswell, *Measuring the Extensional Rheology of Polymer Melts.* Trans. Soc. Rheol, 1972. **16**: p. 383-403.
9. J. Meissner, *Development of a universal extensional rheometer for the uniaxial extension of polymer melts.* Trans. Soc. Rheol, 1972. **16**: p. 405-420.
10. J. Meissner and J. Hostettler, *A new elongational rheometer for polymer melts and other highly viscoelastic liquids.* Rheol. Acta, 1994. **33**: p. 1-21.
11. F.N. Cogswell, *Converging flow of polymer melts in extrusion dies.* Polym. Eng. Sci., 1972. **12**: p. 64-73.

12. D.M. Binding, *Further considerations of axisymmetric contraction flows.* J. Non-Newtonian Fluid Mech., 1991. **41**: p. 27-42.

13. D.M. Binding, *An approximate analysis for contraction and converging flows.* J. Non-Newtonian Fluid Mech., 1988. **27**: p. 173-189.

14. F.N. Cogswell, *Rheology of polymer melts under tension.* Plastics and Polymers, 1968. **36**: p. 109-111.

15. H. Munstedt, *Viscoelasticity of polystyrene melts in tensile creep experiments.* Rheol. Acta, 1975. **14**: p. 1077-1088.

16. H. Munstedt, *New universal extensional rheometer for polymer melts. Measurements on a polystyrene sample.* J. Rheol., 1979. **23**: p. 421-436.

17. H. Munstedt and H.M. Laun, *Elongational properties and molecular structure of polyethylene melts.* Rheol. Acta, 1981. **20**: p. 211-221.

18. D. F. James, G. M. Chandler, and S.J. Armour, *A converging channel rheometer for the measurement of extensional viscosity.* J. Non-Newtonian Fluid Mech., 1990. **35**: p. 421-443.

19. D. F. James, G. M. Chandler, and S.J. Armour, *Measurement of the extensional viscosity of M1 in a converging channel rheometer.* J. Non-Newtonian Fluid Mech., 1990. **35**: p. 445-458.

20. T. Sridhar, et al., *Measurement of extensional viscosity of polymer solutions.* J. Non-Newtonian Fluid Mech., 1991. **40**: p. 271-280.

21. J.R. Collier. 2001: U.S. Patent.

22. A. V. Pendse and J.R. Collier, *Elongational viscosity of polymer melts: A lubricated skin-core flow approach.* J. Appl. Polym. Sci., 1996. **59**: p. 1305-1314.

23. J. R. Collier, O. Romanoschi, and S. Petrovan, *Elongational rheology of polymer melts and solutions.* J. Appl. Polym. Sci., 1998. **69**: p. 2357-2367.

24. S. Petrovan, J. R. Collier, and G.H. Morton, *Rheology of cellulosic N-methylmorpholine oxide monohydrate solutions.* J. Appl. Polym. Sci., 2000. **77**: p. 1369-1377.

25. S. Petrovan, J. R. Collier, and I.I. Negulescu, *Rheology of cellulosic N-methylmorpholine oxide monohydrate solutions of different degrees of polymerization.* J. Appl. Polym. Sci., 2000. **79**: p. 396-405.

26. K. Feigl, et al., *A numerical study of the measurement of elongational viscosity of polymeric fluids in a semi-hyperbolically converging die.* J. Non-Newtonian Fluid Mech., 2003. **115**: p. 191-215.

27. S. Ahn and J.L. White, *Influence of carboxylic acid additives on the flow behaviour of molten thermoplastics.* J. Appl. Polym. Sci., 2003. **90**: p. 1555-1564.

28. F.T. Trouton, *On the coefficient of viscous traction and its relation to that of viscosity.* Proceedings of the Royal Society A77, 1906: p. 426.

29. A.E.E. Jr., J. Appl. Polym. Sci., 1976. **20**: p. 1137.

30. Y. Ide and J.L. White, *Experimental study of elongational flow and failure of polymer melts.* J. Appl. Polym. Sci., 1978. **22**: p. 1061.

31. D. H. Sebastian and J.R. Dearborn, *Elongation rheology of polyolefins and its relation to processability.* Polym. Eng. Sci., 1983. **23**: p. 572.

32. W. Minoshima and J.L. White, *A comparative experimental study of the isothermal shear and uniaxial elongational rheological propertiesof low density, high density and linear low density polyethylenes.* J. Non-Newtonian Fluid Mech., 1986. **19**: p. 251.

33. H.M. Laun and H. Schuch, *Transient Elongational Viscosities And Drawability Of Polymer Melts.* Journal Of Rheology, 1989. **33**(1): p. 119-175.

34. N.E. Hudson and J. Ferguson, *Correlation And Molecular Interpretation Of Data Obtained In Elongational Flow.* Transactions Of The Society Of Rheology, 1976. **20**(2): p. 265-286.

35. J. Ferguson and M.K.H. Eltawashi, *The Measurement Of The Elongational Viscosity Of Polymer-Solutions.* Journal Of Rheology, 1980. **24**(6): p. 946-946.

36. D.M. Binding and K. Walters, *On The Use Of Flow Through A Contraction In Estimating The Extensional Viscosity Of Mobile Polymer-Solutions.* Journal Of Non-Newtonian Fluid Mechanics, 1988. **30**(2-3): p. 233-250.

37. D.M. Binding and D.M. Jones, *On The Interpretation Of Data From Converging Flow Rheometers.* Rheologica Acta, 1989. **28**(3): p. 215-222.

38. D.M. Binding, D.M. Jones, and K. Walters, *The Shear And Extensional Flow Properties Of M1.* Journal Of Non-Newtonian Fluid Mechanics, 1990. **35**(2-3): p. 121-135.

39. S.A. White, A.D. Gotsis, and D.G. Baird, *Review Of The Entry Flow Problem - Experimental And Numerical.* Journal Of Non-Newtonian Fluid Mechanics, 1987. **24**(2): p. 121-160.

40. G. Pearson and S. Middleman, *Elongational Flow Behavior Of Viscoelastic Liquids.1. Modeling Of Bubble Collapse.* Aiche Journal, 1977. **23**(5): p. 714-722.

41. G. Pearson and S. Middleman, *Elongational Flow Behavior Of Viscoelastic Liquids.2. Definition And Measurement Of Apparent Elongational Viscosity.* Aiche Journal, 1977. **23**(5): p. 722-725.

42. S.L. Ng, et al., *Extensional viscosity measurements of dilute solutions of various polymers.* Journal Of Non-Newtonian Fluid Mechanics, 1996. **65**(2-3): p. 291-298.

43. M.E. Mackay, et al., *An Approximate Technique To Determine Elongation Stresses In Stagnation Flow.* Journal Of Rheology, 1995. **39**(1): p. 1-14.

44. G.G. Fuller, et al., *Extensional Viscosity Measurements For Low-Viscosity Fluids.* Journal Of Rheology, 1987. **31**(3): p. 235-249.

45. D.M. Jones, K. Walters, and P.R. Williams, *On The Extensional Viscosity Of Mobile Polymer-Solutions.* Rheologica Acta, 1987. **26**(1): p. 20-30.

46. P.R. Williams and R.W. Williams, *On The Planar Extensional Viscosity Of Mobile Liquids.* Journal Of Non-Newtonian Fluid Mechanics, 1985. **19**(1): p. 53-80.

47. H.H. Winter, C.W. Macosko, and K.E. Bennett, *Orthogonal Stagnation Flow, A Framework For Steady Extensional Flow Experiments.* Rheologica Acta, 1979. **18**(3): p. 323-334.

48. T. Sridhar, *An Overview Of The Project-M1.* Journal Of Non-Newtonian Fluid Mechanics, 1990. **35**(2-3): p. 85-92.

49. D.A. Nguyen and T. Sridhar, *Preparation And Some Properties Of M1 And Its Constituents.* Journal Of Non-Newtonian Fluid Mechanics, 1990. **35**(2-3): p. 93-104.

50. J. Ferguson and N.E. Hudson, *The Extensional-Properties Of M1 Obtained From The Carri-Med Elongational Viscometer.* Journal Of Non-Newtonian Fluid Mechanics, 1990. **35**(2-3): p. 197-205.

51. D.A. Nguyen, R.K. Gupta, and T. Sridhar, *Experimental Results And Constitutive Modeling Of The Extensional Flow Of M1.* Journal Of Non-Newtonian Fluid Mechanics, 1990. **35**(2-3): p. 207-214.

52. D.R. Oliver, *The Horizontal Stretching Of Test Liquid M1.* Journal Of Non-Newtonian Fluid Mechanics, 1990. **35**(2-3): p. 251-261.

53. D.V. Boger and R.J. Binnington, *Circular Entry Flows Of Fluid M1.* Journal Of Non-Newtonian Fluid Mechanics, 1990. **35**(2-3): p. 339-360.

54. D.F. James, G.M. Chandler, and S.J. Armour, *A Converging Channel Rheometer For The Measurement Of Extensional Viscosity.* Journal Of Non-Newtonian Fluid Mechanics, 1990. **35**(2-3): p. 421-443.

55. D.F. James, G.M. Chandler, and S.J. Armour, *Measurement Of The Extensional Viscosity Of M1 In A Converging Channel Rheometer.* Journal Of Non-Newtonian Fluid Mechanics, 1990. **35**(2-3): p. 445-458.

56. H.M. Laun and R. Hingmann, *Rheological Characterization Of The Fluid M1 And Of Its Components.* Journal Of Non-Newtonian Fluid Mechanics, 1990. **35**(2-3): p. 137-157.

57. A.J. Muller, J.A. Odell, and J.P. Tatham, *Stagnation-Point Extensional Flow Behavior Of M1.* Journal Of Non-Newtonian Fluid Mechanics, 1990. **35**(2-3): p. 231-250.

58. A.V. Ramamurthy, *Wall slip in viscous fluids and the influence of materials of construction.* J. Rheol., 1986. **30**: p. 337-357.

59. A.V. Ramamurthy, *LLDPE rheology and blown film fabrication.* Adv. Polym. Techn., 1986. **6**: p. 489-499.

60. D.S. Kalika and M.M. Denn, *Wall slip and extrudate distortion in linear low-density polyethylene.* J. Rheol., 1987. **31**: p. 815-834.

61. F. R. Lim and W.R. Schowalter, *Wall slip of narrow molecular weight distribution polybutadienes.* J. Rheol., 1989. **33**: p. 1359-1382.

62. S. G. Hatzikiriakos and J.M. Dealy, *Wall slip of molten high-density polyethylenes. I. Sliding plate rheomoeter studies.* J. Rheol., 1991. **35**: p. 497-523.

63. S. G. Hatzikiriakos and J.M. Dealy, *Wall slip of molten high-density polyethylenes. II. Capillary rheometer studies.* J. Rheol., 1992. **36**: p. 703-741.

64. P.A. Drda and S.Q. Wang, *Stick-slip transition at polymer melt/solid interfaces.* Phys. Rev. Lett., 1995. **75**: p. 2698-2701.

65. S.G. Hatzikiriakos, *Wall Slip Of Molten Polymers.* Abstracts Of Papers Of The American Chemical Society, 1995. **209**: p. 12-POLY.

66. S.H. Anastasiadis and S.G. Hatzikiriakos, *The work of adhesion of polymer/wall interfaces and its association with the onset of wall slip.* Journal Of Rheology, 1998. **42**(4): p. 795-812.

67. V. Mhetar and L.A. Archer, *Slip in entangled polymer melts. 1. General features.* Macromolecules, 1998. **31**(24): p. 8607-8616.

68. Y.L. Yeow, et al., *A new method of processing capillary viscometry data in the presence of wall slip.* J. Rheol., 2003. **47**: p. 337-348.

69. S.G. Hatzikiriakos, C.W. Stewart, and J.M. Dealy, *Effect Of Surface-Coatings On Wall Slip Of Lldpe.* International Polymer Processing, 1993. **8**(1): p. 30-35.

70. S.G. Hatzikiriakos, et al., *The Effect Of Teflon(Tm) Coatings In Polyethylene Capillary Extrusion.* Journal Of Applied Polymer Science, 1995. **55**(4): p. 595-603.

71. J.M. Piau, N. Kissi, and A. Mezghani, *Slip-Flow Of Polybutadiene Through Fluorinated Dies.* Journal Of Non-Newtonian Fluid Mechanics, 1995. **59**(1): p. 11-30.

72. E.E. Rosenbaum and S.G. Hatzikiriakos, *Wall slip in the capillary flow of molten polymers subject to viscous heating.* Aiche Journal, 1997. **43**(3): p. 598-608.

73. J.R. Barone and S.Q. Wang, *Adhesive wall slip on organic surfaces.* Journal Of Non-Newtonian Fluid Mechanics, 2000. **91**(1): p. 31-36.

74. E.C. Achilleos, G. Georgiou, and S.G. Hatzikiriakos, *Role of processing aids in the extrusion of molten polymers.* Journal Of Vinyl & Additive Technology, 2002. **8**(1): p. 7-24.

75. S.G. Hatzikiriakos, *Enhanced polymer processing aids.* Journal Of Vinyl & Additive Technology, 2002. **8**(4): p. 223-224.

76. S. Ahn and J.L. White, *Influence of low molecular weight additives on die extrusion rheometer flow of thermoplastic melts.* International Polymer Processing, 2003. **18**(3): p. 243-251.

77. S.G. Hatzikiriakos and N. Rathod, *Boron nitride based processing aids.* Korea-Australia Rheology Journal, 2003. **15**(4): p. 173-178.

78. M. Sentmanat and S.G. Hatzikiriakos, *Mechanism of gross melt fracture elimination in the extrusion of polyethylenes in the presence of boron nitride.* Rheologica Acta, 2004. **43**(6): p. 624-633.

79. N. Rathod and S.G. Hatzikiriakos, *The effect of surface energy of boron nitride on polymer processability.* Polymer Engineering And Science, 2004. **44**(8): p. 1543-1550.

80. E.B. Muliawan, S.G. Hatzikiriakos, and S. M., *Melt fracture of linear PE.* International Polymer Processing, 2005. **20**(1): p. 60-67.

81. M. Mooney, *Explicit formulas for slip and fluidity.* J. Rheol., 1931. **2**: p. 210-222.

82. A. D. Gotsis and A. Odriozola, *The relevance of entry flow measurements for the estimation of extensional viscosity of polymer melts.* Rheo. Acta., 1998. **37**: p. 430-437.

83. P. Beaupre and M. Gupta, *A comparison of axisymmetric and planar elongational viscosities of PE-LD.* Inter. Polym. Pro. J., 2002. **17**: p. 370-375.

84. M. Zatloukal, et al., *Improvement in techniques for the determination of extensional rheological data from entrance flows: computational and experimental analysis (vol 107, pg 13, 2002).* Journal Of Non-Newtonian Fluid Mechanics, 2003. **109**(1): p. 91-91.

85. P. Patil, *Measurement of elongational rheology of polymer melts using semi-hyperbolically convergent dies*. 2002, The University of Tennessee: Knoxville.

86. J. R. Collier, S. Petrovan, and P. Patil, *Hencky strain shifting of convergent flow measured effective elongational viscosity.* J. Appl. Polym. Sci., 2002. **87**: p. 1397-1404.

87. H.J. Park, et al., *Numerical-Simulation In Converging Channel Flow Of The Fluid M1 Using An Integral Constitutive Equation.* Journal Of Non-Newtonian Fluid Mechanics, 1994. **52**(1): p. 69-89.

88. D.M. Kalyon and H. Gevgilili, *Wall slip and extrudate distortion of three polymer melts.* J. Rheol., 2003. **47**: p. 683-699.

Part II: Shear Thickening in Dilute Polymer Solutions: Transient Analysis

This part is revised slightly from a paper by the same name published in the journal of 'Chemical Engineering Communications' in 2005. The full citation is:

P.A. Kamerkar, B.J. Edwards, D.J. Keffer, and C.W. Reneau, "Shear Thickening in Dilute Polymer Solutions: Transient Analysis", *Chemical Engineering Communications,* 192, 89-107 (2005).

In this part, 'we' refers to my co-authors and myself. My primary contributions include: (1) computation of the transient data and analysis; (2) most of the writing.

CHAPTER 1. INTRODUCTION

It is well known that dilute polymeric solutions typically display *shear-thinning* behavior under the application of shear; i.e., their viscosities decrease with increasing shear rate [1]. However, some of these fluids exhibit an anomalous behavior at high shear rates: it is observed that, under very specific conditions, their viscosities actually increase with the magnitude of applied shear rate, provided that the rate of shear is large enough [2-5]. This phenomenon is called *shear thickening*. The manifestations of shear thickening can occur in dilute, low-viscosity solutions when the molecular weight of the dissolved polymer is very high, the concentration of polymer lies within a certain range, and the shear rate is relatively large.

Ten years ago, the cause of shear thickening in these dilute solutions was finally resolved. The work by Kishbaugh and McHugh [2, 3, 6] provided the definitive connection between the anomaly of shear thickening at high shear rates and

shear-induced structure formation. They found that the shear thickening arises due to *intermolecular* interactions, not *intramolecular* interactions, as ascertained through extensive experimentation: a rheo-optical technique was used to measure the rheological and optical responses of the solutions in the initial shear-thinning regime and subsequent shear-thickening region. The results of the experiments conclusively demonstrated that the shear thickening behavior was associated with supermolecular structure formation.

Although the experimental investigations of Kishbaugh and McHugh could delineate the phenomena of shear thickening in polymeric solutions, there was no self-consistent theory that could potentially describe all of the experimental observations at that time. However, the recent work by Edwards et al. [7] provided a single theory that could explain both the rheological and optical behavior simultaneously, while offering predictions for rheological characteristic functions, such as the first and second normal stress coefficients, that were not measured experimentally.

According to the Two Coupled Maxwell Modes (TCMM) Model [7], associations (or structures) of the individual polymer chains start growing in size and aspect ratio at small values of the shear rate below $\dot{\gamma}_c$, the critical shear rate for the onset of shear thickening—see Figure 47*. These associations actually lower the viscosity in the solution by relieving some of the stress acting on the polymer chains as the structures increase in size and aspect ratio. This augments the natural intramolecular chain shear thinning of the dilute solutions. At the critical shear rate,

* All the figures and tables for Part II are included in the appendix for this part.

$\dot{\gamma}_c$, these structures become too distended to be supported by the hydrodynamic forces acting on them. This results from the decrease in the viscosity of the shear thinning solution. Thus the structures begin to decrease in size and aspect ratio in response to the lowered degree of shear force exerted upon them. This reduction in size restricts the stress relief offered to the solution dynamics, and, consequently, the viscosity increases with increasing shear rate. At higher values of the shear rate, the structures become totally isotropic, at $\dot{\gamma}_m$, at which point a shear-thinning behavior resumes as the intra-chain dynamics again dictate the qualitative behavior of the shear viscosity curve—see Figure 47.

In the previous publication [7], the analysis was limited to steady-state shear flow; however, the rheological and optical experimental data of Kishbaugh and McHugh [2, 3] also contained limited transient data taken during start up, steady-state, and cessation of the shear flow experiments. This transient behavior is very interesting in its own right, and can also be described by the TCMM Model. Indeed, as we shall see, it can also be used to add further credibility to the predictions of the said model. Consequently, in this part, we extend the analysis of Edwards et al. [7] from the steady flow regime to the transient flow regime, and compare predictions of the TCMM Model with the transient flow experiments of Kishbaugh and McHugh [2, 3]. Also, as in the preceding paper [7], we offer predictions for rheological properties (but time-dependent predictions this time) that have not been measured experimentally.

CHAPTER 2. THEORETICAL BACKGROUND

2.1 The Two Coupled Maxwell Modes Model

The TCMM Model characterizes the essential qualitative and semi-quantitative behavior of polymeric fluids [8]. It has evolved from the thermodynamic methodology developed by Grmela [9, 10] and Beris and Edwards [11-13]. The Multiple Coupled Maxwell Modes Model was first introduced in [11], and reduced to a two-mode version in [8]. Use of this two-mode model was shown to reproduce faithfully all of the essential qualitative features of polymeric viscoelastic fluids [8]; quantitative reproductions can be achieved through the use of additional (often uncoupled) modes.

To examine the behavior of dilute polymer solutions with structure formation, the TCMM Model is applied using two second-rank mode-conformation tensors, $\mathbf{c}^1$ and $\mathbf{c}^2$. The first mode-conformation tensor, $\mathbf{c}^1(\mathbf{x},t)$, is the second moment of the orientational distribution function, $\psi(\mathbf{x},\mathbf{R},t)$ [1]:

$$\mathbf{c}^1 = \int \mathbf{RR}\,\psi\, d^3R \tag{II.1}$$

In this expression, $\mathbf{R}$ is the end-to-end vector of a dissolved polymer chain and $\mathbf{x}$ is the Eulerian coordinate denoting the spatial position of the chain's center of mass. According to Eq. (1), $\mathbf{c}^1$ has units of length squared. The second mode tensor, $\mathbf{c}^2(\mathbf{x},t)$, quantifies the size, shape, and orientation of the intermolecular structures that are formed during shear [7]. Using as the size distribution function $f(\mathbf{x},\mathbf{a},t)$, with $\mathbf{a}$

the vector spanning the major axis of a spheroidal structure, the second mode tensor can be defined as [7]

$$\mathbf{c}^2 = \int \mathbf{aa}\ f\, d^3a \tag{II.2}$$

The eigenvalues and eigenvectors of these second-rank tensors quantify the degree of orientation and the characteristic directions, respectively, of the two relaxation modes [7, 8].

In a homogeneous flow field, the evolution equations for the mode-conformation tensors can be decoupled from the Cauchy momentum equation and solved independently for known kinematics. These evolution equations are

$$\frac{\partial c^1_{\alpha\beta}}{\partial t} - c^1_{\alpha\gamma}\nabla_\gamma v_\beta - c^1_{\beta_\gamma}\nabla_\gamma v_\alpha = -\frac{1}{\lambda_1}c^1_{\alpha\beta} + \frac{k_BT}{\lambda_1 K_1}\delta_{\alpha\beta} - \frac{\theta}{2k_BT}\sqrt{\frac{n_2}{n_1}}\frac{1}{\sqrt{\lambda_1\lambda_2}}\times$$

$$\left[K_2\left(c^1_{\alpha\gamma}c^2_{\beta_\gamma} + c^2_{\alpha\gamma}c^1_{\beta_\gamma}\right) - 2k_BTc^1_{\alpha\beta}\right] \tag{II.3}$$

$$\frac{\partial c^2_{\alpha\beta}}{\partial t} - c^2_{\alpha\gamma}\nabla_\gamma v_\beta - c^2_{\beta_\gamma}\nabla_\gamma v_\alpha = -\frac{1}{\lambda_2}c^2_{\alpha\beta} + \frac{k_BT}{\lambda_2 K_2}\delta_{\alpha\beta} - \frac{\theta}{2k_BT}\sqrt{\frac{n_2}{n_1}}\frac{1}{\sqrt{\lambda_1\lambda_2}}\times$$

$$\left[K_1\left(c^1_{\alpha\gamma}c^2_{\beta_\gamma} + c^2_{\alpha\gamma}c^1_{\beta_\gamma}\right) - 2k_BTc^2_{\alpha\beta}\right] \tag{II.4}$$

In these expressions, k_B is the Boltzmann constant, T is the absolute temperature, K_1, K_2 are the Hookean spring constants of the free polymer chains and structures (respectively), λ_1, λ_2 are the relaxation times of the two modes, n_1, n_2 are the effective concentrations, and θ is the degree of interaction between the two modes.

For the model to be physically feasible, λ_1, λ_2, n_1, and n_2 must all have values greater than or equal to zero. Thermodynamically, it appears that θ should lie within the range of $[-1, 1]$. It is typically a small positive fraction [7, 8, 11].

2.2 Rheological Properties

According to the TCMM Model [8, 11], the extra stress tensor is given by a linear sum over the two mode-conformation tensors:

$$\sigma_{\alpha\beta} = \sum_{i=1}^{2} \left(n_i N_A K_i c^i_{\alpha\beta} - n_i N_A k_B T \delta_{\alpha\beta} \right) \tag{II.5}$$

where N_A is Avogadro's number. This second-rank tensor has units of force per length squared, and the shear viscosity, η, is calculated by dividing the shear stress component, σ_{12}, by the shear rate, $\dot{\gamma}$. The first and second normal stress coefficients are defined as $\Psi_1 \equiv (\sigma_{11} - \sigma_{22}) / \dot{\gamma}^2$ and $\Psi_2 \equiv (\sigma_{22} - \sigma_{33}) / \dot{\gamma}^2$, respectively.

2.3 Optical Properties: Dichroism

The TCMM Model describes more than just the rheological properties of polymeric materials: it can also be used to determine the optical properties of the deforming liquid. The dichroic signal, $\Delta n''$, is calculated using both modes by summation of the following two equations [2, 6, 7]:

$$\Delta n''_1 = \frac{4\pi}{5} k^3 \frac{c N_A m_s}{M} (\alpha_1^2 - \alpha_2^2)_1 [\mathrm{tr}\,\tilde{\mathbf{c}}^1 - 3] \tag{II.6}$$

$$\Delta n_2'' = \frac{8\pi}{15} m_p n_2 N_A k^3 (\alpha_1^2 - \alpha_2^2)_2 \frac{b}{(1 + 36/\sigma^2)} \tag{II.7}$$

The first equation is the innate dichroism of the individual polymer chains. The parameters appearing in this equation are as follows: wave number, $k = (2\pi/6.328 \times 10^{-7})\,\mathrm{m}^{-1}$, polymer concentration, c, molecular weight, M, the refractive index of the solvent, m_s=1.475 [2, 6], and the polarizability difference, $(\alpha_1^2 - \alpha_2^2)_1$. This last quantity was estimated by Kishbaugh and McHugh as -1.25×10^{-42} cm^3/molecule using the method of Gurnee [14]. Since $\mathrm{tr}\,\tilde{\mathbf{c}}^1$ is always greater than three, this contribution to the dichroic signal is always negative in sign.

The second equation, (7), is the dichroism arising from the supermolecular structures according to the Rayleigh Scattering Theory [2, 6, 7]. The quantities appearing in this expression are the refractive index of the polymer, $m_p = 1.59$ [2, 6], and several other model-specific functions. The first is an anisotropy function that depends on the shape of the structure, p:

$$b = \frac{p^2 - 1}{p^2 + 1} \tag{II.8}$$

with p taken as [7]

$$p = (1 + \frac{3}{2}[\mathrm{tr}\,\tilde{\mathbf{c}}^2 - 3])^{3/4} \tag{II.9}$$

The quantity σ is a dimensionless measure of the shear rate relative to the size and shape of the assumed structures. It is given by [2, 6]

$$\sigma = \frac{\eta_S V_P \nu(p)}{k_B T}\dot{\gamma} \tag{II.10}$$

where V_p is the volume of the structure,

$$V_P = \frac{4\pi}{3p^2}a^3 = \frac{4\pi}{3p^2}([\mathrm{tr}\,\tilde{\mathbf{c}}^2 - 3]\langle \mathbf{aa}\rangle_0)^{3/2} \tag{II.11}$$

$\eta_S = 2.79$ cP for decalin, the solvent, at $25°C$, and

$$\frac{1}{\nu(p)} = \frac{p^2}{p^4+1}\left(-1 + \frac{2p^2-1}{2p\sqrt{p^2-1}}\ \ln\left[\frac{p+\sqrt{p^2-1}}{p-\sqrt{p^2-1}}\right]\right) \tag{II.12}$$

In Eq. (II.11), $\langle \mathbf{aa}\rangle_0$ is the diameter squared of the average structure in the limit of vanishing shear rate. A measure of the structure size can be obtained from $a = \sqrt{\lambda_p \langle \mathbf{aa}\rangle_0}$, where λ_p is the primary eigenvalue of $\tilde{\mathbf{c}}^2$ [7]. The last quantity appearing in Eq. (II.7) is the polarizability difference of the structures, $(\alpha_1^2 - \alpha_2^2)_2$. It is given by [2, 6, 7]

$$\frac{16\pi^2}{V_P^2}(\alpha_1^2 - \alpha_2^2)_2 = \left(\frac{1}{L_1 + 1/(m_s^2-1)}\right)^2 - \left(\frac{1}{L_2 + 1/(m_s^2-1)}\right)^2 \tag{II.13}$$

where

$$L_1 = \frac{1-e^2}{e^2}\left(-1 + \frac{1}{2e}\ln\left[\frac{1+e}{1-e}\right]\right) \tag{II.14}$$

$$L_2 = \frac{1-L_1}{2} \tag{II.15}$$

$$e^2 = \left(1 - \frac{1}{p^2}\right) \tag{II.16}$$

It can be shown that the contribution to the dichroic signal arising from the structures is always greater than or equal to zero.

It is important to note a hypothesis expressed in the previous study [7]: the dichroic orientation angle is dependent on which mode dominates the dichroism. When anisotropic structures are present, they dominate the dichroic signal since $\Delta n_2''$ is of greater magnitude than $\Delta n_1''$. Thus, for shear rates with significant structural anisotropy, the dichroic orientation angle is quantified by the primary eigenvector of $\tilde{\mathbf{c}}^2$. However, for extremely high values of the shear rate, after the dichroic signal has switched from positive to negative, this signal is now dominated by the free polymer chains, and thus the dichroic orientation angle is quantified by the primary eigenvector of $\tilde{\mathbf{c}}^1$. This hypothesis will be confirmed in this article.

2.4 Optical Properties: Birefringence

The TCMM Model also allows calculation of the linear birefringence, $\Delta n'$, according to the following equation [2, 6, 7]:

$$\Delta n' = 2\pi \frac{n_1 N_A}{\omega} m_s \left([\mathrm{tr}\,\tilde{\mathbf{c}}^1 - 3]\,\Theta_i + [\mathrm{tr}\,\tilde{\mathbf{c}}^1 - 3]\,\Theta_{fs} + 4\pi e_1 \Theta_f \right) \tag{II.17}$$

Three types of birefringence contribute to $\Delta n'$, but all of them arise from the free polymer chains: the birefringence associated with the anisotropy of the

supermolecular structures is several orders of magnitude smaller than that calculated according to the above expression [2, 6, 7], and is therefore excluded from Eq. (II.17). The quantity ω appearing in Eq. (II.17) is a magnitude corrector for the birefringence [7]. It essentially acts as another fitting parameter in the present paper.

The first term in Eq. (II.17) represents the intrinsic optical anisotropy of the free polymer chains. This term is proportional to Θ_i, which is given by [15]

$$\Theta_i = \frac{3}{5}(\alpha_1 - \alpha_2)_1 \tag{II.18}$$

The polarizability difference, $(\alpha_1 - \alpha_2)_1 = -5.49 \times 10^{-24}$ cm^3/molecule, is assigned the value calculated by Kishbaugh and McHugh [2, 6] using the method of Gurnee [14]. This contribution to the birefringent signal is always negative in sign.

The second contribution to the overall birefringence is from macroform anisotropy [16], which is due to the difference in the refractive indices of the polymer and solvent. In Eq. (II.17), this contribution is given by [2, 6, 7]

$$\Theta_f = \left(\frac{m_s^2 + 2}{3}\right)^2 \left(\frac{m_p^2 - m_s^2}{4\pi m_s \rho N_A}\right)^2 \frac{M^2}{v} \tag{II.19}$$

with

$$e_1^2 = \left(1 - \frac{1}{p_1^2}\right) \tag{II.20}$$

Note that p_1 appearing in Eq. (20) is a function of the trace of the first mode-conformation tensor, $p_1 = (1 + \frac{3}{2}[\mathrm{tr}\tilde{\mathbf{c}}^1 - 3])^{3/4}$ [7]. Furthermore, $\rho = 1.065$ g/ml for Polystyrene and $M^2/\nu = 2.083 \times 10^{25} M^{0.42}$. This contribution to $\Delta n'$ is always positive.

Microform anisotropy [17] accounts for the third contribution to the birefringence. It increases with the extension of the polymer chain, although it is still an effect arising due to the difference in refractive indices between the polymer molecules and solvent. The contribution is expressed by

$$\Theta_{fs} = \frac{3}{5}\left(\frac{m_s^2 + 2}{3}\right)^2 \left(\frac{m_p^2 - m_s^2}{4\pi m_s}\right)^2 \frac{4\pi M_0 \zeta e_s}{\rho N_A} \tag{II.21}$$

where $\zeta = 5.4$ is the number of monomeric units per statistical chain segment, $M_0 = 104$ g/mol is the monomer molecular weight, and $e_s = 0.1$ is the optical shape factor for the segment [2, 6]. This contribution to $\Delta n'$ is also always positive.

CHAPTER 3. EXPERIMENTS AND DATA FITTING

3.1 Transient Rheo-Optical Experiments

The steady-state rheo-optical data of Kishbaugh and McHugh [2, 3] was obtained using a Couette flow cell subjected to the transient shear-rate profile depicted in Figure 46. In these experiments, the shear rate was ramped up from rest to the steady-state shear rate value of interest, $\dot{\gamma}_{ss}$, in a two second time interval. The shear rate was held constant for 5 s, and then it was ramped back down to rest in another two-second interval. The 5 s steady-state interval was sufficient to allow the solutions to attain time-independent rheological and optical responses. These experiments were performed on Polystyrene/decalin solutions made from monodisperse polymer samples of various molecular weights over a range of concentrations at $25°C$.

3.2 Transient Data Fitting Using the TCMM Model

The transient flow profiles for both the rheological and optical data reported by Kishbaugh and McHugh [2, 3] will be analyzed in this section in terms of the TCMM Model. In order to reproduce the results obtained from the transient experiments, the TCMM Model must be applied to the transient shear profile of Figure 48. This is easiest to accomplish when working in terms of dimensionless quantities. Subsequently, the model predictions can be transformed back into dimensional quantities and compared with experimental data.

The evolution equations, (3) and (4), are made dimensionless by defining the dimensionless shear rate as $\tilde{\gamma} \equiv \dot{\gamma}\sqrt{\lambda_1\lambda_2}$, the dimensionless mode tensors as $\tilde{c}^i_{\alpha\beta} \equiv K_i c^i_{\alpha\beta}/k_BT$, and dimensionless time as $\tilde{t} \equiv t/\sqrt{\lambda_1\lambda_2}$. Consequently, the spring constants, K_1 and K_2, drop out of the analysis, and one is left with only five parameters, λ_1, λ_2, n_1, n_2, and θ, that must be fit to the experimental data.

Fitting the model to experimental data was accomplished using two different methods. In the first method, Method 1, values for the five parameters listed above, as well as $\langle \mathbf{aa} \rangle_0$, can be taken directly from the previous study [7, 18]. In other words, the parameters are fitted using only *steady-state* viscosity versus shear rate data. Then the coupled, non-linear, ordinary differential evolution equations, (II.3) and (II.4), were solved using the fourth-order Runge-Kutta algorithm, in accordance with the transient shear flow profile of Figure 48. These equations are well conditioned, and hence stability issues were not relevant. This method is very stable, and calculates time-dependent components of the two mode-conformation tensors to the desired degree of accuracy, in this case, to twelve significant figures. These components can then be converted into the requisite dimensional rheological and optical properties in a post-processing operation using Eqs. (II.5), (II.6), (II.7), and (II.17), and subsequently compared with available transient experimental data.

The second method, Method 2, was more complicated than the first. In this method, use is made of all available transient data taken for a given polymer molecular weight and concentration. Multiple transient dichroism profiles for various steady-

state shear rates are fitted simultaneously using the Nelder and Mead Downhill Simplex Method [19] to find the best set of six parameters, λ_1, λ_2, n_1, n_2, θ, and $\langle \mathbf{aa} \rangle_0$, which give the smallest objective function. This objective function was defined as

$$f_{obj} = \left(\sum_{i=1}^{n_{set}} f_{obj}^{i} \Big/ n_T \right)^{1/2} , \qquad f_{obj}^{i} = \sum_{j=1}^{n_d^i} w(j) \left(\frac{\Delta n''_{\text{expt}} - \Delta n''_{\text{model}}}{\Delta n''_{\text{expt}}} \right)^2 \tag{II.22}$$

where n_T is the total number of experimental data points from all transient dichroism profiles, n_{set} is the number of transient dichroism profiles, and n_d^i is the number of data points in the *i*-th data set. The weighting factor appearing in this expression was defined as $w(j) = 10$ when the experimental value of the dichroism was within 5% of its maximum value, and $w(j) = 1$ otherwise.

The objective function thus represents an average of differences between the theoretical calculations and the experimental transient profiles for a given set of parameters. The Nelder and Mead algorithm searches through the parameter space trying to minimize the objective function, solving at each iteration the coupled evolution equations, (3) and (4), and then calculating the dichroism to compare with the experimental transient dichroism profiles. (Dichroism profiles were used for the fitting, as opposed to stress or viscosity profiles, because none of the latter were presented in Refs. [2, 3].) After the objective function was minimized, the parameters corresponding to this value of the objective function were used to compare the TCMM Model with the transient experimental profiles.

CHAPTER 4. RESULTS

In all cases, data fitting was hindered by the limited transient data presented in the Kishbaugh and McHugh publications [2, 3]. However, a sufficient amount of data could be gleaned from these sources to come to some significant conclusions, as described below.

4.1 Dichroism

Two sets of experimental transient dichroism curves are presented in Refs. [2, 3]. The first set is presented in Figures 49 and 50, along with TCMM Model fits for the two data fitting methods described in the preceding section. Experimental data in Figures 49 and 50 is for a solution of 6.8×10^{6} g/mol Polystyrene dissolved in decalin at a concentration of 0.30 g/dl. (In this and subsequent figures, only a sampling of results at specific values of the steady-state shear rate are shown; displayed results are typical.) The dashed curve corresponds to parameter values obtained using Method 1; these parameter values were obtained in [7], and are collected in Table 8. Recall that these parameter values were obtained using steady-state viscosity vs. shear rate curves [7], such as represented symbolically in Figure 47. The solid curve corresponds to parameter values obtained via Method 2, which are also collected in Table 8. Recall that these parameters were obtained by optimizing all available dichroism vs. time curves simultaneously.

As evident, both sets of parameters describe well the qualitative features of the transient dichroism curves, but the latter set offers a fair deal of quantitative

improvement, especially at lower shear rate values. The reason for this is apparent: the parameter values from Method 1 were obtained from the best model fit to steady-state viscosity vs. shear rate data, whereas Method 2 optimized the parameters to transient dichroism data, including those displayed in the figures. For this particular solution, no shear thickening was observed in the steady-state viscosity versus shear rate curve, nor did a maximum occur in the steady-state dichroism versus shear rate curve [2, 3, 7]. At this concentration, the structure size increased with increasing shear rate, eventually reaching a limiting size at high shear rates [7]. According to the model and the experimental data, the size of the structures increases and the shape elongates monotonically to the steady-state structure size and shape upon start up of shear, and decrease back to their quiescent values upon flow cessation.

Note that both theory and experiment coincide on another point: the dynamical response of the solution at any time is at a pseudo steady state. In other words, during start up and cessation of flow, the instantaneous value of the shear rate determines the instantaneous values of all rheological and optical properties as if the flow field was at steady state with that particular value of the shear rate.

The orientation angles of the structures relative to the direction of flow are displayed in Figure 51 for one value of the steady-state shear rate. Here, only the TCMM Model fit is displayed for the parameter values obtained via the more accurate Method 2. The model predicts well the transient qualitative features of the experimental data, including the initial rapid changes immediately after start up and immediately before total flow cessation. Note that the experimental data contains

much noise at very small and long times due to the method in which the orientation angle is calculated from the raw intensity data [2, 3]. This noise is not present in the TCMM Model predictions, since the computational algorithm is not subject to measurement error. At both values of the steady-state shear rate, the orientation angle drops quickly from its zero shear rate limit of $45°$ to a value fairly close to the direction of flow, and then returns to $45°$ upon flow cessation.

The second set of dichroism data are much more interesting than the first in that this solution, a 1.54×10^6 g/mol Polystyrene /decalin solution at a concentration of 0.79 g/dl, corresponds to a case in which the steady-state viscosity curve displays a minimum and the steady-state dichroism curve displays a maximum. Results of the TCMM Model fit to the experimental data using the more accurate Method 2 are presented in Figures 52-54. At the lowest value of the shear rate (not shown), the TCMM Model captures the qualitative shape of the experimental curve, but the quantitative value is dramatically lower. This is consistent with the steady-state analysis of Refs. [7, 18], wherein it was observed that the model is not quantitatively accurate at low shear rates. This problem is exacerbated by the greater degree of relative error in the experimentally measured value of the dichroism due to its small magnitude at low deformation rates. As the steady-state shear rate increases, the model becomes quantitatively accurate as well as qualitatively so. At the higher values of the steady-state shear rate, the curves display maxima upon start up and cessation of flow. This occurs because the structures increase and then decrease in size and shape as the flow field approaches its steady state. At the highest values of

the steady-state shear rate, the dichroism decreases to the point where it actually has a negative value, as indicated in Figure 54. At this point, the structures have become rather small and optically isotropic (i.e., spherical), and the dichroism is dominated by the inherent anisotropy of the individual chains remaining in solution [7]. (Remember that Polystyrene has a negative intrinsic optical anisotropy.) At flow cessation, the structures back track the path they took upon shear start up, until the solution returns to its quiescent condition.

The most interesting prediction of this analysis is obtained for the dichroic orientation angle for this solution at $\dot{\gamma}_{ss} = 7037\ s^{-1}$, as displayed in Figure 55. Recall that at this shear rate, the steady-state dichroism has a negative value, implying that the physical mechanism dominating the dichroic signal has switched from the structures to the individual polymer chains. Therefore, the model predicts that during flow start up and flow cessation, a discontinuity should appear in the orientation angle as the dominating mechanism switches from the structures to the chains. Hence the orientation angle switches discontinuously from that of the structures to that of the chains. (Although this data was not presented directly in [2, 3], raw data for this case was given, so that the current authors were able to calculate the experimental curve.) It is evident that the experimental data displays the same type of discontinuity, at exactly the same times as the model predictions. This gives a strong validation of the notion initiated in Ref. [7] that the dichroism switches from a structure-controlled mechanism to an individual chain-controlled mechanism at very high shear rates.

4.2 Rheology

No transient rheological data is presented by Kishbaugh and McHugh for their rheo-optical experiments [2, 3]. However, they do state that for all cases, whether or not shear thickening was present, the shear stress curve almost exactly matched the trapezoidal shear profile of Figure 48. In Figure 56, we present plots of the shear stress versus time for the solutions of Figure 51. It is evident that the observed stress profiles are consistent with the statement expressed above. Furthermore, the TCMM Model also gives predictions for transient rheological properties that have not been measured experimentally. In Figures 57 and 58, we show predictions for both the first and second normal stress differences as functions of time at several values of the applied steady-state shear rate.

4.3 Birefringence

The TCMM Model also describes reasonably well the linear birefringence as a function of time for the shear thickening dilute polymer solutions. In Figures 59-61, we plot the transient birefringence for several shear rates of a Polystyrene/decalin solution from Refs. [2, 3]. For this set of transient data, no dichroism data was available, so we fit the TCMM Model to the birefringence data via Method 2, but using Eq. (II.17) instead of the corresponding dichroism equation. At low shear rates, the birefringence is positive as the signal is dominated by form birefringence. As the steady-state shear rate increases, however, the birefringence turns negative as the intrinsic optical anisotropy of the stretched Polystyrene chains takes over from the

form birefringence. The fits to the experimental data are quite reasonable qualitatively, but differ quantitatively at the higher values of the steady-state shear rate. As noted in Ref. [7], the birefringence changed by several orders of magnitude with increasing shear rate, thus rendering a quantitative data fit quite difficult. The main problem with this fitting is that the birefringent signal must be positive at low shear rates, and negative at high shear rates, and the negative signals are of much larger magnitude than the positive ones. The issue then becomes whether one wants an accurate fit at low shear rates, or at higher values. If one wants to fit higher values only, the parameter ω appearing in Eq. (II.17) is not required.

CHAPTER 5. CONCLUSIONS

In this article, we have focused on the transient analysis of the shear thickening in dilute polymer solutions. Using the TCMM Model, we were able to reproduce the experimental results of the transient analysis with considerable accuracy. The analysis of the transient data is useful in the determination of the kinetics and reversibility of the structure formation process. Hence the TCMM Model not only offers a consistent explanation for the rheological and optical behavior associated with shear thickening [7], but also provides valuable information about the kinetics of this phenomenon.

Some of the important conclusions of this analysis are as follows. The TCMM Model was able to capture the reversibility and instantaneity of the structure formation as it showed the rapid increases and declines under the application of a trapezoidal shear rate profile. For the solutions that exhibit shear thickening, the transient dichroism changes sign for each steady-state shear rate above $\dot{\gamma}_m$. The orientation angle of the dichroism does not change sign, but we observe discontinuities in this quantity that correspond to the sign change in the dichroism signal from positive to negative. This gives a very good indication that the physical mechanism that dominates the dichroic signal has changed at this point in time, as suggested in Ref. [7].

REFERENCES

1. R. B. Bird, et al., *Dynamics of Polymeric Liquids*. 2nd ed. Vol. 2. 1987, New York: John Wiley and Sons, Inc.
2. A.J. Kishbaugh, *The Rheo-Optics of Shear-Thickening and Structure Formation in Polymer Solutions*. 1992, University of Illinois.
3. A.J. Kishbaugh and A.J. McHugh, *A Rheooptical Study Of Shear-Thickening And Structure Formation In Polymer-Solutions.1. Experimental.* Rheologica Acta, 1993. **32**(1): p. 9-24.
4. M.N. Layec-Raphalen and C. Wolff, *Shear-Thickening Behavior Of Dilute-Solutions Of Chain Macromolecules.* Journal Of Non-Newtonian Fluid Mechanics, 1976. **1**(2): p. 159-173.
5. E.P. Vrahopoulou and A.J. McHugh, *Shear-Thickening And Structure Formation In Polymer-Solutions.* Journal Of Non-Newtonian Fluid Mechanics, 1987. **25**(2): p. 157-175.
6. A.J. Kishbaugh and A.J. McHugh, *A Rheooptical Study Of Shear-Thickening And Structure Formation In Polymer-Solutions.2. Light-Scattering Analysis.* Rheologica Acta, 1993. **32**(2): p. 115-131.
7. B.J. Edwards, D.J. Keffer, and C.W. Reneau, *An examination of the shear-thickening behavior of high molecular weight polymers dissolved in low-viscosity newtonian solvents.* Journal Of Applied Polymer Science, 2002. **85**(8): p. 1714-1735.
8. B.J. Edwards, A.N. Beris, and V.G. Mavrantzas, *A model with two coupled Maxwell modes.* Journal Of Rheology, 1996. **40**(5): p. 917-942.

9. M. Grmela, *Hamiltonian-Dynamics Of Incompressible Elastic Fluids.* Physics Letters A, 1988. **130**(2): p. 81-86.

10. M. Grmela, *Hamiltonian-Mechanics Of Complex Fluids.* Journal Of Physics A-Mathematical And General, 1989. **22**(20): p. 4375-4394.

11. A.N. Beris and B.J. Edwards, *Thermodynamics of Flowing Systems*. 1994, New York: Oxford University Press.

12. B.J. Edwards and A.N. Beris, *Noncanonical Poisson Bracket For Nonlinear Elasticity With Extensions To Viscoelasticity.* Journal Of Physics A-Mathematical And General, 1991. **24**(11): p. 2461-2480.

13. B.J. Edwards and A.N. Beris, *Unified View Of Transport Phenomena Based On The Generalized Bracket Formulation.* Industrial & Engineering Chemistry Research, 1991. **30**(5): p. 873-881.

14. E.F. Gurnee, Journal of Applied Physics, 1954. **25**: p. 1232.

15. W. Kuhn and F. Grün, Kolloid-Z., 1942. **101**: p. 248.

16. M. Copic, Journal of Chemical Physics, 1957. **26**: p. 1382.

17. V.N. Tsvetkov, Soviet Physics Uspekhi, 1964. **6**(639).

18. B. Jiang, et al., *Modeling shear thickening in dilute polymer solutions: Temperature, concentration, and molecular weight dependencies.* Journal Of Applied Polymer Science, 2003. **90**(11): p. 2997-3011.

19. W.H. Press, et al., *Numerical Recipes in Fortran 77*. 1992, Cambridge: Cambridge University Press.

APPENDIX

Table 8: Parameter values for the 6.8×10^{6} g/mol Polystyrene/decalin solution with $c = 0.30$ g/dl at $25^{0}C$.

	λ_1(s)	λ_2(s)	$n_1(\text{mol/m}^3)$	$n_2(\text{mol/m}^3)$	θ	$\langle aa\rangle_0(\text{m}^2)$
Method 1	0.004333	0.013	1.0×10^{-3}	1.0×10^{-6}	0.10	4.20×10^{-16}
Method 2	0.001117	0.011	4.2×10^{-5}	4.1×10^{-7}	0.17	5.35×10^{-16}

Table 9: Parameter values for the 1.54×10^{6} g/mol Polystyrene/decalin solution with $c = 0.79$ g/dl at $25^{0}C$.

	λ_1(s)	λ_2(s)	$n_1(\text{mol/m}^3)$	$n_2(\text{mol/m}^3)$	θ	$\langle aa\rangle_0(\text{m}^2)$
Method 2	0.002769	0.0052	4.183×10^{-6}	4.181×10^{-6}	0.03	4.19×10^{-16}

Table 10: Parameter values for the 6.8×10^{6} g/mol Polystyrene/decalin solution with $c = 0.10$ g/dl at $25^{0}C$.

	λ_1(s)	λ_2(s)	$n_1(\text{mol/m}^3)$	$n_2(\text{mol/m}^3)$	θ	ω
Method 2	0.002258	0.0417	4.06×10^{-4}	9.22×10^{-7}	0.26	96.48

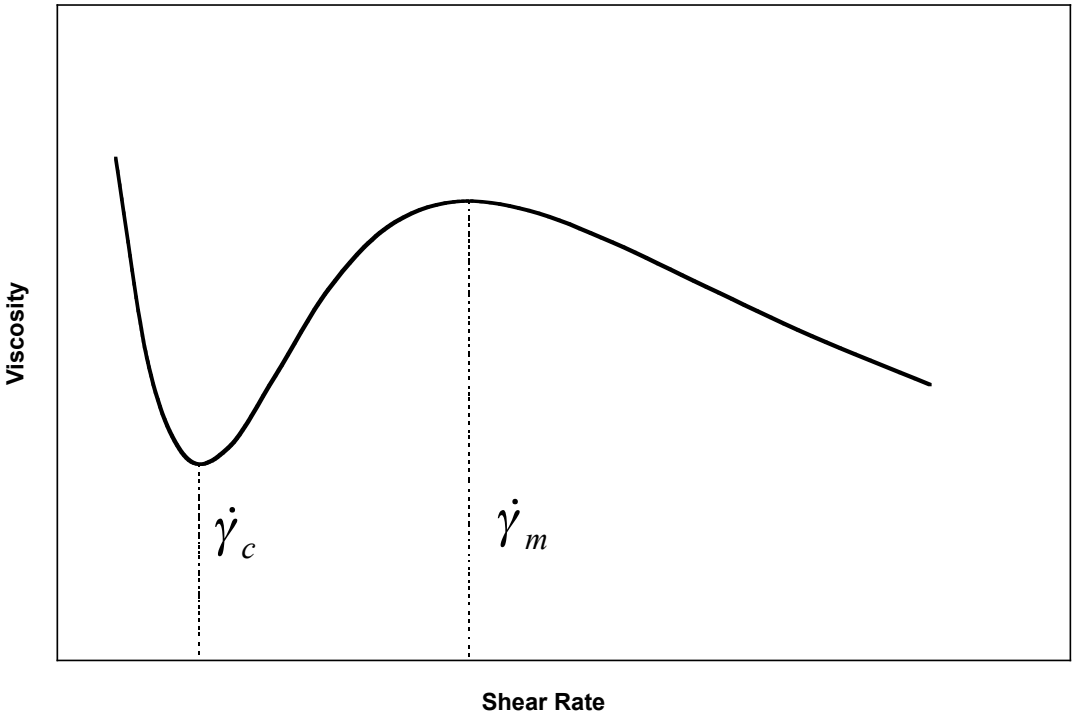

Figure 47: Generic profile of viscosity versus shear rate for a dilute polymer solution that exhibits shear thickening

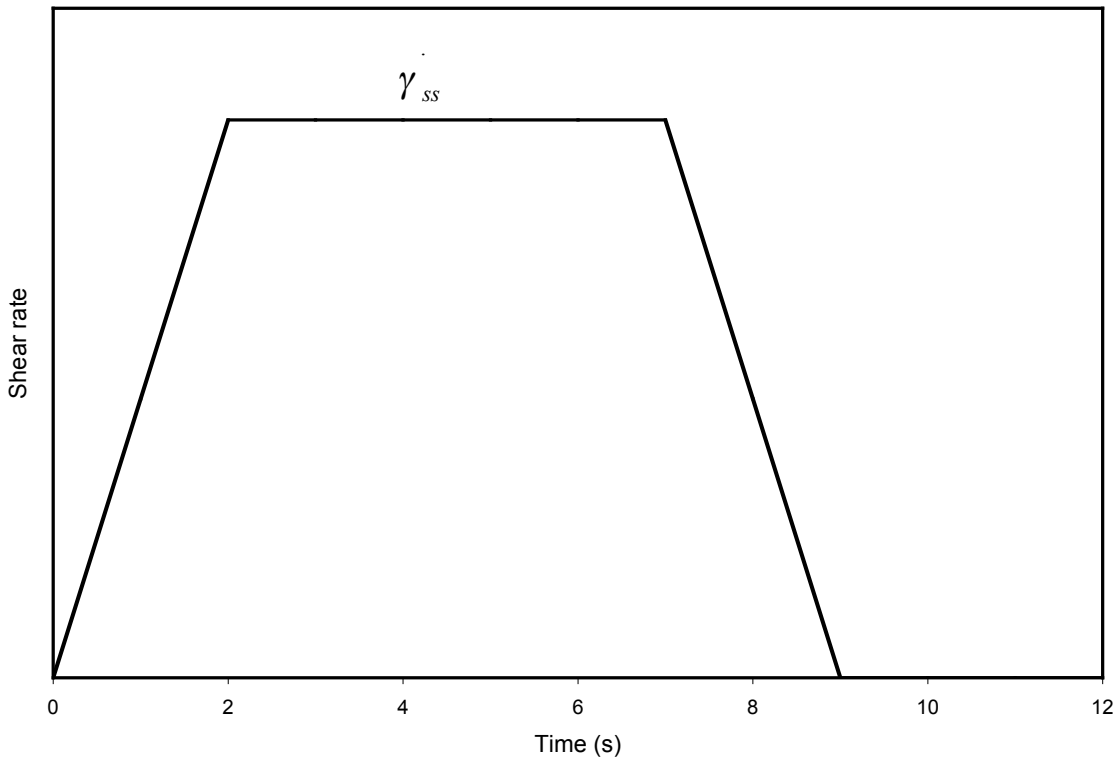

Figure 48: Trapezoidal velocity profile used for most of the rheo-optical measurements of Refs. [2,3]

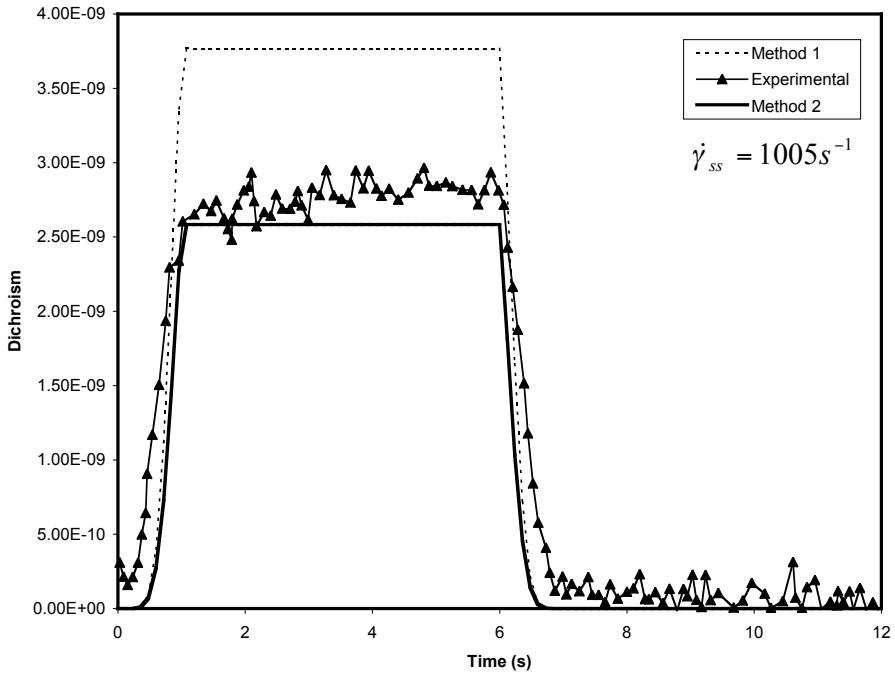

Figure 49: Transient dichroism for the solution with $c = 0.30$ g/dl at a steady-state shear rate of 1005s^{-1}

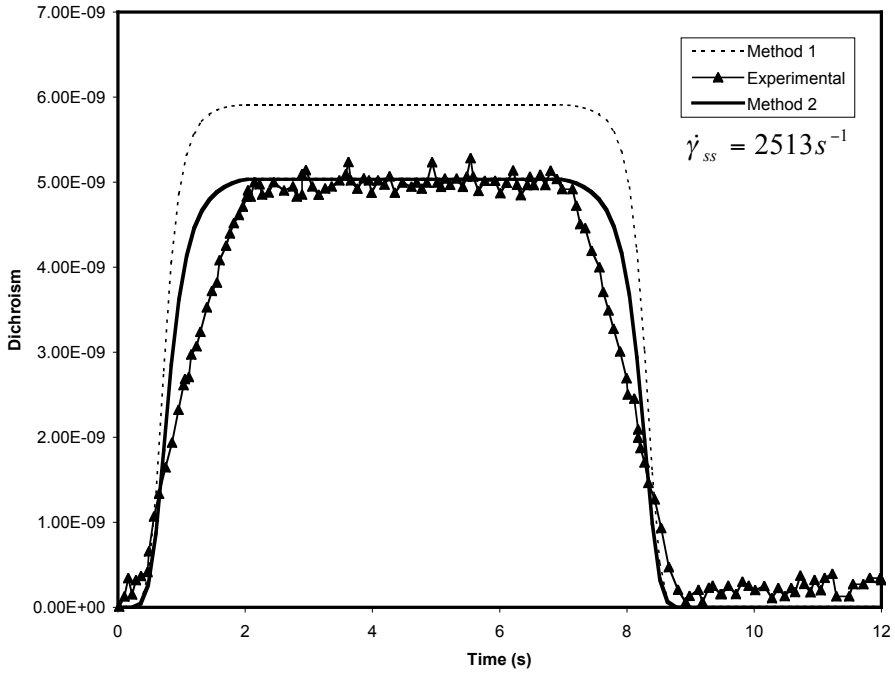

Figure 50: Transient dichroism for the solution with $c = 0.30$ g/dl at a steady-state shear rate of 2513s^{-1}

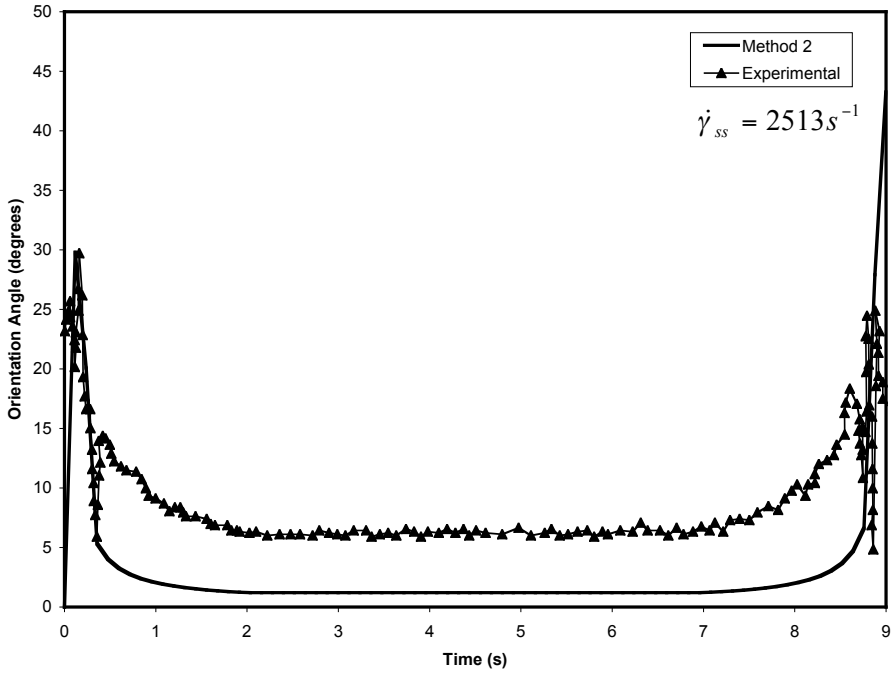

Figure 51: The orientation angle of the dichroism for the 6.8×10^{6} g/mol Polystyrene/decalin solution with $c = 0.30$ g/dl at $\dot{\gamma}_{ss} = 2513s^{-1}$

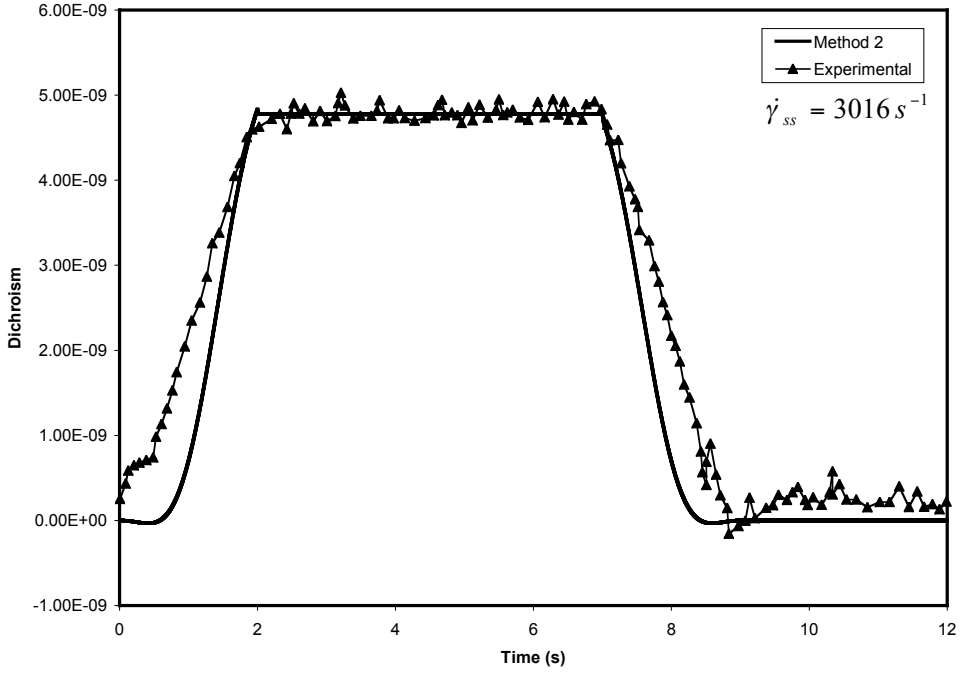

Figure 52: Transient dichroism for the 1.54×10^{6} g/mol Polystyrene/decalin solution with $c = 0.79$ g/dl at $\dot{\gamma}_{ss} = 3016 s^{-1}$

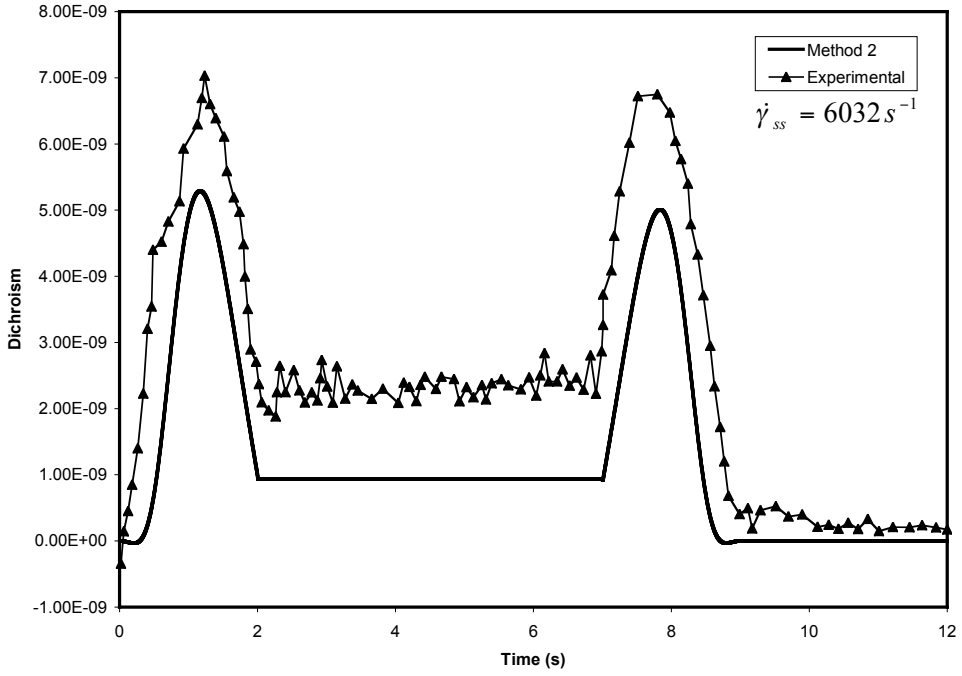

Figure 53: Transient dichroism for the 1.54×10^{6} **g/mol Polystyrene/decalin solution with** $c = 0.79$ **g/dl at** $\dot{\gamma}_{ss} = 6032s^{-1}$

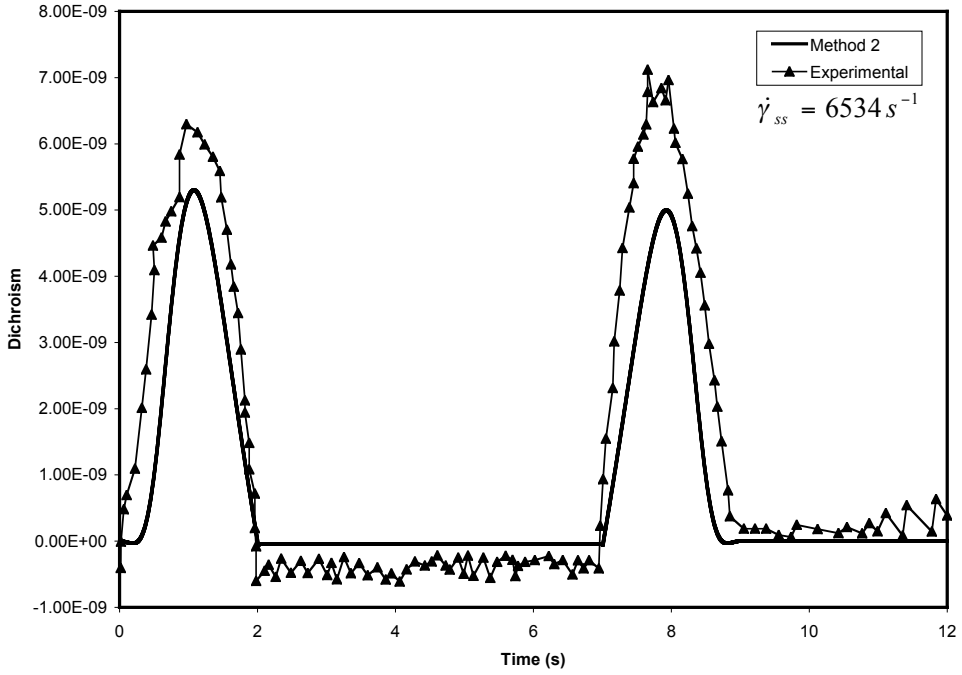

Figure 54: Transient dichroism for the 1.54×10^{6} **g/mol Polystyrene/decalin solution with** $c = 0.79$ **g/dl at** $\dot{\gamma}_{ss} = 6534 s^{-1}$

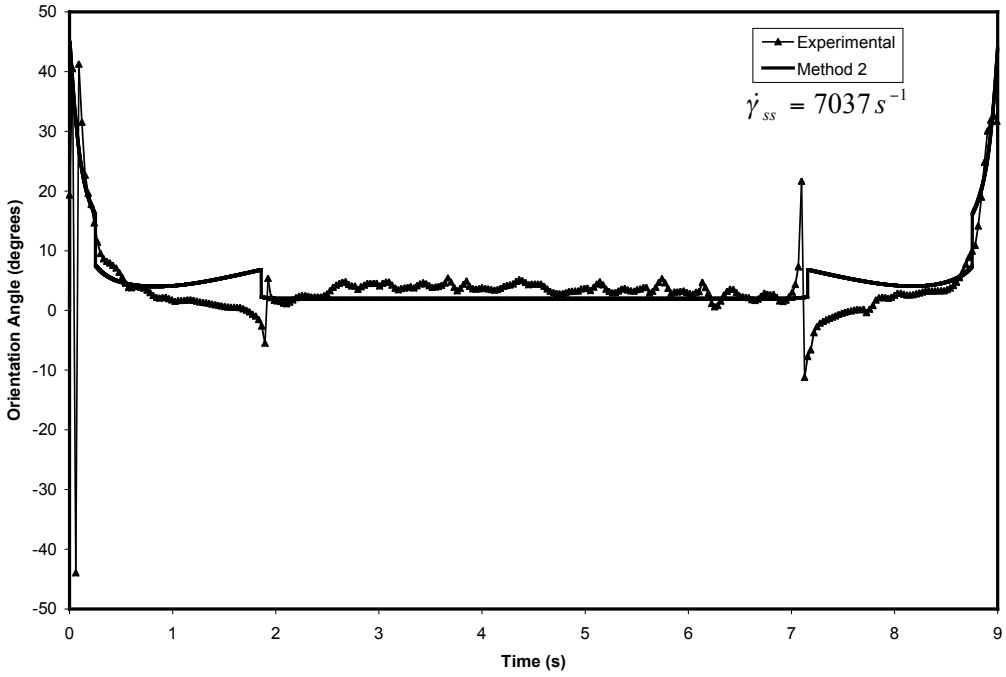

Figure 55: The orientation angle of the dichroism for the 1.54×10^{6} g/mol Polystyrene/decalin solution with $c = 0.79$ g/dl at $\dot{\gamma}_{ss} = 7037\,s^{-1}$

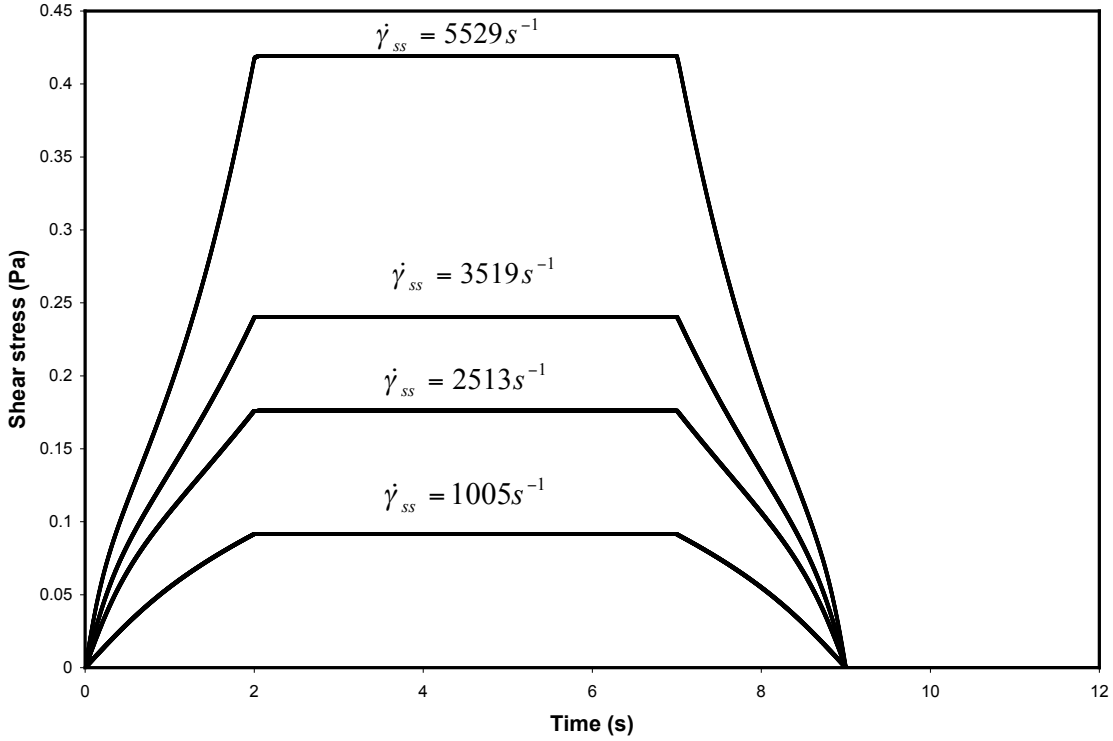

Figure 56: The shear stresses for the 6.8×10^{6} g/mol Polystyrene/decalin solution with c = 0.30 g/dl at four steady-state shear rates

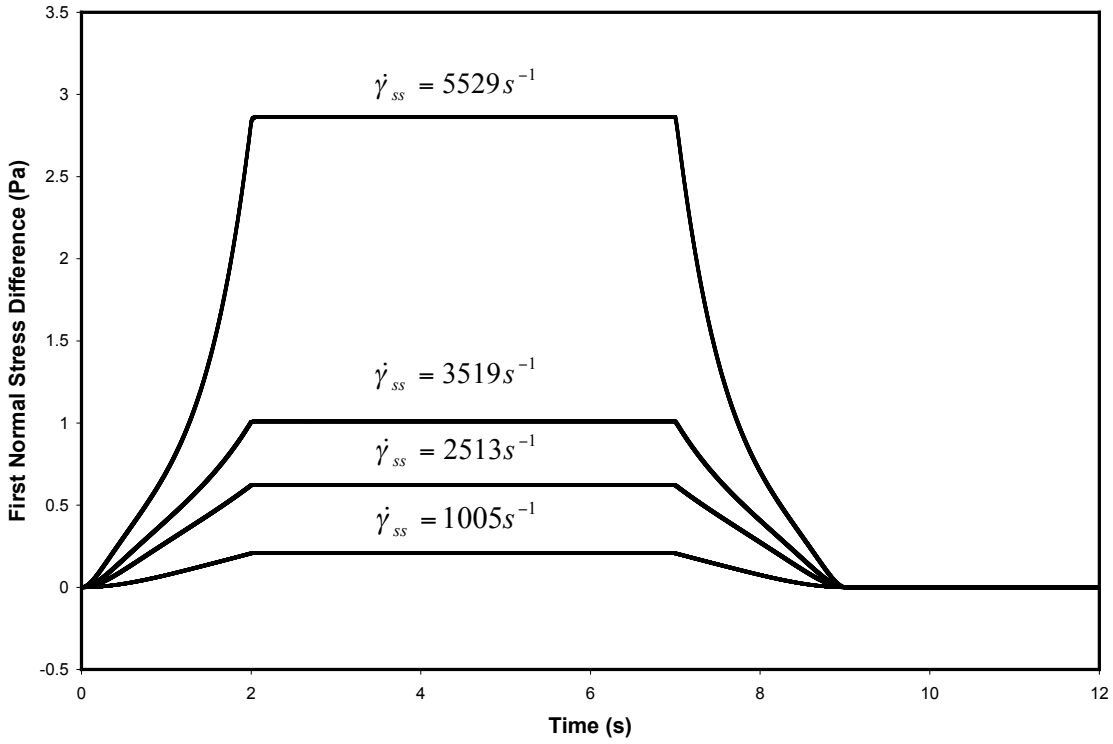

Figure 57: The first normal stress differences for the 6.8×10^{6} g/mol Polystyrene/decalin solution with $c = 0.30$ g/dl at four steady-state shear rates

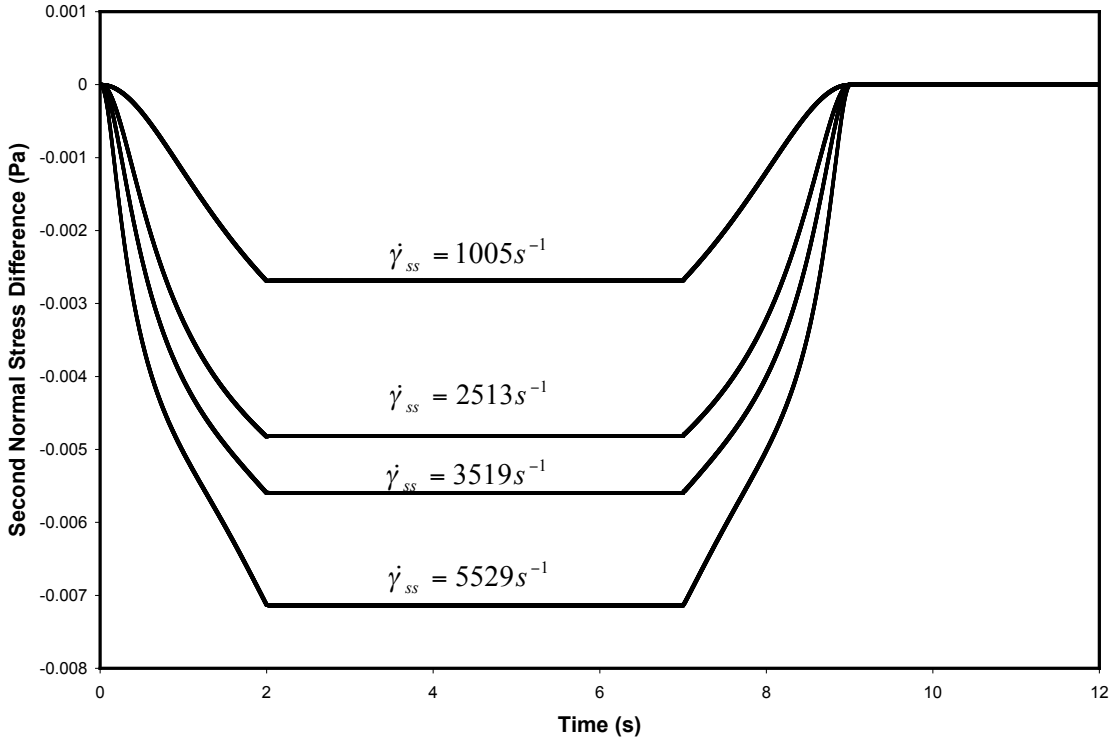

Figure 58: The second normal stress differences for the 6.8×10^{6} g/mol Polystyrene/decalin solution with $c = 0.30$ g/dl at four steady-state shear rates

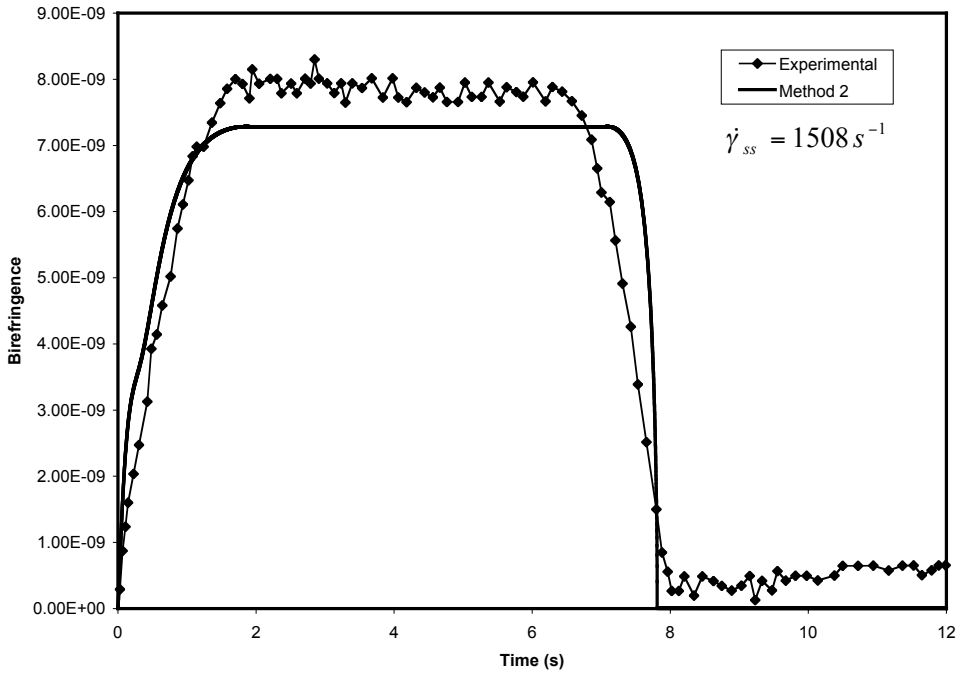

Figure 59: Transient birefringence for the 6.8×10^{6} g/mol Polystyrene/decalin solution with $c = 0.10$ g/dl at $\dot{\gamma}_{ss} = 1508 s^{-1}$

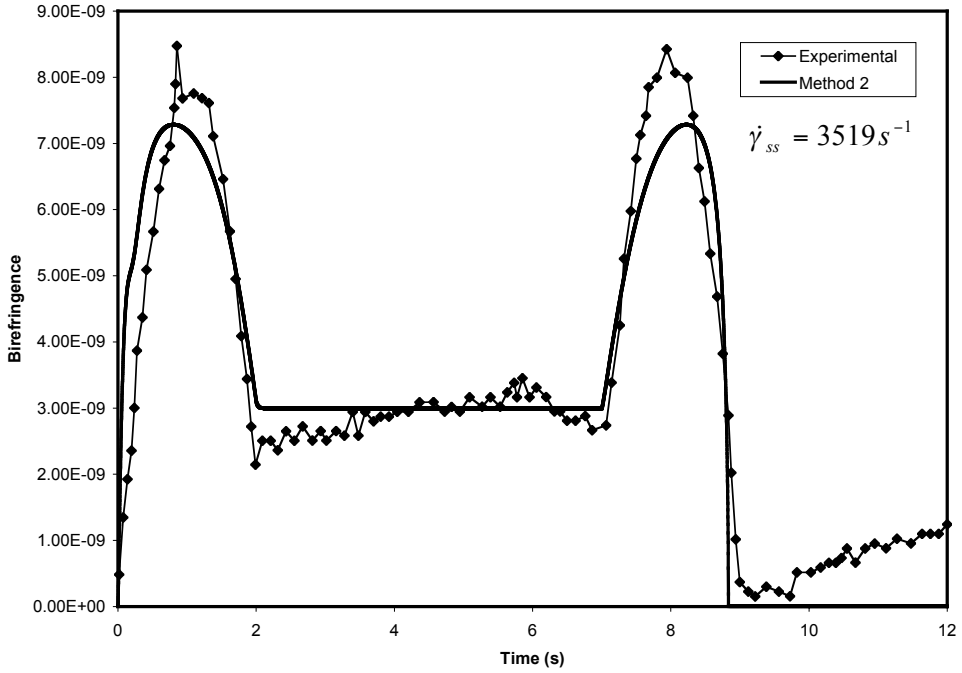

Figure 60: Transient birefringence for the 6.8×10^{6} g/mol Polystyrene/decalin solution with $c = 0.10$ g/dl at $\dot{\gamma}_{ss} = 3519 s^{-1}$

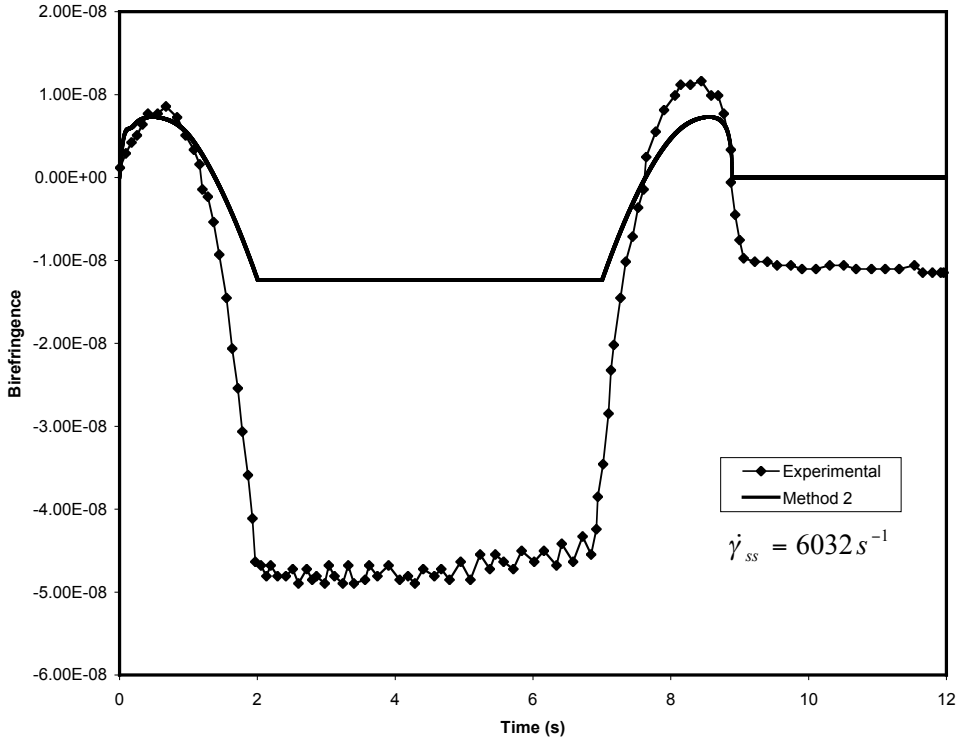

Figure 61: Transient birefringence for the 6.8×10^{6} g/mol Polystyrene/decalin solution with $c = 0.10$ g/dl at $\dot{\gamma}_{ss} = 6032 s^{-1}$

Part III: Additional Experimental Research in Polymer Melt Rheology

CHAPTER 1. EXPERIMENTS WITH LDPE

Shear viscosity measurements were performed using the Advanced Capillary Extrusion Rheometer (ACER) and the Advanced Rheometrics Expansion System (ARES) by Rheometrics Scientific™. The LDPE samples were obtained from Exxon, which were prepared using a Ziegler-Nata catalyst. The LDPE had a wide molecular weight distribution with a value of the polydispersity index of 5.15. The value of the melt index was 0.2 g/minute, with a density of 0.923 g/cm^3. The weight-average molecular weight, according to gel permeation chromatography, was 80,350 g/mol. All the experiments were carried out at 175°C.

A variety of experimental data were obtained. The ARES was used to perform a dynamic frequency sweep in the range of about 0.01s^{-1}-100 s^{-1}. These small amplitude oscillatory shear flow experiments gave the storage modulus (G') and loss modulus (G'') data, as seen in Figure 62[**]. Shear viscosity data over a wide range of shear rates (0.001 s^{-1}-40000 s^{-1}) was also obtained. To cover this range of shear rates, we used ARES at low shear rates, ACER at higher shear rates, and complex viscosity measurements (on ARES) to cover the range between 1 to10 s^{-1}. Transient shear stress data (start up and relaxation) and first normal stress difference data are plotted in Figures 63, 64, as measured using a cone-plate geometry on ARES. From this transient data, we obtained steady-state shear stress and first normal stress difference

[** *] All the figures and tables for Part III are included in the appendix for this part.

data for a shear rate range of $0.01s^{-1}$-3 s^{-1}. This data is shown in Figures 65 and 66. The steady-state shear viscosity was also measured, as seen in Figure 67.

The viscosity measurements performed over the shear rate range 0.001 s^{-1}-40,000 s^{-1} are presented in Figure 68, which contains the comparison between the data from two different types of rheometers and three different types of experiments, mentioned above. We can see that the data agrees very well over the entire range and there are no discrepancies when moving from one method to another.

This data was later fitted using various multiple mode rheological models, and the parameters obtained were used to predict other properties like elongational viscosity, step-strain profiles, etc. Two papers were written based upon this experimental data [1,2] and a third one is currently under preparation.

REFERENCES

1. B. Jiang, et al., *A Test Case for Predicting the Rheological Properties of Polymeric Liquids: the Multiple Coupled Maxwell Modes Model.* J. Non-Newtonian Fluid Mech., 2004. **120**: p. 11-32.

2. B. Jiang, et al., *Using Multiple-Mode Models for Fitting and Predicting the Rheological Properties of Polymeric Melts.* J. Appl. Polym. Sci., Accepted 2005.

APPENDIX

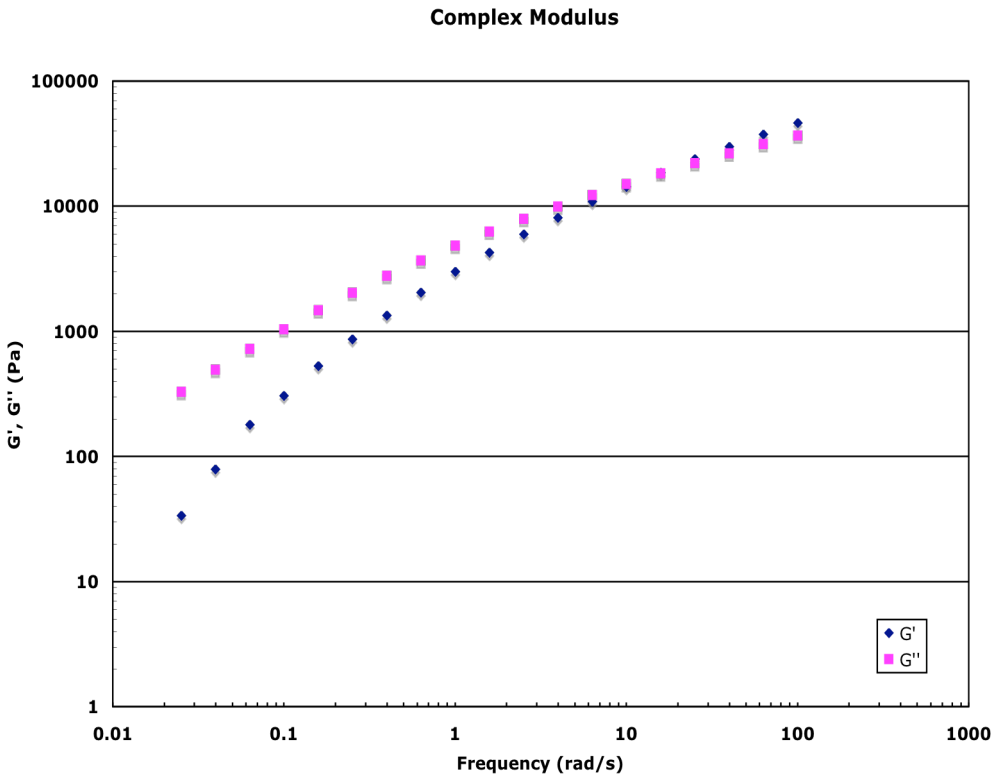

Figure 62: Storage modulus (G') and loss modulus (G') data plotted versus frequency for LDPE at 175^{o}C

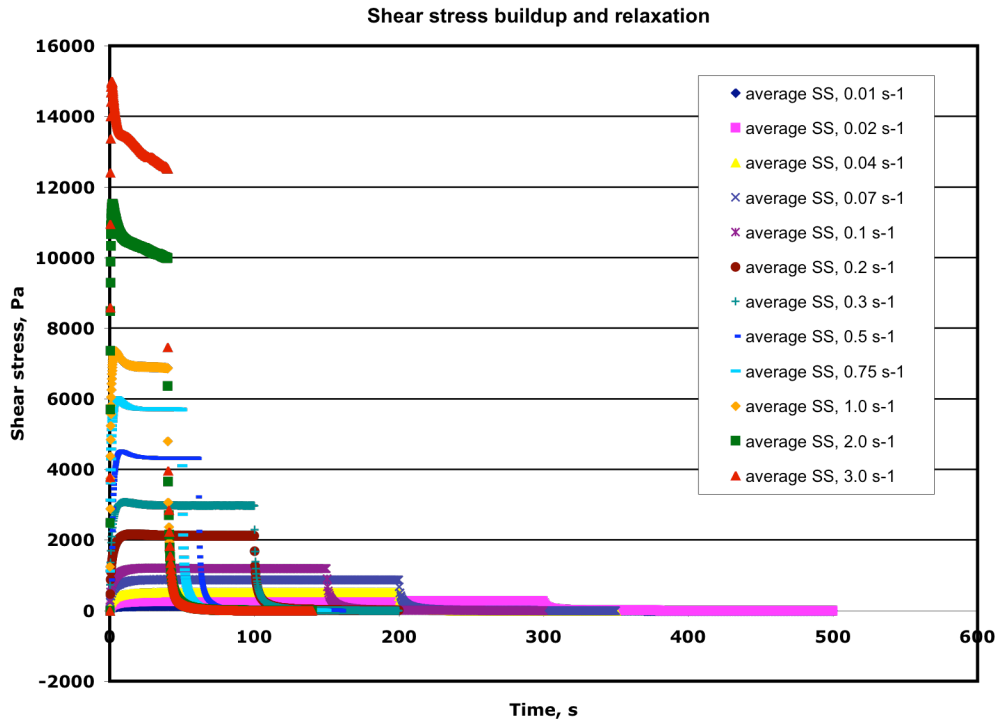

Figure 63: Shear stress build-up and relaxation data at various shear rates in the transient shear flow for LDPE at 175^{o}C

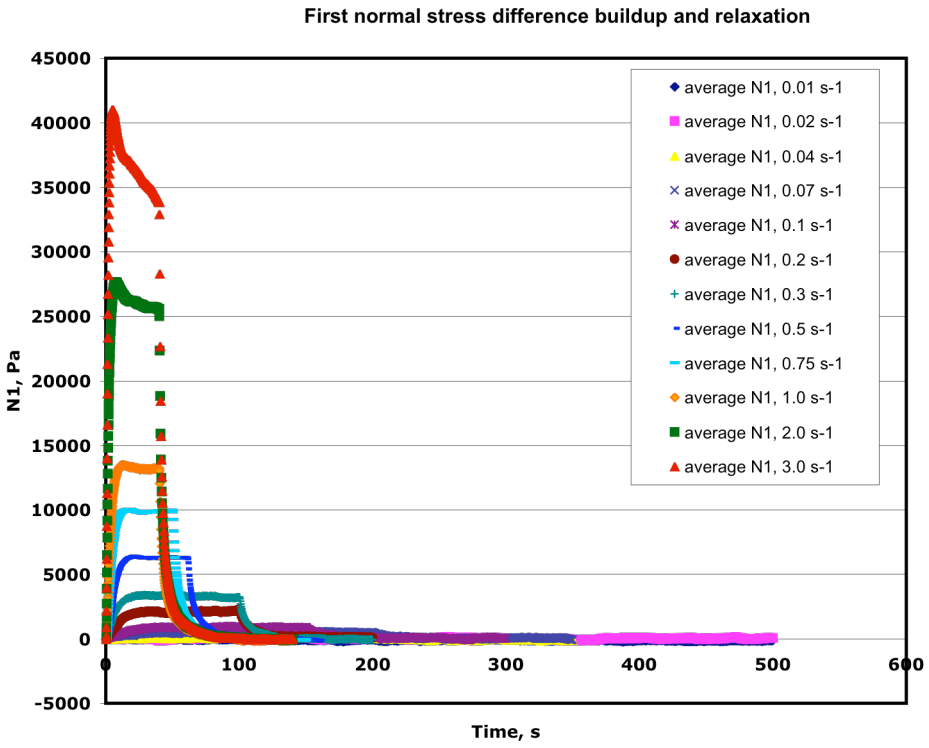

Figure 64: First normal stress difference build-up and relaxation data at various shear rates in the transient shear flow for LDPE at 175^{o}C

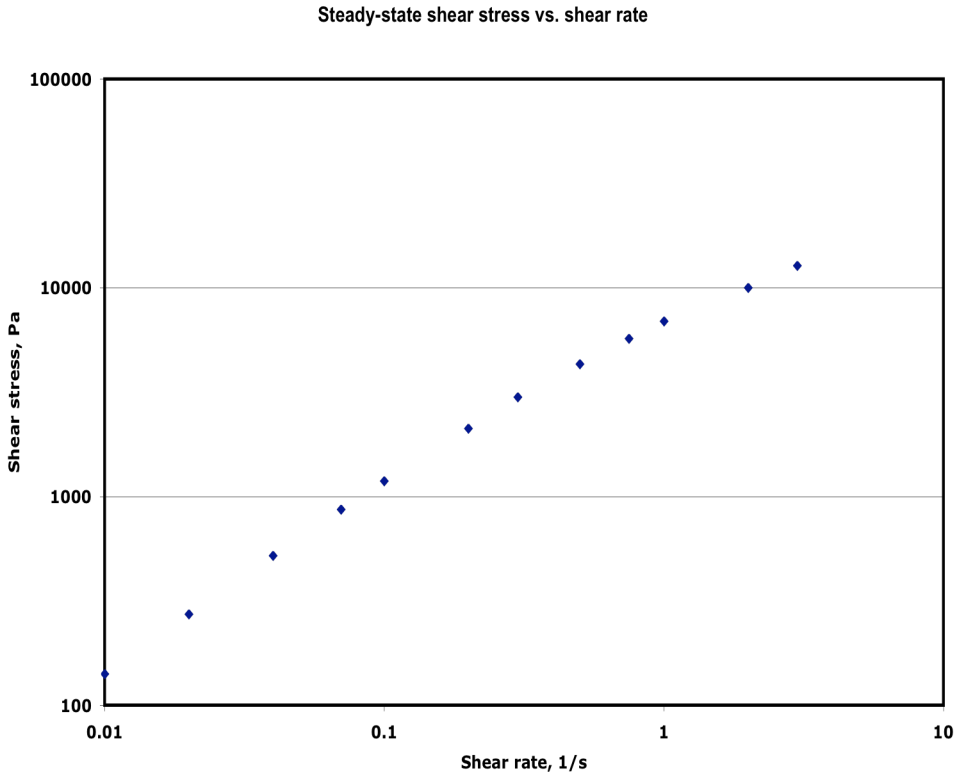

Figure 65: Steady-state shear stress data plotted vs. shear rate for LDPE at 175^{o}C

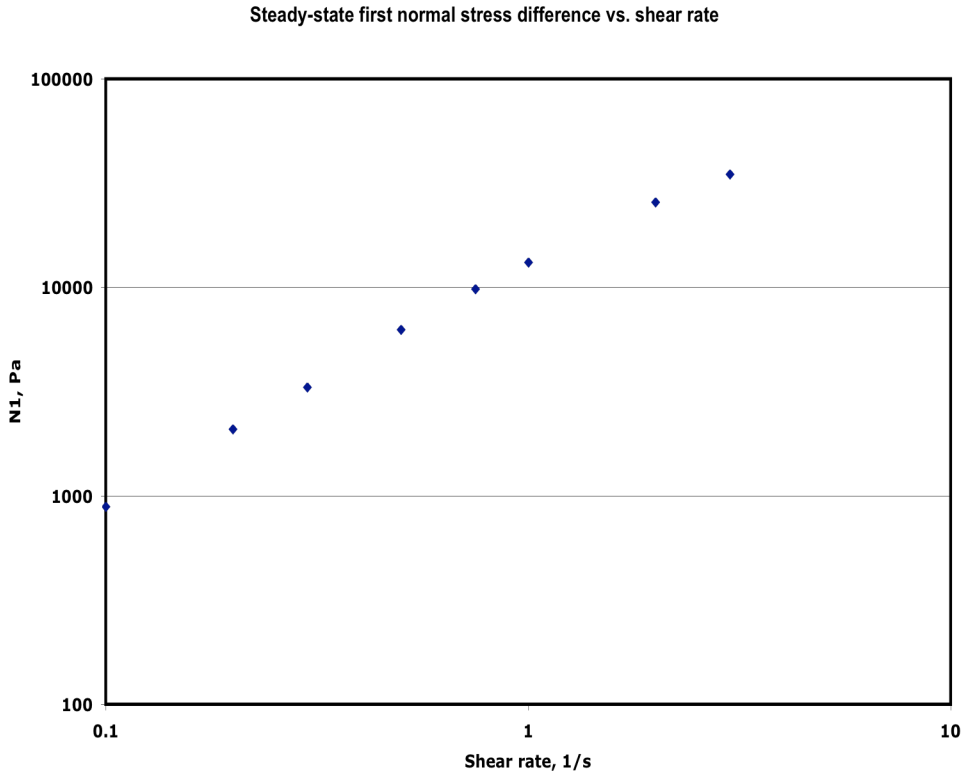

Figure 66: Steady-state first normal stress difference data plotted versus shear rate for LDPE at 175^{o}C

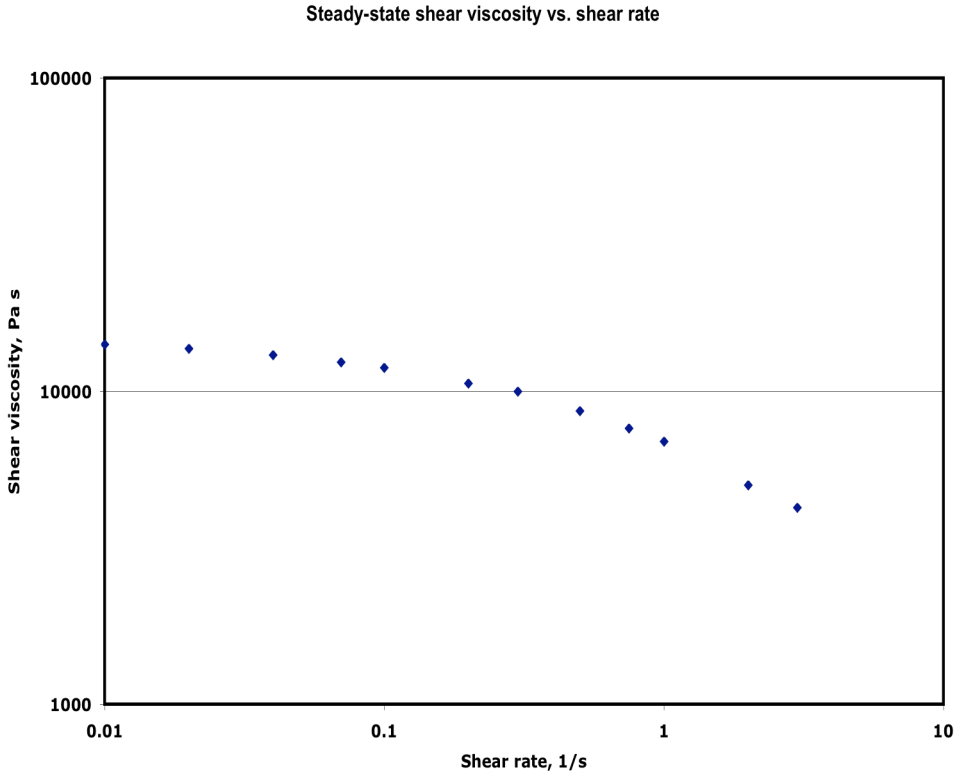

Figure 67: Steady-state shear viscosity data versus shear rate calculated from the transient shear flow for LDPE at 175^{o}C

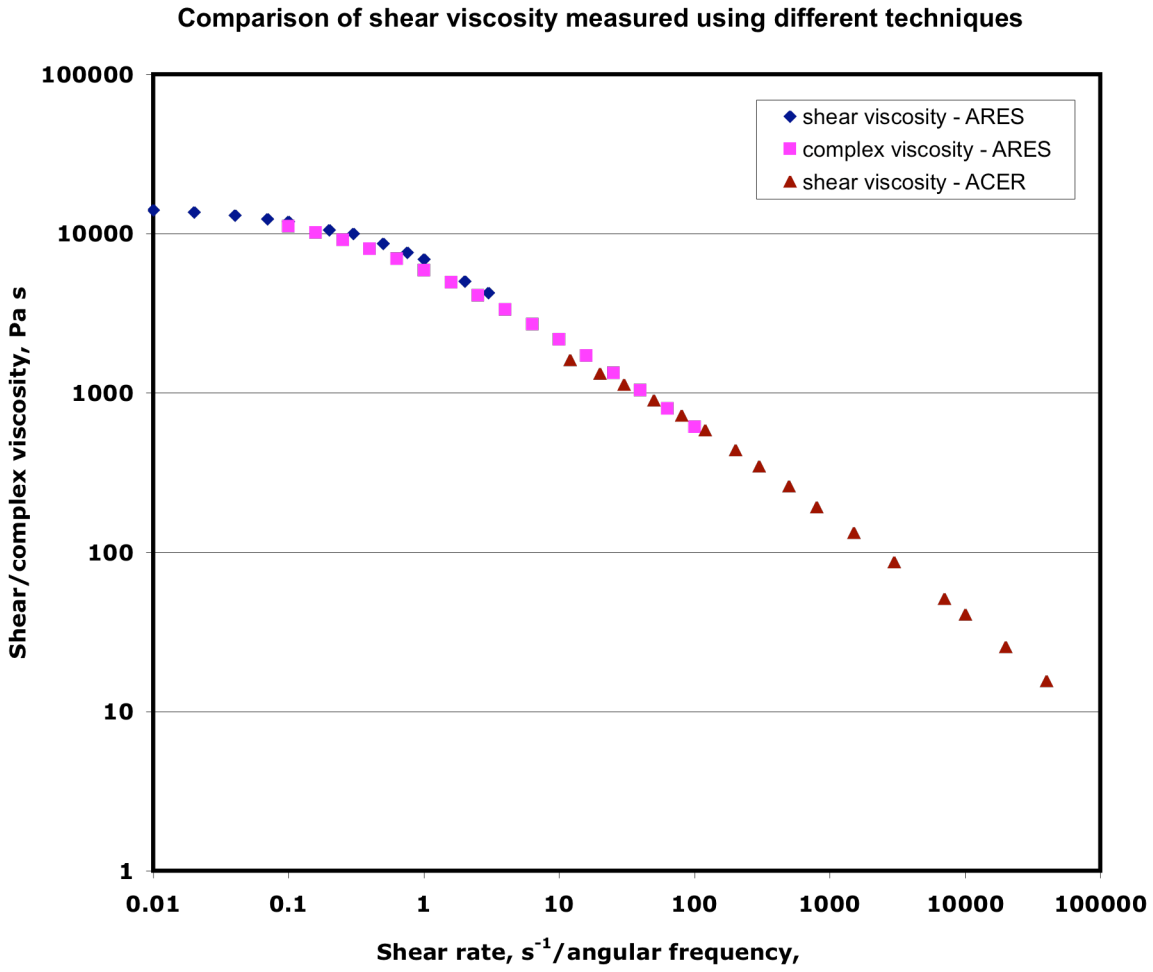

Figure 68: Comparison of shear viscosity measured using different techniques for LDPE at 175°C

VITA

Prajakta Kamerkar was born in Chiplun, India on 23rd April, 1980. She was raised in Mumbai, India where she joined the Mumbai University Institute of Chemical Technology in July 1997. There she received a Bachelor of Science degree in Chemical Engineering in May 2001.

She joined the Chemical Engineering Department at the University of Tennessee, Knoxville, as a graduate student in August 2001 to pursue a doctoral degree. She will receive the Ph.D. degree in Chemical Engineering in August 2005.